DEVELOPMENT OF SYNTHESIS STRATEGIES FOR EFFICIENT, ROBUST, AND STABLE LIGHT-EMITTING NANOCOMPOSITES BASED ON HALIDE PEROVSKITES

by MAI NGOC AN

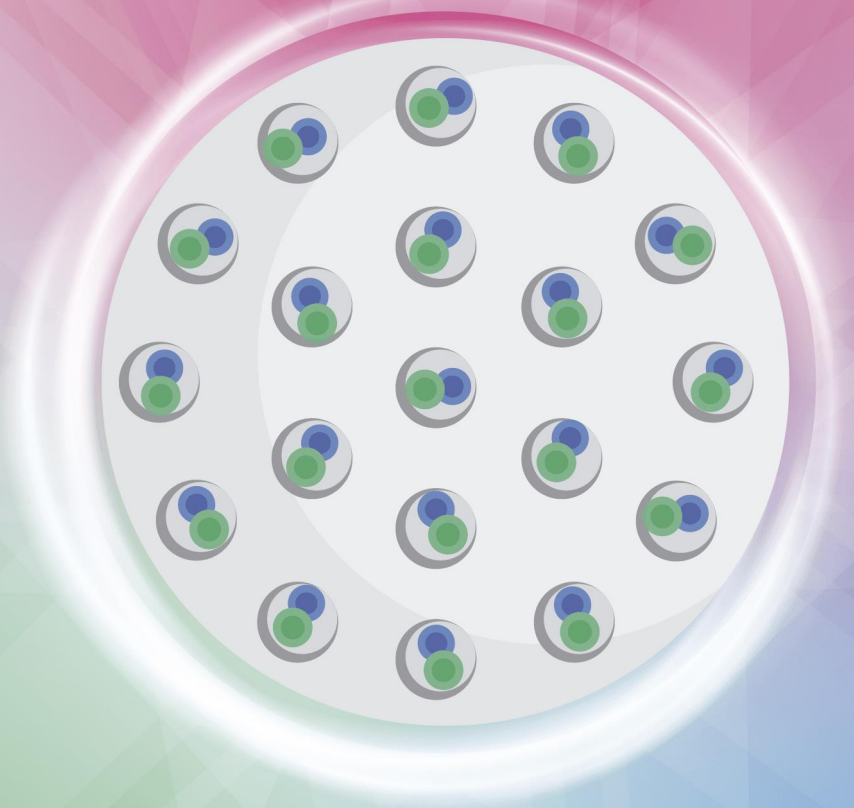

A Thesis

Submitted to the Università degli Studi di Genoa

In Partial Fulfillment of the Requirements for the degree of

Doctor of Philosophy

in

Sciences and Technologies of Chemistry and Materials

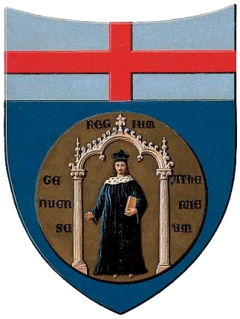

Nanochemistry Department

Università degli Studi di Genoa

ADVISORS:

Prof. Liberato Manna (IIT),

Dr. De Trizio Luca (IIT)

and

Prof. Ferretti Maurizio (DCCI, Unige)

All research was conducted at Istituto Italiano di Tecnologia, Genova

To my dearest father

TABLE OF CONTENTS

TABLE OF CONTENTS

ABSTRACT

Over the past few years, halide perovskites have generated extensive interest as potential materials for various applications, such as light-emitting diodes, displays, detectors, and tracking (e.g., bio-applications or oil tracing). Halide perovskite nanocrystals (NCs), having chemical formula ABX_3, where A is an organic or inorganic monovalent cation (e.g., Cs^+, $CH_3NH_3^+$, $CH(NH_2)_2^+$, etc.), B is a divalent metal cation (e.g., Pb^{2+}, Sn^{2+}, etc.), and X is halide anion (Cl^-, Br^- or I^-), possess excellent optical properties, which include high photoluminescence (PL) quantum yield (QY) and high color purity (narrow PL emission). However, the effective implementation of these halide perovskite NCs in industrial manufacturing processes is limited by their poor stability under various conditions: when exposed to humidity, high temperature, and photo-irradiation, the NCs are quickly degraded. Therefore, the research work included in this thesis is mainly focused on developing various strategies to improve the stability of halide perovskite NCs with the aim of implementing them in practical applications.

Among different matrix encapsulation materials for perovskites (such as polymers, inorganic metal oxide/halides, and metal-organic framework), silica has been chosen as an efficient matrix to protect halide perovskite NCs due to its excellent properties, which include high optical transparency in the visible, chemical stability, abundance, non-toxicity, and low-cost. A facile synthesis approach to produce $CsPbX_3$ NCs embedded in silica is developed as a simple and straightforward method via sol-gel route. The synthesis starts from colloidal Cs_4PbX_6 NCs, which is mixed with tetraethyl orthosilicate (Si precursor) in the presence of nitric acid, which triggers the sol-gel reaction yielding the formation of SiO_x and the concomitant conversion of starting Cs_4PbX_6 NCs into $CsPbX_3$ NCs. The resulting $CsPbX_3/SiO_x$ composites exhibit enhanced water and thermal stability under ambient conditions. When mixing $CsPbX_3/SiO_x$ samples with different anion compositions, no inter-particle anion exchange processes are observed, indicating that the silica shell acts as a robust barrier for $CsPbX_3$ NCs. Such composites have also been tested as down-converter phosphors on

top of a blue light-emitting diode (LED). The resulting WLED exhibits nearly ideal white light emission with the Commission Internationale de l'Eclairage (CIE) color coordinates (0.32, 0.33). The detailed results of this work are described in *chapter 2* of this thesis.

Chapter 3 shows another new approach to prepare $CsPbBr_3$/m-SiO_2 composite material made of mesoporous silica (m-SiO_2) particles whose pores are filled with $CsPbBr_3$ NCs and other inorganic salts (e.g., KNO_3, $NaNO_3$, and KBr). The protocol involved the use of a mixture of molten salts as the synthesis medium, in which the reaction occurs at 350 °C. The molten salts allow for the nucleation and growth of perovskite NCs inside the silica pores and enable the sealing of those pores. The resulting $CsPbBr_3$/m-SiO_2 composites have high PLQY values (around 90 %) and exhibit high stability against heat, water, and even aqua regia. The excellent properties of these composites made them attractive in various types of applications, such as LEDs for the display, and tracing/tagging for the oil industry. As a proof of concept, a white-LED is prepared by mixing green-emitting $CsPbBr_3$/m-SiO_2 composite with red-emitting $K_2SiF_6:Mn^{4+}$ on top of a blue LED. The device achieves stable white light emission with the Commission Internationale de l'Eclairage color coordinates (0.2985, 0.3076) and a CCT of 7692 K. The $CsPbBr_3$/m-SiO_2 composites are also demonstrated being promise as a potential oil tracer material as they could survive to the combined harsh conditions of saline water and high temperature, which represent the typical underground environment of oil wells.

Finally, two perovskite Sn-based materials, including Cs_2SnI_6 3D perovskite and $(C_{18}H_{35}NH_3)_2SnI_4$ 2D perovskite, are synthesized by a hot-injection method. The results of the structural and optical characterization of these materials are discussed in *chapter 4*, extending the scope of this work to non-toxic lead-free perovskite materials.

CHAPTER 1

Introduction

Abstract: *This chapter introduces halide perovskites with a brief overview of their structure, optoelectronic properties, synthesis technique, and applications. This section is followed by a short review of the encapsulation strategies employed to protect lead halide perovskites, especially those in which silica is used as a matrix. A general introduction to lead-free tin-based halide perovskite is presented afterward. Eventually, the motivation of the thesis is given.*

1.1. Halide perovskites

1.1.1. Chemical structure

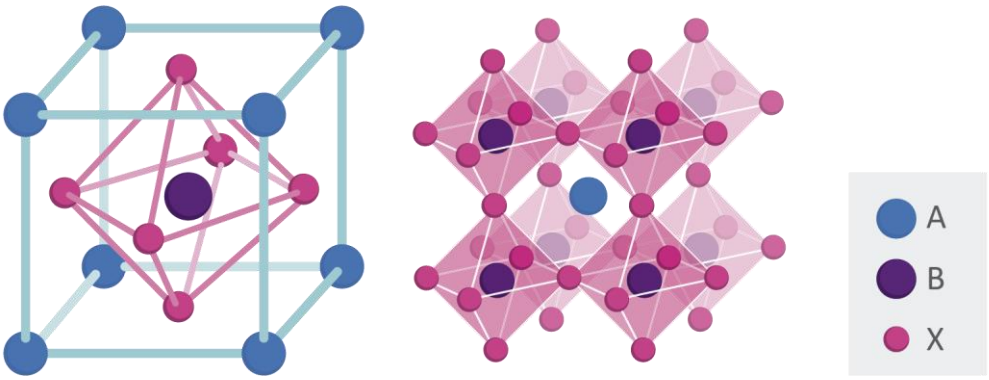

Figure 1.1. Structure of perovskites with ABX_3 formula.

The name "perovskite" was initially given in 1839 to the mineral form of $CaTiO_3$ and lent to the class of compounds having an ABX_3 stoichiometry, in which A is a monovalent cation, B is a divalent cation, and X represents an anion (O^-, Cl^-, Br^- and I^-). The B and X ions form the BX_6 octahedra with B in the center and X in the corners. By connecting the corners, the BX_6 octahedra extend to form a three-dimensional (3D) framework. Each unit cell of ABX_3 crystal comprises eight corner-sharing BX_6 octahedra, with the A-site cation occupying the cuboctahedra cavity (**Figure 1.1**). Recently, halide perovskites (HPs), in which X is either Cl^-, Br^- or I^-, A is a monovalent cation (e.g., Cs^+, Rb^+, $CH_3NH_3^+$ (methylammonium, MA^+),

$CH(NH_2)_2^+$ (formamidinium, FA^+), etc.), B is a divalent metal cation (e.g., Pb^{2+}, Sn^{2+}, Cu^{2+}, Ge^{2+}, Eu^{2+}, Ni^{2+}, etc.), have been much focused on as potential materials for different applications, such as light-emitting diodes, displays, detectors.[1-5]

The Goldschmidt tolerance factor, *t*,[6] has been used extensively used to predict the formation of a 3D-perovskite structure starting from various A and B cations:

$$t = \frac{r_A + r_X}{\sqrt{2(r_B + r_X)}}$$

where r_A and r_B represent the ionic radii of the A and B cations, respectively, and r_X is the ionic radius of the anion. The tolerance factor assesses if the A cation can fit inside the cavities of the BX_3 framework. $0.9 \leq t \leq 1$ is considered a good fit for an ideal cubic perovskite structure.[7] The range of $0.80 \leq t \leq 0.89$, a distorted perovskite structure with an orthorhombic, tetragonal, or rhombohedral crystal structure is most likely to be formed (**Figure 1.2**). Moreover, if $t > 1$ or $t < 0.8$, the A-site cation is either too large or too small, respectively, and the perovskite structure cannot form.[8-10]

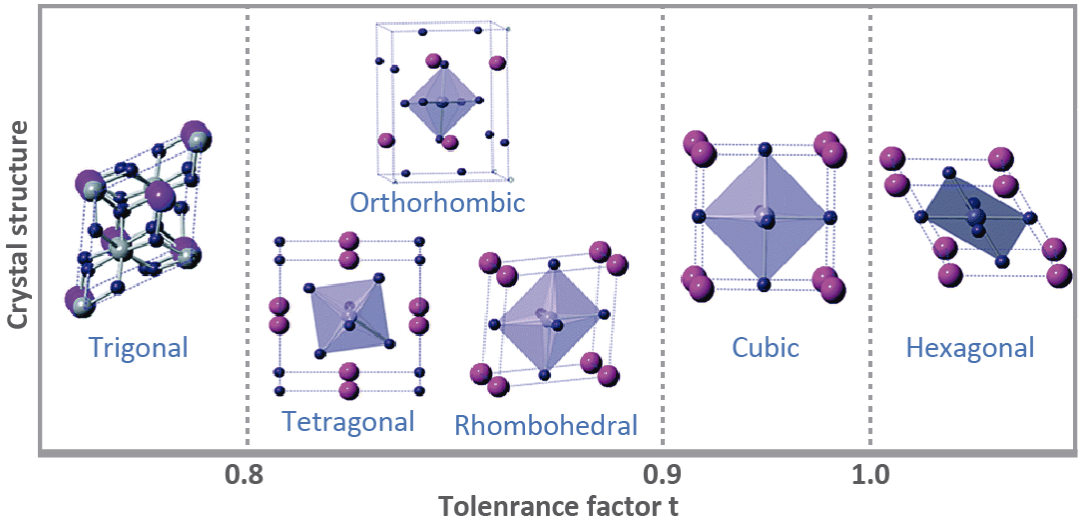

Figure 1.2. Correlation between the crystal structure of perovskite and the value of tolerance factor t. Reproduced from ref.[11] Copyright 2019 Royal Society of Chemistry

Besides the tolerance factor, the octahedral factor, μ,[9, 12] is also used to estimate the stability of a perovskite structure, which is defined as:

$$\mu = \frac{r_B}{r_X}$$

where r_B is the ionic radii of the B cation and r_X is the ionic radius of the anion. μ should lie between 0.44 and 0.90 to form stable perovskite structures.[8, 9, 13] The most popularly studied 3D HPs are cesium lead halide ($CsPbX_3$), methylammonium lead halide ($MAPbX_3$), formamidinium lead halide ($FAPbX_3$), and cesium tin halide ($CsSnX_3$) materials (**Figure 1.3**).

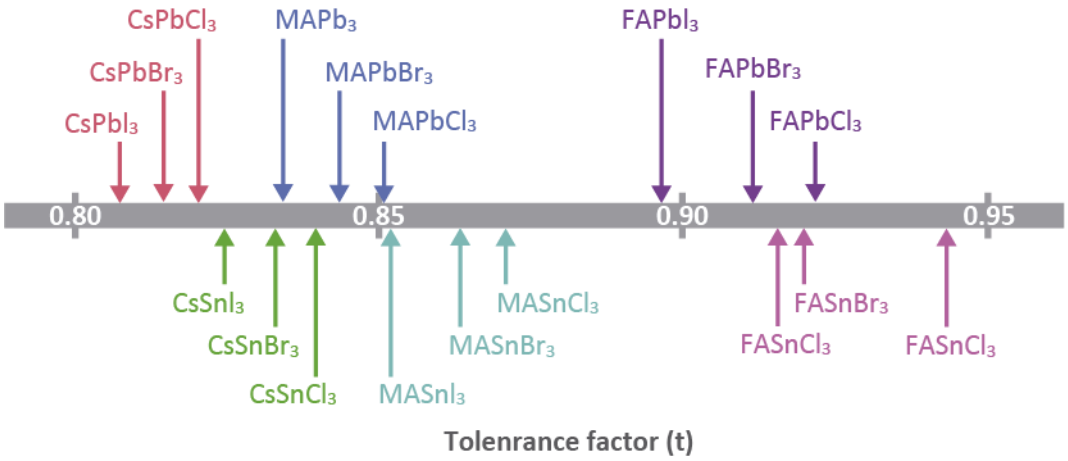

Figure 1.3. The most popularly studied 3D halide perovskites with their tolerance factors (t). Reproduced from ref.[14] Copyright 2018 Royal Society of Chemistry

Together with 3D HPs, 2D HPs also have attracted increasing attention recently. These 2D HPs, also call Ruddlesden–Popper-type perovskite could be regarded as a compound of ripping along a specific plane (*hkl*) of 3D parent halide perovskites with a formula of $A'_2A_{n-1}B_nX_{3n+1}$, where A' is mostly a large or long-chain organic cation; A represents small cations fitting in the voids of the layers, B refers to bivalent metal cations, X refers to halides; n is an integer, which indicates the number of halide octahedral layers between the two A' cation layers. (with n = 1 corresponds to a pure 2D structure; n = ∞ corresponds to a pure 3D structure; and n > 1 corresponds to quasi-2D layered structure) (**Figure 1.4**).[15, 16]

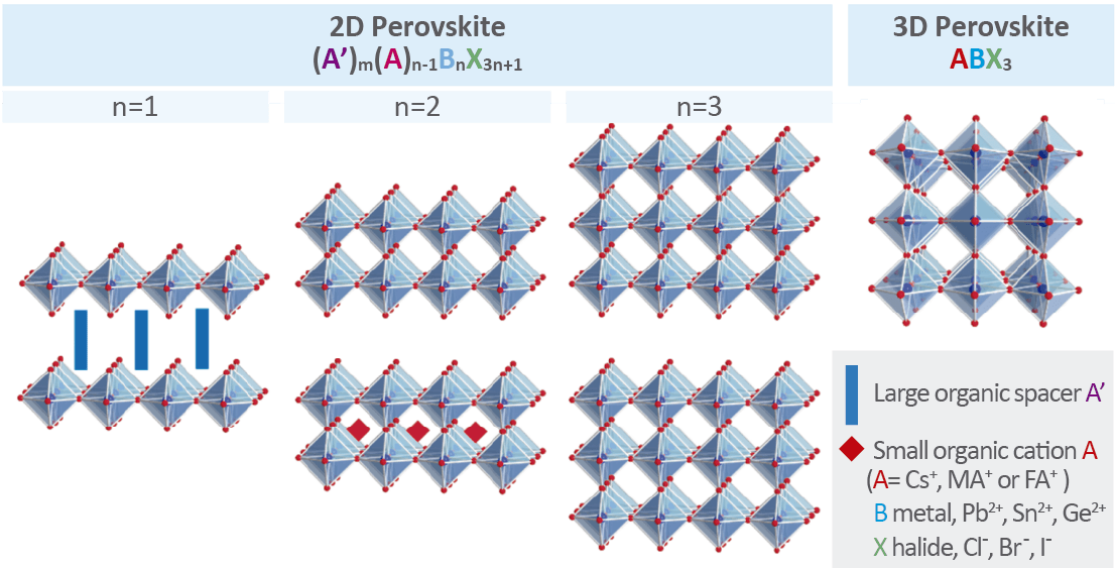

Figure 1.4. The structure of 2D (with the different number of layers n) and 3D halide perovskites (when n = ∞). Reproduced from ref.[17] Copyright 2019 American Chemical Society

It is worth introducing the Cs_4PbX_6 (X = Cl, Br, I) materials, also called 0D, which do not exhibit perovskite structure but have also been received much interest in structure and optical properties.[18, 19] Unlike 3D $CsPbX_3$, where the crystal structure is characterized by corner-shared $PbBr_6^{4-}$ octahedra, in the 0D Cs_4PbX_6 crystal structure has the PbX_6^{4-} octahedra are entirely decoupled in all dimensions (**Figure 1.5**).[20, 21]

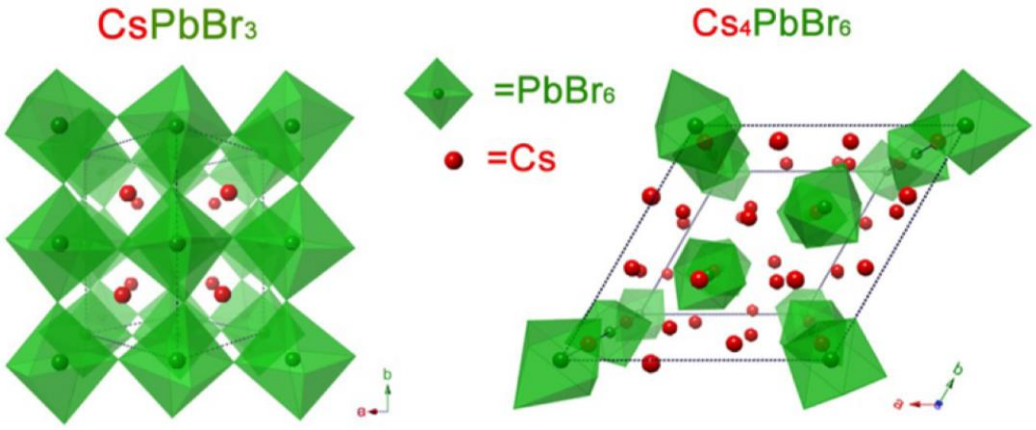

Figure 1.5. The crystal structure of Cs_4PbBr_6 with isolated $PbBr_6^{4-}$ octahedra compare to that of $CsPbBr_3$ with corner-shared. Reproduced from ref.[22] Copyright 2016 American Chemical Society

1.1.2. Optoelectronic properties

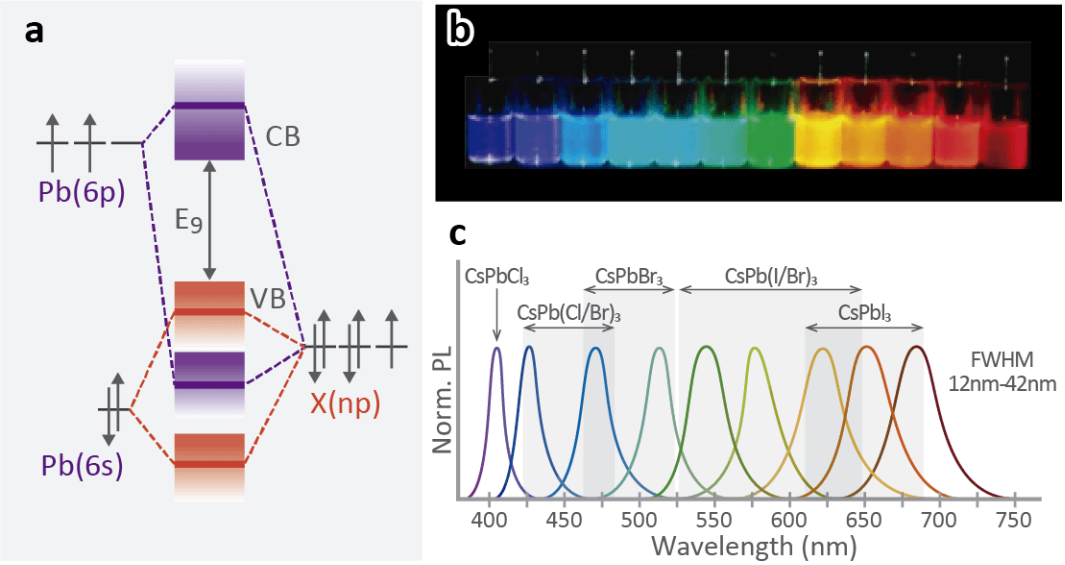

Figure 1.6. (a) Schematic representation of bonding/antibonding orbitals of $APbX_3$ showing the formation of the VB and CB. Reproduced from ref.[24] Copyright 2016 American Chemical Society **(b)** PL images and **(c)** PL spectra of colloidal solutions of $CsPbX_3$ (X = Cl, Br, I) perovskite nanocrystals. Reproduced from ref.[27] Copyright 2015 American Chemical Society

The optoelectronic properties of perovskite are dominated by charge transfer at the interface and optical transitions (absorption or emission), which strongly depend on the nature of the valence band maximum (VBM) and conduction band minimum (CBM). Here, the VBM is constituted predominately by the halide np^6 orbitals (n is the principal quantum number, n = 3, 4, and 5 for Cl, Br, and I, respectively) and ns^2 orbitals from B-site metal cation (n = 5, 6 for Sn and Pb, respectively) with a major contribution from halide np^6 orbitals. The CBM is constituted by antibonding mixing of the metal p orbitals (B-site) and the halide np^6 orbitals with dominant contributions from the metal p orbitals (B-site) (**Figure 1.6a**).[23-26] The electronic states of the A-site cation lie far away from VB and CB and thus provide no direct electronic contribution near the band edges.[24] As the halide moves from I ($5p^6$) to Br ($4p^6$) to Cl ($3p^6$), the energies of the halide np^6 orbitals decrease, shifting the VBM toward more positive potentials.[23] For instance, for $CsPbX_3$ (X = Cl, Br, and I) NCs, when changing the composition from $CsPbCl_3$ to $CsPbI_3$, the VBM shifts from −6.24 to −5.44 eV, whereas the CBM shifts from −3.26 to −3.45 eV and the band-gap tunes from 3.06 to 1.77 eV.[23, 25] A systematic change in the halide compositions of $CsPbX_3$

NCs from $CsPbCl_3$ to $CsPbBr_3$ to $CsPbI_3$ results in systematic variation in their optical gap and photoluminescence (PL) from blue to red (**Figure 1.6b-c**).[26]

The band-gap of HPs can can also be modified by varying the composition of the metal cations in the B-sites. For example, $CsSnX_3$ (X = Cl, Br, I and their mixtures) NCs varied from Cl^- to Br^- and to I^-, the band-gap was calculated to vary from 2.8 to 1.3 eV.[27, 28] The band-gap of Sn-based perovskite nanocrystals are narrowed compared to analogous Pb-based nanocrystals,[28] and this is due to the higher electronegativity of Sn^{2+} occupying the B site in ABX_3 perovskite lattice.[29]

Like 3D perovskites, the conventional 2D perovskites have direct excited-state transitions, with small Stokes shifts, narrow emission, low full width at half maximum (FWHM), and a relatively short lifetime in the order of nanoseconds. Besides, corrugated 2D perovskites,[30-32] which consist of twisted sheets ripped along the (110) crystallographic plane of 3D perovskites, have strongly Stokes shifted broad-band emissions due to exciton self-trapping. **Figure 1.7** shows the mechanism of exciton self-trapping: phtoexcited electrons can undergo fast relaxation to self-trapped states. They are noting that multiple trapped states are possible with different energies depending on the ground-state electronic structure of the material. The decay from the potential energy surface with multiple local minima results in broadband emission.

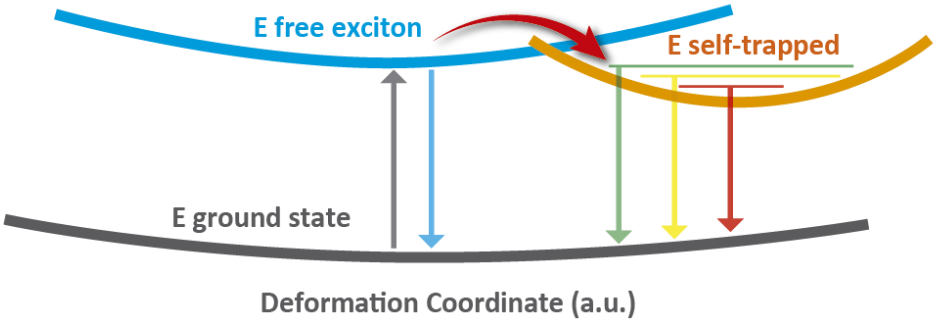

Figure 1.7. The mechanism for emission from both direct band and self-trapped states in corrugated 2D perovskites.

1.1.3. Colloidal halide perovskite nanocrystals

Halide Perovskite (HP) NCs have a soft and rather ionic lattice. The optical and electronic properties of HP NCs are highly tolerant of structural defects and

surface states, meaning that surface defects impart no significant detrimental effects to the photo-physics of HP NCs. This unique feature arises from the fact that typical defects (those with the lowest formation energy) result in relatively shallow states within the band-gap.[33, 34] The major attribute of HP NCs compared to the corresponding bulk counterpart is the impressive PLQY (lead halide perovskite NCs with PLQY up to 100 %).

HP NCs are routinely prepared by the ligand-assisted reprecipitation (LARP) or hot-injection method. LARP method is a simple technique and convenient for the preparation of perovskite nanocrystals at room temperature (RT).[35, 36] Typically, this technique consists of mixing a solution of HP precursors (e.g., CsBr, $PbBr_2$ for the formation of $CsPbBr_3$ NCs) in a "good" solvent (typically polar solvents where the HP precursors are soluble, e.g., DMF) into a vigorously stirred "poor" solvent (where HP precursors are not soluble, e.g., toluene) with long-chain organic ligands (normally amine and acid), which subsequently results in the controlled crystallization of precursors into colloidal NCs.[37] This facile approach enables producing different shapes of HPs such as spherical quantum dots, nanocubes, nanorods, and nanoplatelets by varying the capping ligands (**Figure 1.8a**).[35]

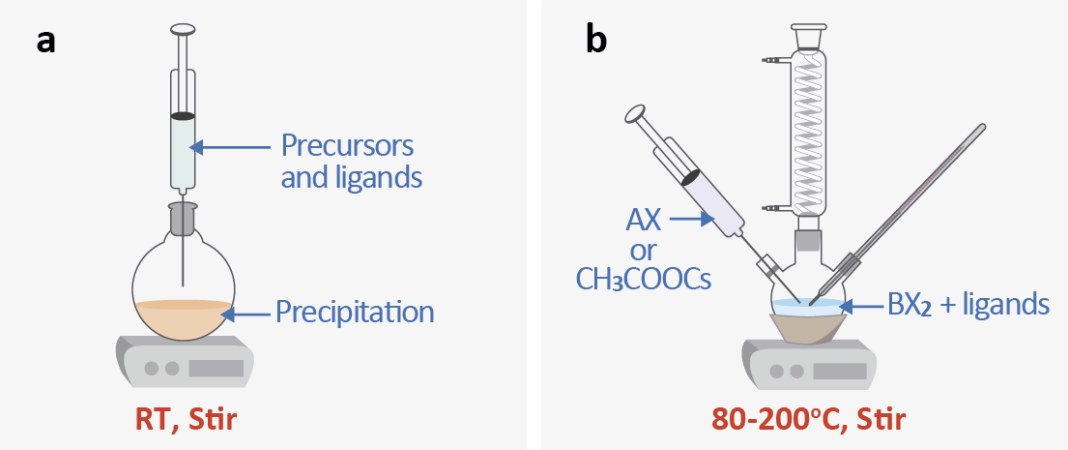

Figure 1.8. Synthesis of perovskite nanocrystals by the **(a)** LARP method and **(b)** hot-injection method. Reproduced from ref.[38] Copyright 2020 Royal Society of Chemistry.

Following the classical hot-injection method, which is frequently used to synthesize colloidal metal chalcogenide NCs, Protesescu et al. synthesized $CsPbX_3$ (X = Cl, Br, I and their mixtures) NCs by adapting such hot-injection

technique.[39] Generally, the nucleation and growth of $CsPbX_3$ NCs is triggered by the swift injection of cesium oleate into an octadecene solution containing PbX_2, oleic acid (OA), and oleylamine (OLA) at high temperatures (normally in the range of 140 – 200 °C) as expressed below and shown in **Figure 1.8b**:[40]

$$2\text{Cs-oleate} + 3PbX_2 \rightarrow 2CsPbX_3 + Pb(oleate)_2$$

LARP and hot-injection methods are also used for the synthesis of lead-free NCs. For example, the LARP method is useful for synthesizing lead-free $A_3M_2X_9$ perovskite NCs at RT: $Cs_3Sb_2Br_9$ NCs are prepared by mixing CsBr and $SbBr_3$ in DMF (or DMSO) supplemented with octadecylamine or n-octylamine and quickly adding a mixture of octane and oleic acid. $Cs_3Sb_2Br_9$ NCs are collected from the reaction solution by the addition of acetone or octane and centrifugation.[41] Besides, the hot-injection method was used for the synthesis of $CsSnX_3$ NCs: Cs_2CO_3 was suspended in a mixture of OA and OLA in octadecene, which is followed by injecting SnX_2 dissolved in tri-n-octylphosphine and increasing the temperature of the solution to 100 – 170 °C, then, $CsSnX_3$ NCs precipitate upon cooling the reaction mixture in an ice-bath.[28]

1.2. Toward stable lead halide perovskites

1.2.1. Phosphor-converted light-emitting diode application

Lead halide perovskite (LHP) NCs have unique optical characteristics in the visible–NIR spectral region, namely, narrow emission bandwidths, high PLQY, tunable color, and an impressively wide gamut of highly saturated colors. These properties make them promising as ideal light emitters for displays, especially phosphor-converted light-emitting diode (pc-LED) applications.[42, 43]

Since 2015, when Protesescu et al. first reported all-inorganic LHP $CsPbX_3$ (X = Cl, Br, I) NCs synthesized in colloidal nanocrystal form via the hot-injection method,[26] these LHP NCs have become the hotspot in quantum dots material research. They are considered more promising in the LED display

applications compared to the conventional semiconductor quantum dots.[44-47] In 2016, Liu et al. fabricated the first on-chip quantum dot liquid crystal display (QLCD) device, which shows a wide color gamut (113%, NTSC).[48] The QLCD was fabricated by mixing green $CsPbBr_3$-mesoporous silica nanocomposite and red $CsPb(Br_{0.4}I_{0.6})_3$ NCs with silicone resin and then coating it on a blue InGaN chip. This study has opened the floodgates to LHP-based backlighting displays. Since then, numerous studies on the different lifting schemes of LHP NCs have been conducted, thus closing the distance to the practical application of on-chip QLCDs (**Figure 1.9**).

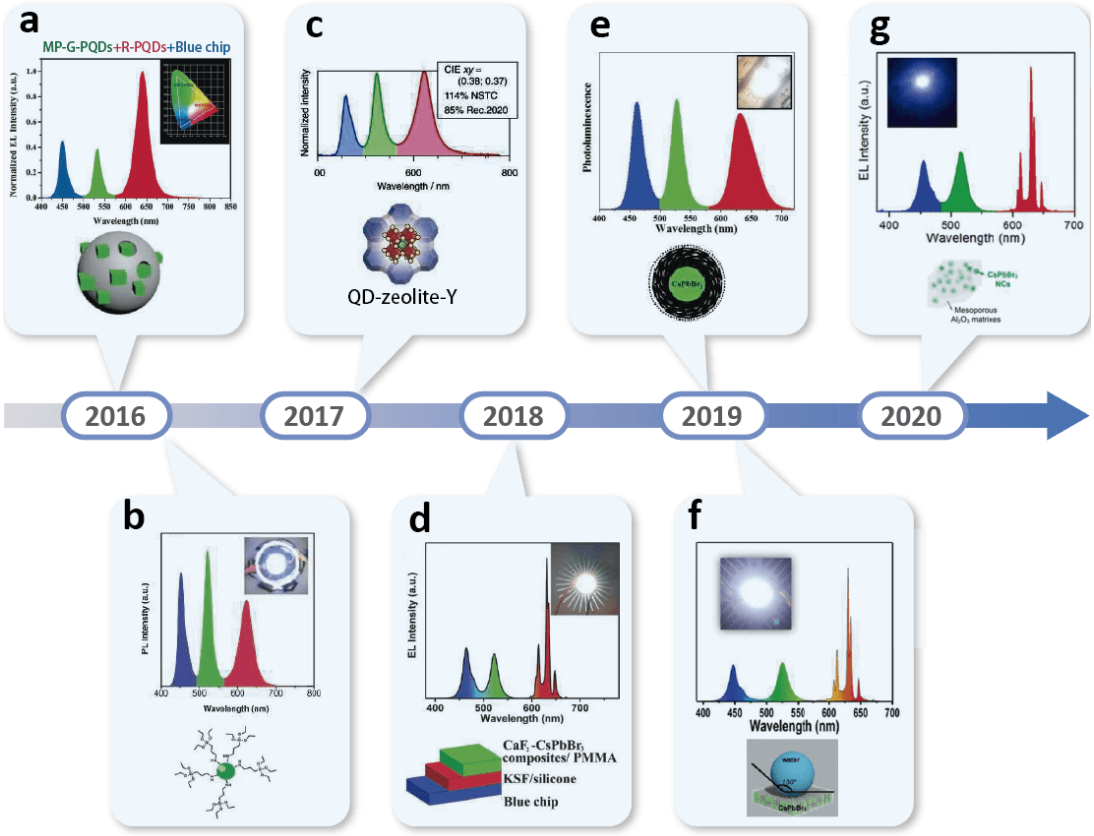

Figure 1.9. Timeline of the applications of LHP NCs in QLCD applications. **(a)** $CsPbBr_3/SiO_2$ composite. Reproduced from ref.[48] Copyright 2016 Wiley-VCH.**(b)** $CsPbBr_3/SiO_2$ composite. Reproduced from ref.[49] Copyright 2016 Wiley-VCH. **(c)** $CsPbX_3$/zeolite-Y composite. Reproduced from ref.[50] Copyright 2017 Wiley-VCH. **(d)** $CsPbBr_3/CaF_2$ composite. Reproduced from ref.[51] Copyright 2018 Wiley-VCH. **(f)** $CsPbBr_3$/polystyrene. Reproduced from ref.[52] Copyright 2019 Wiley-VCH. **(e)** $CsPbBr_3$/poly-divinylbenzene composite. Reproduced from ref.[53] Copyright 2019 American Chemical Society. **(g)** $CsPbBr_3$/mesoporous Al_2O_3. Reproduced from ref.[54] Copyright 2020 American Chemical Society

Two strategies are typically used for implmenting color-converting emitter into a lighting device which lead to two types of pc-LED device called "on-chip" (prototype) and "remote" configurations (**Figure 1.10**).[10, 55] In the "on-chip" configuration, the perovskite NCs emitters are coated directly onto a LED chip, resulting in a substantial heat transfer from the LED chip to the perovskite NCs with a very high local flux of UV or blue light. In the "remote" configuration, the perovskite NCs emitters are placed remotely from the LED light source, i.e., a perovskite NCs film can be placed on the surface area of the luminaire away from the LED chip.[10] In this respect, the remote-type device mitigates the PL degradation caused by thermal, hence higher stability.[49, 56]

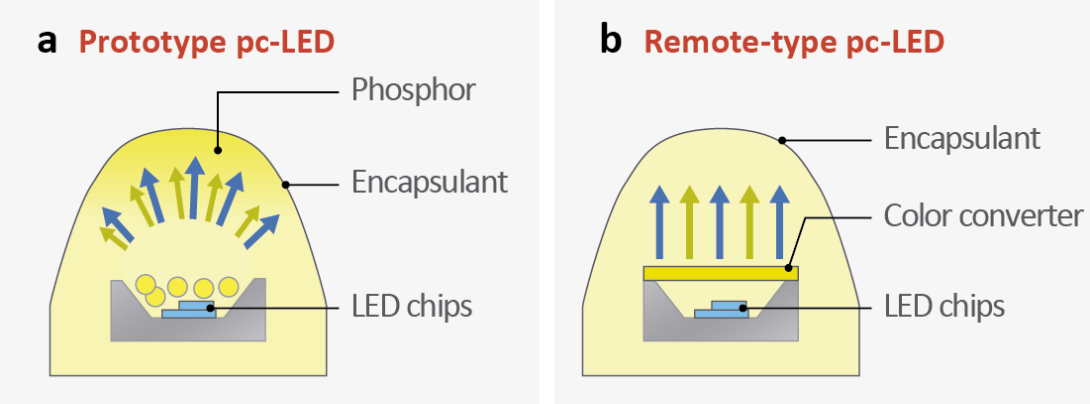

Figure 1.10. Schematic structure of pc-LEDs in 2 types: prototype **(a)** and remote-type **(b)**.

In order to evaluate the technical feasibility of a pre-commercialized pc-LED device, three parameters need to be optimized: luminous efficacy (LE), color rendering index (CRI), and correlated color temperature (CCT).

LE is a quantitative measure of how well a light source produces visible light, considered the headforemost index for pc-LEDs. The luminous flux measures the total power of electromagnetic radiation (including infrared, ultraviolet, and visible light), reflecting the varying sensitivity of human eyes to different wavelengths of light. The luminous efficacy is defined as:

$$\phi_{\text{lum}} = \frac{\phi_{\text{V}}}{\phi_{\text{e}}} = \frac{\int_0^\infty K(\lambda)\phi_{\text{V},\lambda}\,\mathrm{d}\lambda}{\int_0^\infty \phi_{\text{V},\lambda}\,\mathrm{d}\lambda}$$

where $ø_V$ is luminous flux, $ø_e$ is radiant flux, $ø_{e,\lambda}$, is spectral radiant flux , and

K(λ) is spectral luminous efficacy. The standard luminosity function is normalized to a single peak value at 555 nm, and thereby, the combination of a blue LED with a yellow phosphors generally produces an outstanding LE.

The CRI refers to a light source's ability to faithfully reveal the colors of various objects compared to natural light or an ideal source. The high CRI light source illumination gives a more accurate color of objects. The CRI is related to the spectrum of the light source. Sunlight has a CRI of 100. An incandescent lamp has a CRI of close to 100, whereas most pc-LEDs have a CRI of around 80.[57]

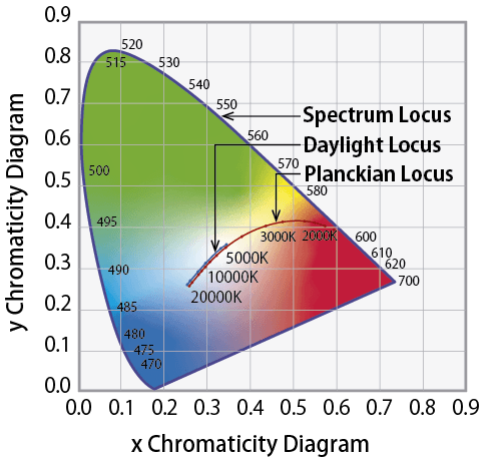

Figure 1.11. CIE 1931 chromaticity diagram.

CCT relates to the temperature of an ideal blackbody radiator that radiates light of a color comparable to that of the light source, measured in Kelvins (K). As the temperature rises, the blackbody radiates from reddish, orange, white, and bluish-white light. Thus, the color of a black body can be simply described by an absolute temperature. By analogy, the color of nearly Planckian (or blackbody) radiators, including a tungsten lamp and sunlight, can be judged by their temperature. At different temperatures, the chromaticities of the Planckian radiator are all in a continuous curve called the Planckian locus (**Figure 1.11**). However, for the light sources that are not Planckian, such as pc-LEDs, color temperature is not a well-defined attribute. Color coordinates of white lights are generated by non-Planckian radiators that do not strictly fall on the Planckian locus but lie near it; in this case, the CCT is used. The CCT is defined as the temperature of the Planckian radiator that is closest to the chromaticity of the

light source, which is extended by vertical lines from the Planckian locus. CCT over 5000 K is called cold white light, while lower CCT is called warm white light.

1.2.2. Environmental stability

Owing to their excellent optical properties, LHP NCs have great potential in lighting applications. However, the poor stability, which leads to their degradation when exposed to humidity, high temperature, and photo-irradiation, limits their commercialization. As an example, under illumination, mixed-halide perovskites ($MAPbI_{3-x}Cl_x$ and $MAPbBr_{3-x}Cl_x$) easily decomposed to hydrocarbons, ammonia gas and PbI_2Cl, Pb, or $PbCl_xBr_{2-x}$,[58] or the surface ligands of $CsPbBr_3$ NCs were easily removed, and the NCs tended to aggregate because of the strong van der Waals attraction forces.[59]

Moisture is the main factor that causes the decomposition of LHP NCs due to the fact that being ionic nature, they are highly soluble in water or other polar solvents. As reported by Leguy et al., in the presence of moisture, a $MAPbI_3$ crystal absorbed H_2O forming the complexes and simultaneously generating PbI_2 at its surface.[60] In the case of $CsPbBr_3$ NCs, H_2O molecules have been found to cause the removal of surface ligands and to promote the subsequent decomposition of the NCs into CsBr and $PbBr_2$.[61, 62] Besides, also oxygen could accelerate the degradation of LHP NCs. Haque et al. proposed probable processes and reactions of photo-oxidation in $MAPbX_3$ NCs as **Equation (1.1)**, **(1.2)**: under photo-irradiation, the photo-excited electrons react with oxygen molecules to form superoxide molecules which react with $CH_3NH_3^+$ to form volatile CH_3NH_2.[63, 64] Then, upon removal of $CH_3NH_3^+$ from the crystal, the $MAPbBr_3$ framework gradually decomposes.[65]

$$CH_3NH_3PbX_3 \longrightarrow CH_3NH_3PbX_3^* \quad (1.1)$$

$$CH_3NH_3PbX_3^* + O_2 \xrightarrow{\text{Deprotonation}} CH_3NH_2 + PbX_2 + \tfrac{1}{2}X_2 + H_2O \quad (1.2)$$

The reliability of this photo-oxidation mechanism is confirmed by X-ray diffraction (XRD) and gas chromatography (GC), which verified the presence of decomposition products. In another work, Lorenzon et al. revealed that the

degradation of $CsPbBr_3$ NCs upon exposure to oxygen is mainly caused by generated nonradiative defects.[66]

High temperature is another factor that induces the degradation of LHPs. The decomposition temperature of organic−inorganic LHPs bulk samples is 220 °C and 250 °C for $MAPbBr_3$ and $MAPbI_3$, respectively, owing to the formation of HX and CH_3NH_2.[67, 68] On the other hand, the decomposition temperature of $CsPbBr_3$ is > 500 °C owing to the collapse of crystal structures.[69] LHP NCs tend to decompose at lower temperatures (~85 °C). In this case, the surface ligands are easily released first, triggering the aggregation and degradation of NCs.[70, 71] Besides the decomposition of the structure under thermal stress, the thermal-induced PL quenching is unavoidable for most types of luminescent materials, (including the commercial phosphor $K_2SiF_6:Mn^{4+}$ [72]). Bulk $MAPbBr_3$ perovskites show severe PL quenching (nearly 100 %) from 300 to 400 K, while the $MAPbBr_3$ NCs preserve 30 % of their initial PL in the same temperature range.[37] $CsPbBr_3$ NCs prepared by the LARP technique show about 85 % PL loss when heated from 80 to 273 K.[73]

In practical applications, all the above factors take effect synergistically, and this represents a major challenge to the stability of perovskite materials. Hence, developing strategies to improve the stability of LHP NCs is highly required to bridge the gap between these materials and their applications.

1.2.3. Encapsulating materials

In the last several years, numerous strategies have been developed to stabilize LHP NCs, including compositional engineering,[74-77] surface engineering[78-81] and matrix encapsulation, [55, 82-86] with significant improvement in the stability of LHP against moisture, temperature and photo-irradiation. This section mainly focuses on reviewing the matrix encapsulation strategies, with a particular focuses on the use of silica as a matrix, which is considered one of the most efficient material to protect LHP NCs.

The encapsulation of LHP NCs inside suitable materials is used to protect

them and mitigating the detrimental effects which arise from the exposure of the NCs to moisure, oxygen, heat and photo-irradiation. Hence the resulting composites have enhanced stability. The encapsulation approaches can be divided into three main types depending on the encapsulation material: organic matrix (polymer), inorganic matrix (metal oxide, i.e., TiO_2, Al_2O_3, SiO_2; metal halide, i.e., $NaNO_3$, CaF_2), and hybrid matrix (metal-organic framework). The combination of two or three of these matrix materials has also been attempted and is referred to as a multi-coating approach.

Polymer encapsulting. Organic polymers with low levels of oxygen and moisture transmission rates have been widely investigated to serve as matrices for embedding HP NCs.[87-90] Li et al. fabricated $CsPbBr_3$ NCs encapsulated in ethylene-vinyl acetate (EVA) matrix via a one-step method by combining the dissolution of the EVA and the supersaturated recrystallization of $CsPbBr_3$ QDs in toluene (**Figure 1.12a**).[82] The PL intensity of $CsPbBr_3$ NCs/EVA composite remained unaltered after 192 h of storage in air and after 240 h of immersion in water (**Figure 1.12c-d**). The good water-resistance of these composites is related to their hydrophobic nature, as evidenced by their large water contact angle of 96° (**Figure 1.12b**).

LHP NCs have been embedded into various polymer matrices using two-step approaches in which pre-synthesized LHP NCs are mixed with desired polymers: poly(methyl methacrylate),[39, 91, 92], polystyrene,[93, 94] poly(styrene-ethylene-butylene-styrene),[93] poly(lauryl methacrylate),[93] and poly(acrylic acid).[95] The so-called "swelling–shrinking" technique is one of the simplest strategies to mix pre-synthesized colloidal NCs with the desired polymer.[94] This approach is based on the fact that polymers swell in a suitable solvent and shrink in a "theta" solvent (a solvent in which polymer coils act like ideal chains).[96] For example, toluene is a "good" solvent, and hexane is a "theta" solvent for polystyrene (PS). LHP NCs/PS composites can be easily obtained by simply dispersing LHP NCs and polystyrene beads in toluene, adding hexane to shrink the polymer.[94] Air stability and water resistance are the most remarkable characters of these reported perovskite/polymer composites.

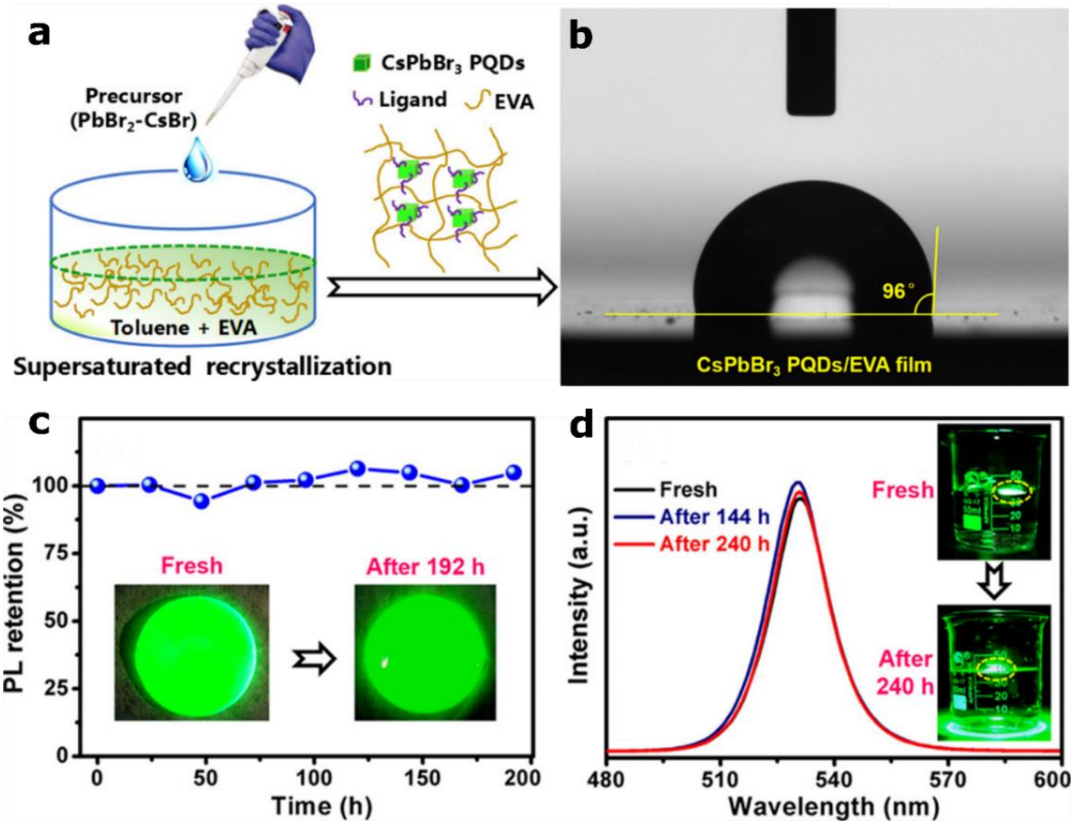

Figure 1.12. **(a)** Schematic of the synthesis procedure of $CsPbBr_3$ QDs/EVA composite, **(b)** contact angle with water, **(c)** PL intensity under the air as a function of retention time, and **(d)** emission spectra after soaking in water. Reproduced from ref.[82] Copyright 2018 American Chemical Society

Metal-organic frameworks (MOFs) encapsulating. MOFs are organic-inorganic hybrid materials with intramolecular pores self-assembled by organic ligands and metal ions through coordination bonds, have also been used in LHP NCs coatings. MOFs possess distinct features, including high porosity (typically micropores < 2 nm), high specific surface area, and tremendous structural diversity.[97-100] Ren et al. adopted MOF-5 as a coating by using templating agents to expand pore size resulting in the sample have giant pores 20-40 nm in size, which is suitable to impregnate LHP NCs.[83] The $CsPbX_3$/MOF-5 composites composites possess a PLQY of 52 % and good stability against moisture (preserving 79.2 % of the initial PL intensity after 60 days of exposure to air), heat (preserving 72.8 % of the initial PL intensity at 80 °C), and photo-irradiation (preserving 71.4 % of the initial PL intensity after 80 h exposing to UV lamp) (**Figure 1.13**).

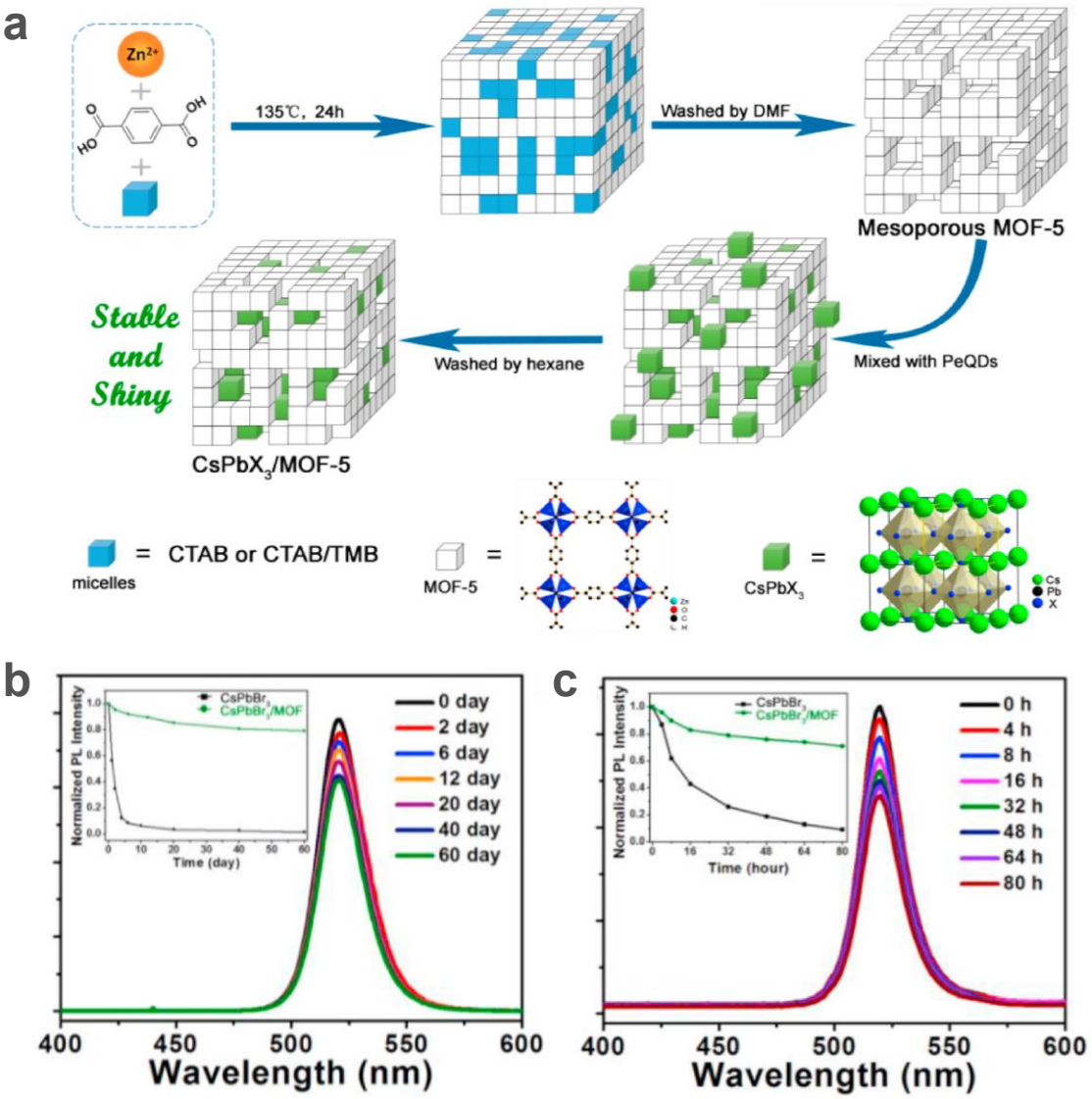

Figure 1.13. (a) Synthesis strategy of the mesoporous MOF-5 crystals and the $CsPbX_3$/MOF-5 composites, **(b)** long-term storage (upper panel) and photo-stability (lower panel) stability test of $CsPbBr_3$/MOF-5. Reproduced from ref.[83] Copyright 2019 Science Direct

Metal halide (inorganic salts) and metal oxides. The ideal protective inorganic matrix should be transparent, nontoxic, and have a low refractive index. As shown in **Figure 1.14a-b**, Yang et al. selected $NaNO_3$ as the coating matrix for $MAPbBr_3$ NCs resulting in a considerably improved stability of $MAPbBr_3/NaNO_3$ composites against thermal and photo-irradiation.[101] Dirin et al. used a multi-step approach to obtain efficient and stable $CsPbBr_3$@KBr/NaBr composites via microcarrier-assisted inorganic shelling.[102] The LHP NCs were first anchored onto preformed KBr crystals/microcrystals, and the resulting composites were coated with an

inorganic shell of NaBr. The stability of the obtained powder against heat was improved remarkably: 65 % of the initial PLQY remains after the exposure of the sample to 80 °C for 190 h. These composites could withstand sonication in pure acetone, acetonitrile, ethanol, N-methylpyrrolidone, γ-butyrolactone, tetramethylurea, and trimethylamine with of 30 % of maximum reduction of the initial PL. In other work, Wei et al. fabricated $CsPbX_3/CaF_2$ composites by impregnating pre-synthesized $CsPbX_3$ NCs into pre-synthesized CaF_2 hierarchical nanospheres in hexane, followed by drying in vacuum at 40 °C. The resulting composites featured a drastically enhanced stability against moisture (preserving 60 % of initial PL intensity after 1 day of storage in the air), light irradiation (retaining 56 % of the initial PL intensity after an 80 h test under UV lamp with 365 nm, 12 W).[51]

The reported LHP/polymer composites are characterized by a high PLQY, good moisture/water resistance, but weak thermal resistance. On the other hand, MOF and metal halides (inorganic salts) used as matrices can provide thermal- and photo-stability, but they do not offer water stability. Conversely, metal oxides can ensure both thermal and water stability to LHP while preserving their high PL emission thanks to their robustness. As shown in **Figure 1.14c-d**, TiO_2-coated $CsPbBr_3$ NCs were synthesized via a facile wet chemical approach by adding titanium precursor (titanium butoxide) into the solution of colloidal $CsPbBr_3$ NCs at 25 °C to form $CsPbBr_3$/TiOx composite, followed by a calcination process at 300 °C for the formation of $CsPbBr_3/TiO_2$ NCs with the tight TiO_2 shell.[103] These $CsPbBr_3/TiO_2$ core−shell nanocomposites had excellent water resistance: PL intensity remained almost constant after soaking the composites in water for more than 12 weeks.

Many other inorganic porous materials, such as Al_2O_3 and SiO_2, have also been reported to be promising shell matrices to protect perovskites.[84, 104, 105]

Multiple coatings, such as $CsPbBr_3$/ mesoporous polystyrene microspheres/ silica,[85] $CsPbBr_3$-dual hollow silica sphere,[106] $MAPbBr_3$/ SiO_2/ poly-(vinylidene fluoride),[107, 108] have also been used synergistically.

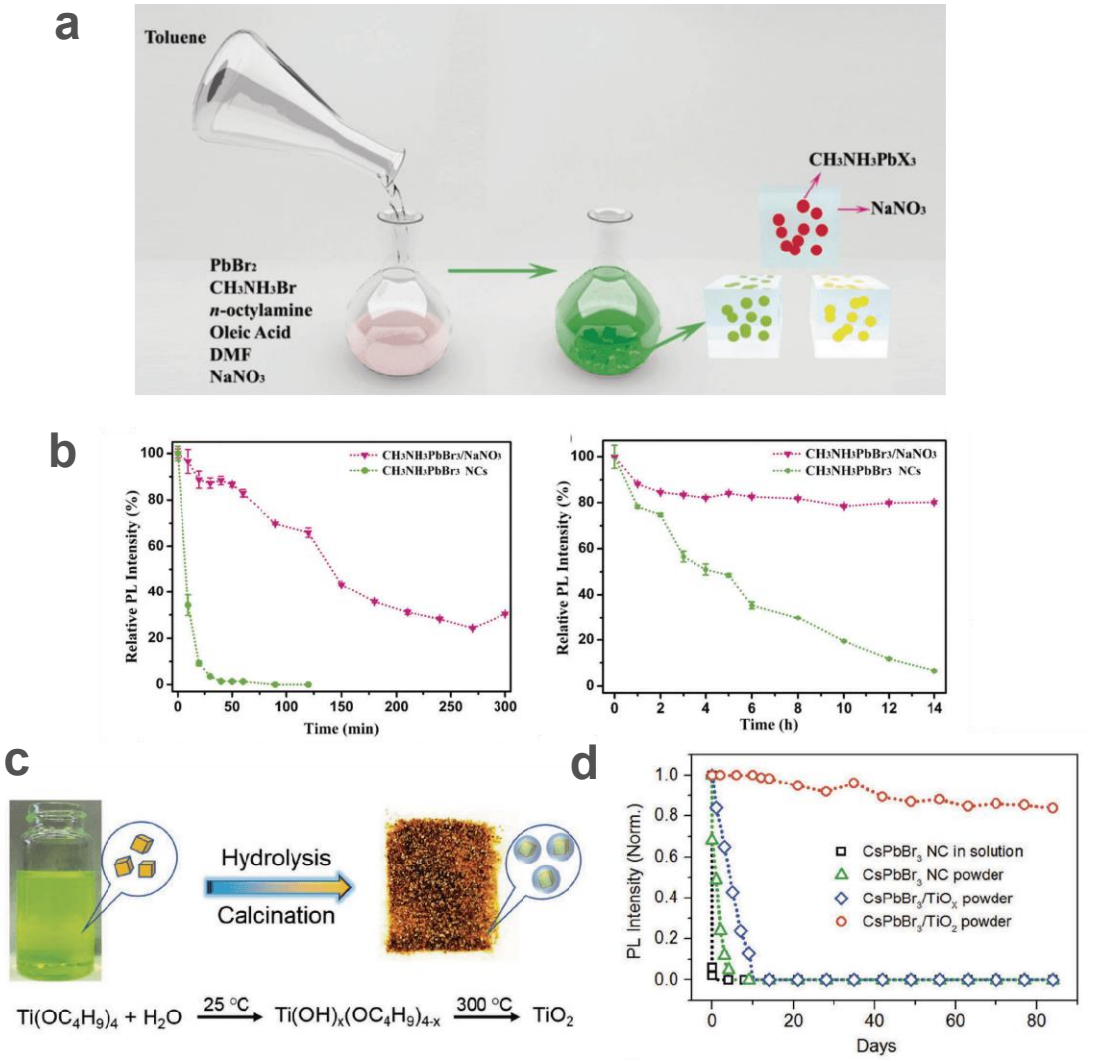

Figure 1.14. (a) Scheme of a one-step reprecipitation procedure for the synthesis of $MAPbBr_3/NaNO_3$ composites, **(b)** Thermal stability (upper panel) and photo-stability (lower panel) test of $MAPbBr_3$ NCs and $MAPbBr_3/NaNO_3$ composites. Reproduced from ref.[101] Copyright 2016 Royal Society of Chemistry **(c)** Schematic illustration of the fabrication process for $CsPbBr_3/TiO_2$ core/shell NCs, **(d)** the relative PL intensity of $CsPbBr_3$ NCs (without precipitation), dried $CsPbBr_3$ NC powder, $CsPbBr_3/TiO_x$ powder, and $CsPbBr_3/TiO_2$ NC powder after immersing in Milli - Q water. Reproduced from ref.[103] Copyright 2018 Wiley-VCH

1.3. Silica encapsulating for lead halide perovskites

Among the different metal oxides, silica (SiO_2) is one of the best candidates for the encapsulation of LHPs due to their properties: i) it is non-toxic, earth-abundant, and cheap; ii) it has excellent thermal and chemical stability; iii) its surface can be easily functionalized (to make it hydrophilic or hydrophobic); iv) it can be made porous (also called mesoporous silica) and the size of the pores

can be control from 2 to 50 nm.

LHP/SiO_2 composites can be fabricated mainly through two routes: (i) direct growth of silica onto LHP and (ii) formation of LHP NCs into pre-synthesized mesoporous silica particles. The "direct growth silica" strategy relies on the formation of a silica shell from silica precursors [e.g., (3-aminopropyl) triethoxysilane - APTES, tetraethoxysilane - TEOS, tetramethoxysilane - TMSO, etc.] onto LHP NCs by several techniques such as LARP[109, 110] and sol-gel route[86, 111] (**Figure 1.15** and **Table 1.1**).

The sol-gel process is based on molecular precursor that undergo hydrolysis and condensation reactions. The method is also economically viable as it can be performed at low temperatures. In a general sol-gel process, a solution of starting chemical precursor for the target material turns to a sol (fine colloidal particles, 10 to 10^3 Å in solution),[112] and at a later stage forms an integrated network (a gel). Three reactions usually occur during the sol-gel process to form silica, as shown below:

$$\equiv Si\text{-}OR + H_2O \longrightarrow \equiv Si\text{-}OH + ROH \quad (1.3)$$

$$\equiv Si\text{-}OR + HO\text{-}Si\equiv \longrightarrow \equiv Si\text{-}O\text{-}Si\equiv + ROH \quad (1.4)$$

$$\equiv Si\text{-}OH + HO\text{-}Si\equiv \longrightarrow \equiv Si\text{-}O\text{-}Si\equiv + H_2O \quad (1.5)$$

The OR group is substituted with an OH group by hydrolysis, in which a metal alkoxide and water react (**Equation 1.3**). Then, the resulting silanol forms a siloxane bond through condensation reactions, and a gel is formed as a network of Si-O bonds is established due to continuous hydrolysis and polymerization (**Equation 1.4** and **1.5**).[113]

As an example, Hu et al. devised a simple method by adding an appropriate amount of TEOS to a solution of freshly synthesized LHP NCs, resulting in the formation of LHP/silica spheres with enhanced stability (**Table 1.1**).[86] In another work, Yin et al. prepared isolated $CsPbX_3/SiO_2$ Janus nanoparticles via a water-triggered transformation process combined with a sol-gel protocol

(**Figure 1.15b**).[111] In detail, Cs_4PbBr_6 NCs were transformed into $CsPbBr_3$ NCs via the use of DI water which, at the same time, triggered the hydrolysis of TMOS, which leads to the formation of the SiO_2 shell. The stability of $CsPbBr_3/SiO_2$ nanoparticles was remarkably enhanced: 80 % of the PL intensity of nanoparticles was retained after 7 days of immersing in water (**Table 1.1**).

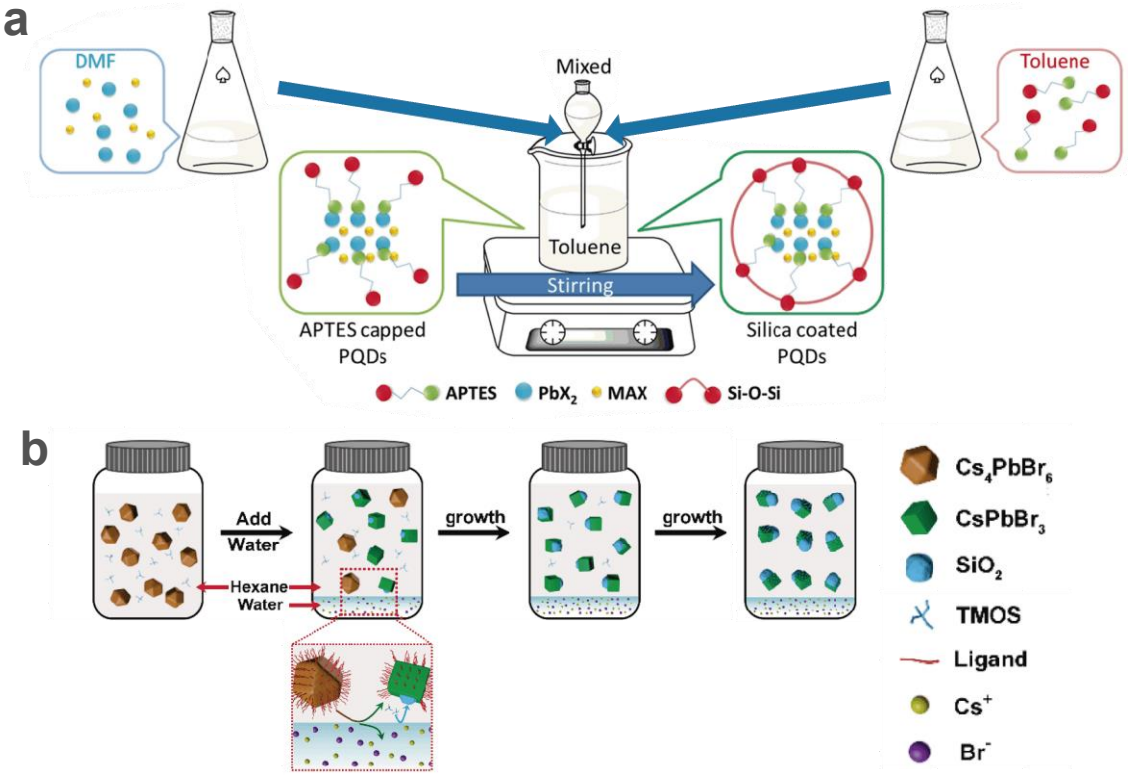

Figure 1.15. The "direct growth silica" strategy for LHP/SiO_2 composites via Ligand-assisted Reprecipitation method **(a)** or sol-gel route **(b)**. (a) reproduced from ref.[109] Copyright 2018 American Chemical Society and (b) reproduced from ref.[111] Copyright 2018 American Chemical Society

The direct growth of silica onto LHPs, however, is challenging due to the degradation or dissolution of LHP NCs during the growing process. Accordingly, another possible strategy to fabricate LHP/SiO_2 is introducing LHP NCs into the pre-synthesized silica matrix. In a straightforward way, Liu et al. simply blended pre-synthesized $CsPbBr_3$ NCs with mesoporous silica (m-SiO_2), resulting in composites with enhanced stability at high temperature and under photo-irradiation (**Table 1.1**).[48] It is worth highlighting that LHP NCs can be grown directly inside m-SiO_2 by simply immersing silica in the solution of precursors (e.g., CsBr, $PbBr_2$ for the formation of $CsPbBr_3$) and then by evaporation of the solvent.[114] In another work, Chen et al. devised a colloidal

synthesis method to produce $CsPbBr_3$/m-SiO_2 nanocomposite:[115] m-SiO_2 was first heated up to 120 °C under N_2 in a mixture of oleic acid, oleylamine, and octadecene; afterward, $PbBr_2$ was added to the mixture and, finally, a cesium oleate precursor solution is injected at 180 °C to trigger the nucleation of the $CsPbBr_3$ NCs. The resulting composites exhibit a bright PL emission (PLQY of 83 %) and an enhanced stability against thermal and photon-irradiation (**Figure 1.16** and **Table 1.1**). In yet another work, Zhang et al. recently devised a synthesis approach to produce $CsPbBr_3$/m-SiO_2 composites, which was achieved by mixing $PbBr_2$ and CsBr salts with silica and heating everything up to 600-700 °C.[116] The high annealing temperature leads to the collapse of SiO_2 pores, resulting in the encapsulation of $CsPbBr_3$ inside a thick SiO_2 matrix. The PL emission of the sample retained almost constant after immersing in water and acid for 50 days or after exposing to blue LED (455 nm, 20 mA, 2.7 V) for 1000 h (**Table 1.1**).

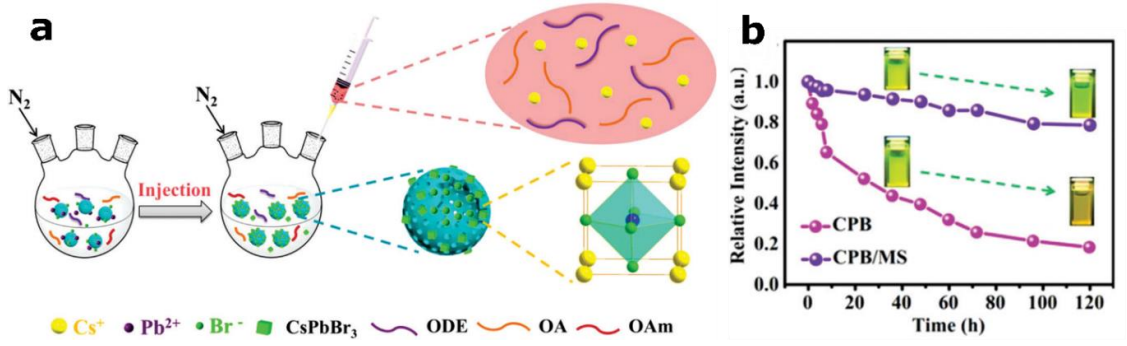

Figure 1.16. (a) Schematic of the colloidal synthesis process for the $CsPbBr_3$/m-SiO_2 nanocomposite. **(b)** Photo-stability of $CsPbBr_3$/m-SiO_2 nanocomposite. After 120 h exposed to UV light (365 nm), the $CsPbBr_3$ NCs retain ~16 % of the initial PL intensity. In contrast, the $CsPbBr_3$/m-SiO_2 nanocomposites retain ~80 % of the initial PL intensity thanks to protecting the m-SiO_2 shell. The insets show that the $CsPbBr_3$/m-SiO_2 solution is still yellow-green after irradiation, distinguished from the yellow $CsPbBr_3$ NCs solution. Reproduced from ref.[115] Copyright 2019 American Chemical Society.

Overall, silica has been shown to be an efficient material for the encapsulation of LHPs NCs with remarkable enhanced stability. However, the LHP/SiO_2 composites reported so far have not met the requirement of high PLQY (at least 80 %) and, at the same time, high stability in harsh conditions, including high salinity, temperature and low pH. For these reason, the use of

these composites in numerous applications such as optoelectronic devices, high energy radiation detectors, solar concentrators,[117, 118] or as tracers/emitters in bio-imaging for clinical purposes[119, 120] or crude oil extraction,[121] has not yet achieved. Therefore, developing new approaches for LHPs encapsulation is desired in order to implement these materials to applications.

Table 1.1. Synthesis method and enhancement in stability and applications of LHP NCs/silica composites.

LHP NCs/silica composite	Method		PLQY	Stability in moisture, chemical, thermal, and photo-irradiation	Application
	Silica growth	LHPs growth			
$MAPbBr_3/SiO_2$[109] (In solution at RT)	In-situ with APTES	In-situ LARP in DMF	91 %	~94 % after 72 h in air ~66 % after 30 min at 60 °C ~50 % in ethanol	WLED power efficiency 54 lm/W
$CsPbBr_3@s_4PbBr_6/SiO_2$[110] (In solution at RT)	In-situ with APTES	In-situ LARP in DMSO	84.5%	~100 % after 10 cycles at 150 °C (6 % after 50 cycles) ~91 % after 2 months in air with RH 50%	triple-mode anti-counterfeiting
$CsPbBr_3/SiO_2$[86] (In solution at 165 °C)	In-situ with TEOS	Pre-synthesized	N/A	~73.8 % after 12 h in air with RH 75% ~36.4 % after 15 h at 60 °C	N/A
$CsPbBr_3/SiO_2$[111] (In solution at RT)	In-situ with TMOS	In-situ, transformed from Cs_4PbBr_6	80 %	~80 % after 7 days in water ~98 % after 5 min continuous illumination with a 375 nm LED light (117 mW/cm^2) at 40 °C	WLED with 1 h stable of white emission
$CsPbBr_3/m\text{-}SiO_2$[48] (In solution at RT)	Pre-synthesized	Pre-synthesized	55 %	~80 % after 96 h under continuous UV (365 nm, 6 W) irradiation ~95 % after 1 cycle at 100°C	WLED (no info. of operation)
$CsPbBr_3/m\text{-}SiO_2$[115] (In solution at 180 °C)	Pre-synthesized	In-situ hot injection	83 %	~80 % after 120 h exposing to UV light (365 nm) No anion exchange with $ZnCl_2$	WLED, ~100 % PL after 10 h continuous operation
$CsPbBr_3/SiO_2$[122] (Solid state at 700 °C)	Pre-synthesized	In-situ	63 %	~100 % after 50 days in water and acid ~100 % after 168 h at 85 °C in RH 88 % ~100 % after 1000 h under blue LED chips (455 nm, 20 mA, 2.7 V)	N/A

1.4. Lead-free tin halide perovskites

Despite the promising results obtained by employing lead halide perovskites in optoelectronic applications, the toxicity of Pb-based halide perovskites is a critical problem that makes them still not ready for commercialization.[123-125] To address this toxicity issue, much recent research has attempted toward environmentally friendly materials by exploring new compounds to substitute lead with less-toxic elements, e.g., tin,[126-132] germanium,[7, 133-135] bismuth,[136-139] antimony,[140-142] or palladium.[143] Among them, tin (Sn) perovskite is the most potential candidate. Due to the higher electronegativity of Sn, Sn-based HPs have a narrower band-gap compared to their Pb-based counterparts, so they are potentially better light harvesters.[144-147] Tin iodide-based perovskite compounds exhibit direct band gaps around 1.2–1.4 eV, negligible exciton binding energies (25 meV, lower than the thermal energy at room temperature), high carrier mobility (up to 2320 cm^2 V s^{-1} for the electron mobility, and 322 cm^2 V s^{-1} hole mobility) and long carrier diffusion lengths of over 500 nm.[128, 148-150] All these properties are highly desirable for solar cell applications. Shuzi et al. recently fabricated tin iodide-based perovskite solar cell (PSC) with the highest efficiency of 13.24 % by using mixed cations having the chemical composition of GeI_2-doped $(FA_{0.9}EA_{0.1})_{0.98}EDA_{0.01}SnI_3$.[130]

However, Sn-based HPs, suffer from severe chemical instability that heavily hampers the investigation of their optical properties. Under ambient conditions, Sn^{2+} easily oxidizes into Sn^{4+}; the problem of oxidation is even more pronounced in NCs because of their higher surface-volume ratio. This undesired transition is followed by the generation of trap states that irreversibly deteriorate the photoluminescence emission properties of the NCs, thus suggesting a defect-intolerant nature of tin-based perovskites. In order to overcome these problems, replacing Sn^{2+} with Sn^{4+} is a possible strategy to avoid the oxidation of Sn^{2+}, i.e., use $Cs_2Sn^{(IV)}I_6$ instead of $Cs_2Sn^{(II)}I_3$ perovskites (**Figure 1.17**). In the Cs_2SnI_6 perovskite derivative, the B-sites are alternatively occupied by a tetravalent ion and vacancies, and the BX_6 octahedra result whereby to be isolated one from the another.[127, 151, 152]

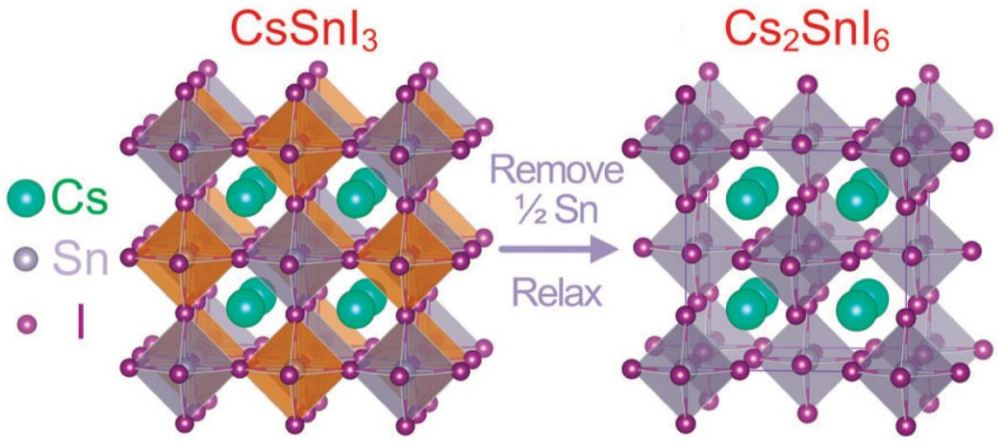

Figure 1.17. Crystal structure of Cs_2SnI_6, which is obtained by removing half of the Sn atoms at intervals, i.e., the edge centers and the body center of $CsSnI_3$. Reproduced from ref.[153] Copyright 2015 Royal Society of Chemistry.

Bulk Cs_2SnI_6 thin film is first investigated by Lee et al. and exhibited an excellent band-gap of 1.3 eV and a high air-stability. The corresponding solar cell is made by using this Cs_2SnI_6 has a power conversion efficiency (PCE) of 7.8 %.[126] Besides, Cao et al. synthesized a Cs_2SnI_6 absorber with a direct band-gap of 1.48 eV and the PCE of the corresponding solar cell is about 1 %.[132, 154] Later, Cs_2SnI_6 crystals in nanoscale have been reported with interest in PL emission and varied band-gap dependent particle size.[131, 155-157] For instance, Cs_2SnI_6 NCs with a band-gap of 2.0 eV and a PL emission at 630 nm were obtained via a hot injection method with anticipation ligands (oleic acid and oleylamine cooperatively).[131] Dolzhnikov et al. reported a hot injection synthesis without organic capping ligands that delivers the Cs_2SnI_6 NCs with size-dependent band gaps (as the band-gap increases from 1.38 eV to 1.47 eV with decreasing of particles size).[155] Moreover, the band-gap of Cs_2SnI_6 depends on the particle size and the shape of particles when going from quantum dots to nanosheets or nanorods.[156] Overall, contradictory conclusions concerning the band-gap were reported by various research groups and thought to originate from the different shapes of the Cs_2SnI_6 nanostructures.

Besides the 3D structure of tin-based perovskites, recently, tin-based 2D perovskites also have attracted increasing attention in optoelectronic applications, including solar cells, LEDs due to being more moisture-resistant

than their 3D perovskite analogues.[158, 159] For example, Cao et al. fabricated 2D Sn-based $(BA)_2SnI_4$ (BA = $C_4H_{10}NH_2^+$) solar cells with a significantly enhanced stability compared to 3D $MASnI_3$ – based solar cells.[158] In terms of LED applications, some groups successfully employed 2D Sn-based perovskite to a LED such as $(PEA)_2SnI_4$ (PEA = $C_8H_9NH_3^+$)[160] and $(OAm)_2SnBr_4$ (OAm = $C_{18}H_{35}NH_3^+$).[161]

Although recent efforts have significantly advanced the research in Sn-based 2D perovskites, the knowledge and understanding of their structure and optical property are still very limited. Therefore, it is necessary to understand these materials before employing them in practical applications fully.

1.5. Motivation of the thesis

This thesis mainly focuses on developing different encapsulation strategies for lead halide perovskites to produce robust and stable light-emitting composites. The work focuses on optimizing photoluminescence quantum yield, and the PL emission (via compositional control) of these LHP/SiO_2 composites. Moreover, motivated by the importance of LHP/SiO_2 composites for practical applications, these composites are tested in several devices such as white-LED in various configurations ("on-chip" or "remote" prototype). Furthermore, some preliminary results about the structure and optical properties of lead-free tin-based perovskites, including Cs_2SnI_6 3D perovskite and $(C_{18}H_{35}NH_3)SnI_4$ 2D perovskite, will be discussed, extending the scope of this work to environmentally-friendly materials.

CHAPTER 2

$CsPbX_3/SiO_x$ composites production via sol-gel method

Abstract: *As shown in chapter 1, silica (SiO_2 or SiO_x) is a promising candidate for the encapsulation of lead halide perovskites. Via a sol-gel method, facile synthesis of composite powders composed of $CsPbX_3$ nanocrystals (NCs) embedded in silica has been developed to be showing in this chapter. The synthesis starts from colloidal Cs_4PbX_6 NCs, which are mixed with silica precursor (tetraethyl orthosilicate) in the presence of HNO_3, which triggers the sol-gel reaction yielding the formation of SiO_x and the conversion of the starting $Cs4PbX_6$ NCs into $CsPbX_3$ ones. The resulting $CsPbX_3/SiO_x$ composite powders exhibit enhanced remarkable stability against water and high temperature (120 °C). After that, these composites are used as down-converter phosphors on top of a blue light-emitting diode (LED). The resulting device has nearly ideal white light emission with the Commission Internationale de l'Eclairage (CIE) color coordinates (0.32, 0.33).*

Parts of this chapter have been adapted or reproduced with permission from ref.[162]

2.1. Introduction

Among various methods to embed NCs material into silica matrixes,[167-170] the sol-gel route is the most employed one. To accelerate the sol-gel reaction, protic acids are commonly employed that are typically a water-based solution of mineral acids, such as HNO_3.[167] However, LHP NCs are not compatible with these mineral acids nor with sol-gel routes as they readily dissolve in water (which is produced during the sol-gel process itself). The sol-gel procedures reported so far for the encapsulation of LHPs in SiO_x do not employ any acid catalyst, thus resulting in a slow hydrolysis reaction that intensifies the degradation of the LHP NCs.[168-170] For these reasons, no LHP/SiO_2 bulk nanocomposites prepared by sol-gel routes have been reported so far.

This chapter presents a novel acid-catalyzed sol-gel method that delivers SiO_x coated $CsPbX_3$ NCs starting from Cs_4PbX_6 NCs. It has been shown that

water can drive the transformation of Cs_4PbX_6 (0D) into $CsPbX_3$ (3D) NCs.[171] Motivated by these findings, an aqueous HNO_3 solution is employed not only for producing 3D NCs starting from the corresponding 0D NCs ones but also simultaneously triggering the rapid hydrolysis of TEOS which leads to the growth of a silica matrix fully embedding the final NCs. The preparation of 0D Cs_4PbX_6 NCs and the production of $CsPbX_3/SiO_x$ composites are described in *sections 2.2, 2.3,* and *2.4*. The $CsPbBr_3/SiO_x$ composite is then selected as a case study for the stability test against heat and humidity (*section 2.5*). Finally, *section 2.6* shows the results of applying these composite materials as down converter luminophores in a white light-emitting diode (W-LED).

2.2. Preparation of 0D Cs_4PbX_6 NCs

First of all, the 0D Cs_4PbX_6 NCs, including $Cs_4Pb(Cl/Br)_6$, Cs_4PbBr_6, and $Cs_4Pb(Br/I)_6$ NCs, are synthesized by a hot injection colloidal approach.[172] Typically, the mixture of $PbBr_2$, ODE, OA, and OLAM is heated to 150 °C. After the complete dissolution of the $PbBr_2$ salt, the solution is cooled down to 80 °C, and the Cs-oleate solution in OA is swiftly injected into the solution. The mixture becomes turbid white after 30 seconds and is quickly cooled down to RT, readily collecting 0D Cs_4PbBr_6 NCs. The Cl/Br-and Br/I- based compositions are also synthesized using a similar method by mixing halide precursors (see **Table 2.1** in the *experimental part*). Their compositions are determined as $Cs_4PbCl_{4.12}Br_{1.88}$ (**Figure 2.1**) and $Cs_4PbBr_{0.97}I_{5.03}$ (**Figure 2.2**) by SEM-EDS analysis.

The structure of these 0D NCs is then characterized by XRD analysis showing the matching with corresponding bulk hexagonal phases (**Figure 2.3**). These 0D NCs have an average size of 16 nm, 13 nm, and 22 nm for $Cs_4Pb(Cl/Br)_6$, Cs_4PbBr_6, and $Cs_4Pb(Br/I)_6$ NCs, respectively, (**Figure 2.3c-e**) and are characterized by a narrow optical absorption peak at high energies (300-360 nm) as seen from their absorbance spectrum (**Figure 2.3b**).

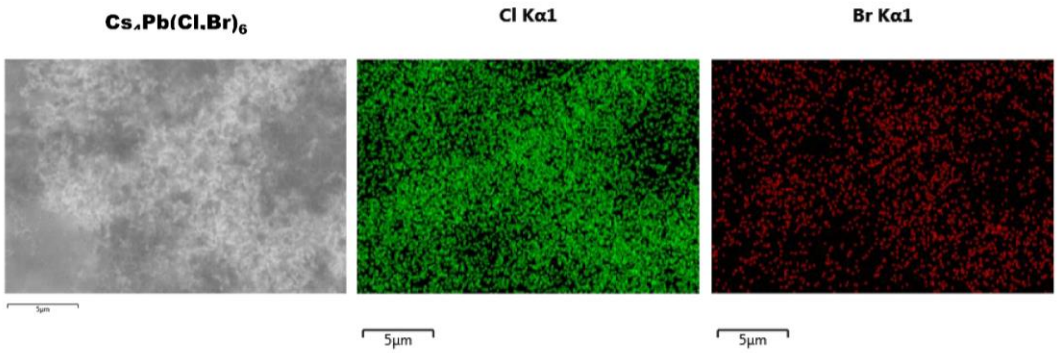

$Cs_4Pb(Cl,Br)_6$	Atomic %
Cl	68.70
Br	31.30
Total	100.00

Figure 2.1. SEM-EDS elemental mappings of the halide anions of 0D $Cs_4Pb(Cl,Br)_6$ NCs system. The chlorine and bromine distribution is visualized in the top panels.

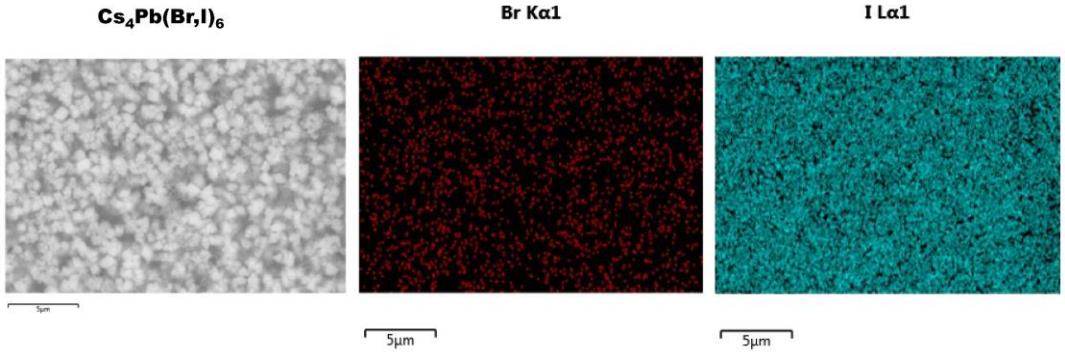

$Cs_4Pb(Br,I)_6$	Atomic %
Br	16.18
I	83.82
Total	100.00

Figure 2.2. SEM-EDS elemental mappings of the halide anions of 0D $Cs_4Pb(Br,I)_6$ NCs system. The bromine and iodine distribution is visualized in the top panels.

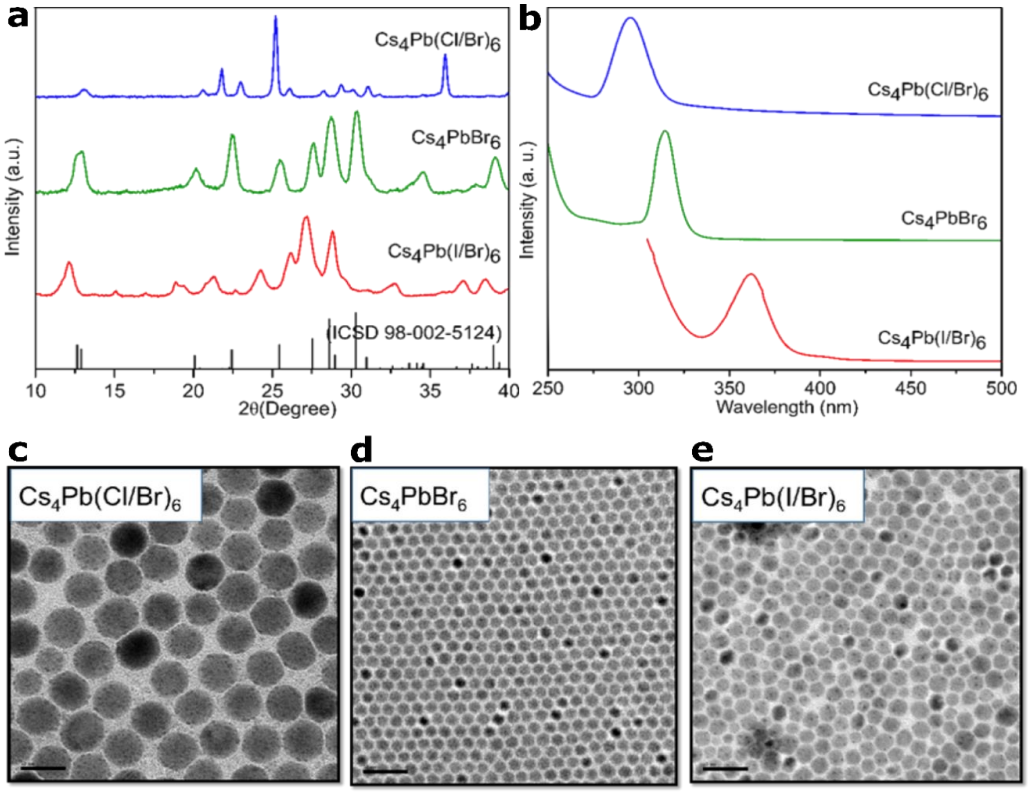

Figure 2.3. Characterization of 0D Cs_4PbX_6 NCs: XRD patterns **(a)**, optical absorption spectra **(b)**; TEM images **(c-e)**. The reference XRD pattern in (a) belongs to the bulk Cs_4PbBr_6 hexagonal phase (ICSD 98-002-5124). All TEM images have scale bars of 50 nm (c-e).

2.3. The synthesis of $CsPbX_3/SiO_2$ composites

Three composite materials are prepared, namely $CsPb(Cl,Br)_3/SiO_x$, $CsPbBr_3/SiO_x$, and Mn-doped $CsPb(I,Br)_3/SiO_x$. Briefly, the as-prepared 0D Cs_4PbX_6 NCs react with TEOS and an HNO_3, aqueous solution forming the corresponding $CsPbX_3/SiO_x$ composites result in the form of luminescent gels that are then dried to flakes and ground into powders **(Figure 2.4)**. It is worth emphasizing here that in the case of $CsPb(Br,I)_3/SiO_x$ composite synthesis, a small amount of Mn^{2+} ions is employed (see the *experimental part* for details) to improve the stability of the resulting sample.[173] Indeed, in the absence of Mn^{2+} ions, the sol-gel process results in a non-luminescent material (see **Appendix 2.1**).

The sol-gel route in this work can be described as a one-step approach in which two "main" reactions occur concomitantly:

i) the water-induced transformation of 0D to 3D NCs;[171]

$$Cs_4PbX_6 \xrightarrow{\text{aq. } HNO_3} CsPbX_3 + 3\ CsX \quad (2.1)$$

ii) the gelation of TEOS, which is catalyzed by HNO_3:

$$Si(OC_2H_5)_4 + 4\ H_2O \Longleftrightarrow Si(OH)_4 + 4\ C_2H_5OH \quad (2.2)$$

$$n\ Si(OC_2H_5)_4 + n\ Si(OH)_4 \Longleftrightarrow (-SiO_2-)_n + 4n\ C_2H_5OH \quad (2.3)$$

$$n\ Si(OH)_4 + n\ Si(OH)_4 \Longleftrightarrow (-SiO_2-)_n + 4n\ H_2O \quad (2.4)$$

As a control experiment, 3D $CsPbBr_3$ NCs are employed instead of 0D Cs_4PbX_6 NCs as the starting precursor in the sol-gel procedure. In such an experiment, the NCs completely degrade (**Appendix 2.2**), indicating that the use of Cs_4PbX_6 NCs is essential in this sol-gel method.

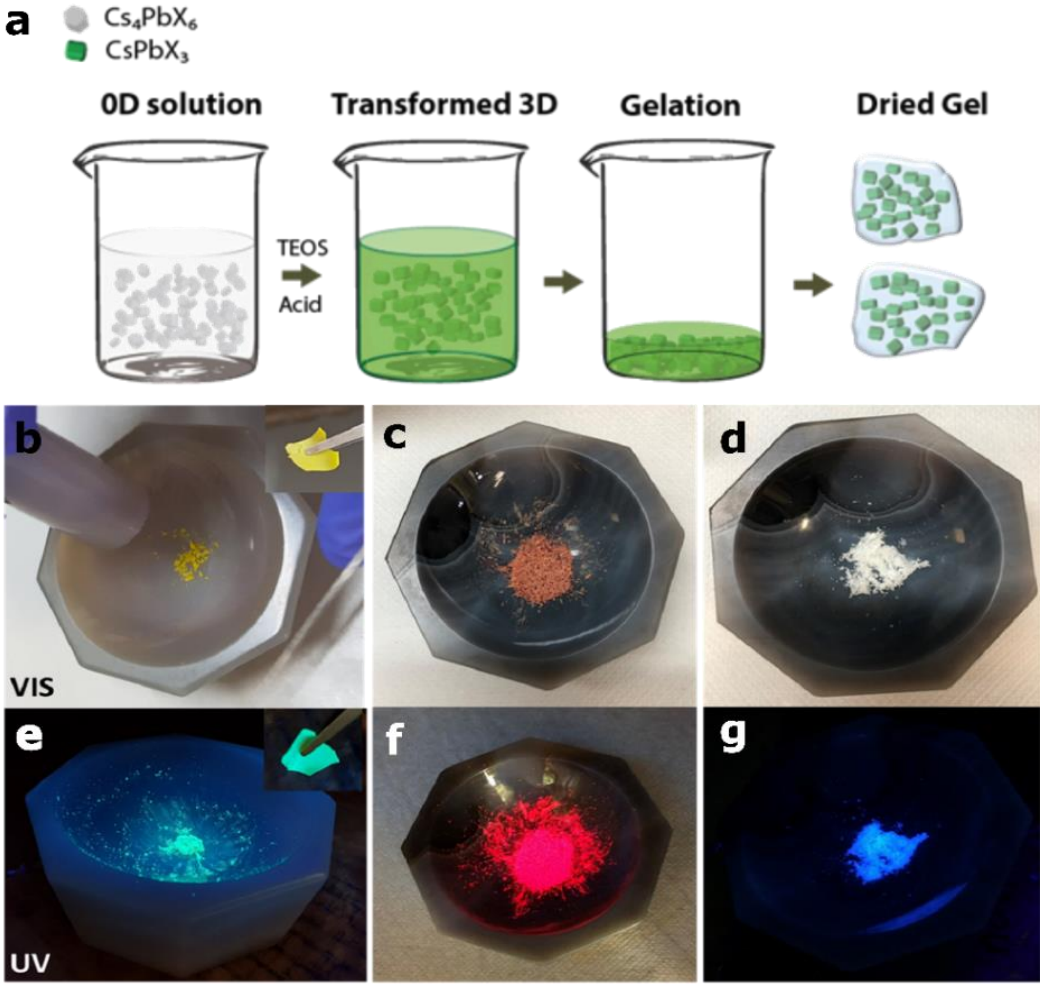

Figure 2.4. (a) The production of $CsPbX_3/SiO_x$ monoliths via a sol-gel route with the concomitant transformation of Cs_4PbX_6 NCs. **(b-g)** The photographs of green, red, and blue-emitting composite powders under daylight (b-d) and 345nm UV lamp (e-g). The insets show the as-prepared flake of $CsPbBr_3/SiO_x$ composite.

2.4. Characteristic of $CsPbX_3/SiO_x$ composites

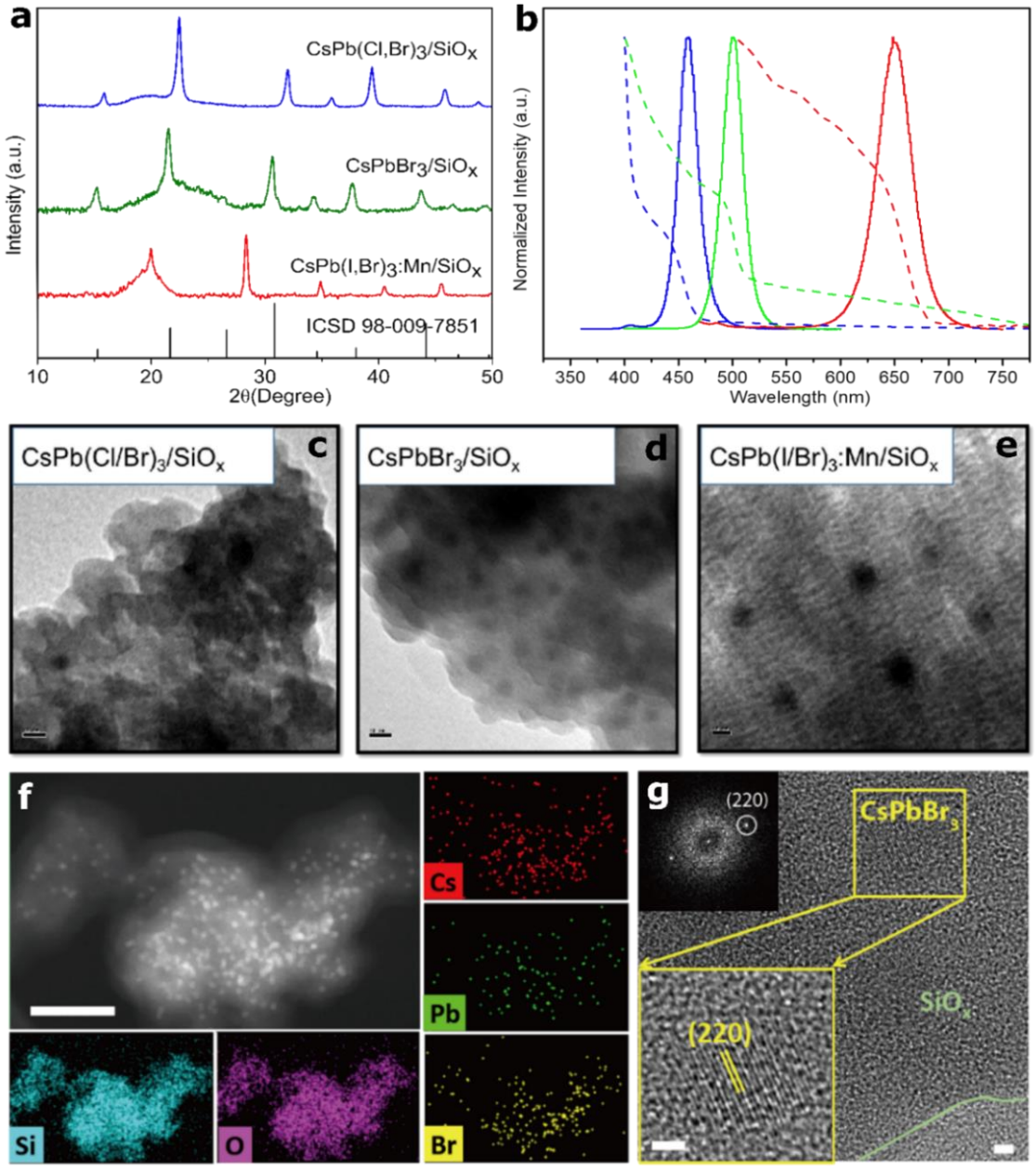

Figure 2.5. (a) XRD patterns of $CsPbX_3/SiO_x$ composite powders and bulk orthorhombic $CsPbBr_3$ (ICSD 98-002-5124). **(b)** Absorption (dash line), PL spectra (solid line) of $CsPb(Cl/Br)_3/SiO_x$ (blue curve), $CsPbBr_3/SiO_x$ (green curve) and $CsPb(I/Br)_3$:Mn/SiO_x (red curve) composite powders. **(c-e)** TEM images of $CsPbX_3/SiO_x$ composite powders. Scale bars are 10 nm in all TEM images. **(f)** HAADF-STEM image and the corresponding elemental maps showing the distribution of Cs, Pb, Br, Si, O. Scale bar is 100 nm. **(g)** HRTEM image of a $CsPbBr_3$ NC inside the SiO_x matrix. The scale bar is 2 nm. Insets are the corresponding FFT and magnified view of the particle.

The green-emitting $CsPbBr_3/SiO_x$ composite exhibits an absorption onset at 490 nm and a green PL emission peaked at 510 nm with a FWHM of 23.8 nm (114 meV). The $CsPb(Cl,Br)_3/SiO_x$ sample has a blue PL emission at 460 nm with an FWHM of 22.6 nm (133 meV), while the Mn-doped $CsPb(Br,I)_3/SiO_x$ composite has a red emission centered at 645 nm with an FWHM of 39.6 nm (117 meV) (**Figure 2.5b**). The XRD patterns of these composites are not characterized by reflections ascribable to the starting 0D structure, nor secondary undesired phases, confirming that 0D NCs are fully converted into the corresponding 3D structures (**Figure 2.5a)**. TEM micrographs, TEM-EDS elemental maps, and HR-TEM analysis reveal that these composites consist of newly formed 3D NCs embedded in an amorphous silica matrix (**Figure 2.5 c-g**, **2.6**).

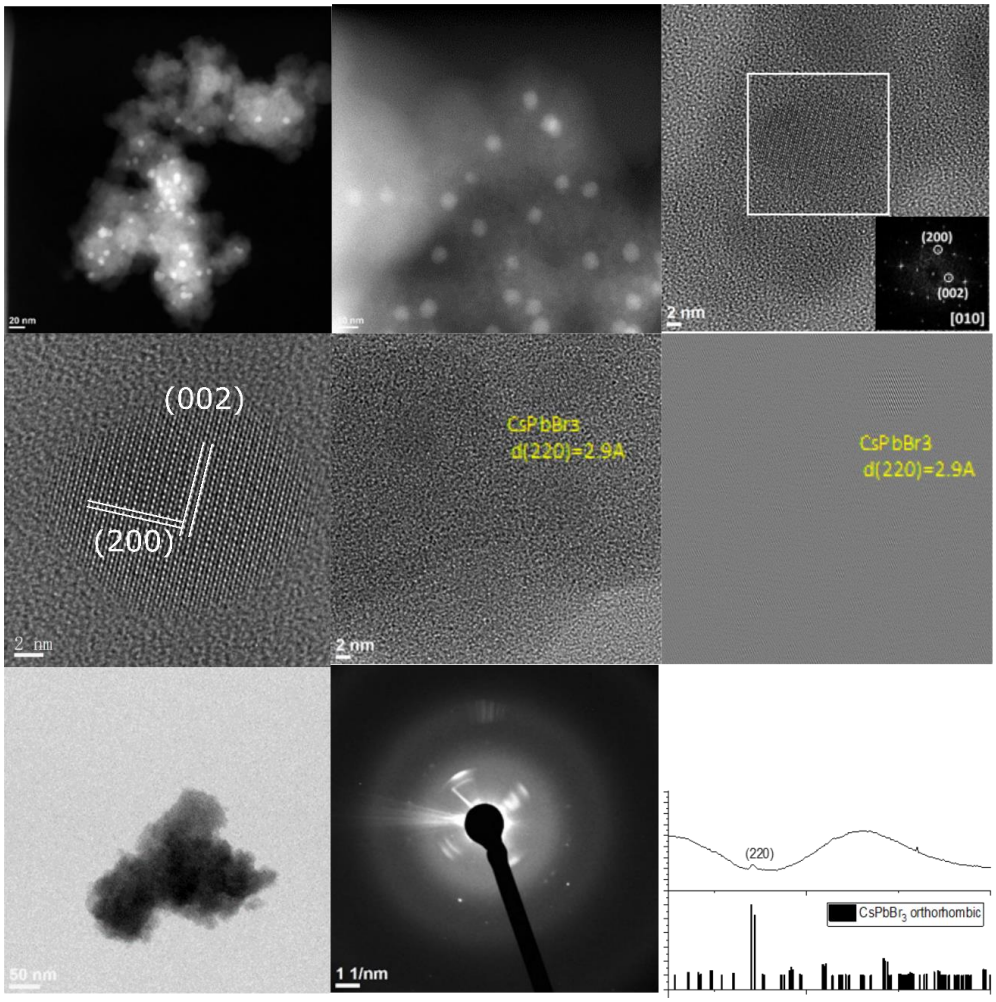

Figure 2.6. HAADF-STEM images, HR-TEM images, and filtered HR-TEM image (inset shows the FFT analysis), SAED pattern, and corresponding Azimuthal integration compared to reference cards orthorhombic $CsPbBr_3$ phase of $CsPbBr_3/SiO_x$ composite.

2.5. Stability of $CsPbBr_3/SiO_x$ composite against heat and water

After assessing the effective encapsulation of $CsPbX_3$ NCs in the SiO_x matrix, the stability of the $CsPbBr_3/SiO_x$ composite is tested against heat and water. For comparison, the stability test is also performed with oleylammonium bromide passivated $CsPbBr_3$ NCs prepared following the approach of Protesescu et al.,[26] and denoted here as "bare" NCs. The thermal stability is assessed by monitoring the PL intensity of films (prepare from the $CsPbBr_3/SiO_x$ composite powder sample) during successive heating and cooling cycles (from RT to 120 °C, 1 hour/cycle).

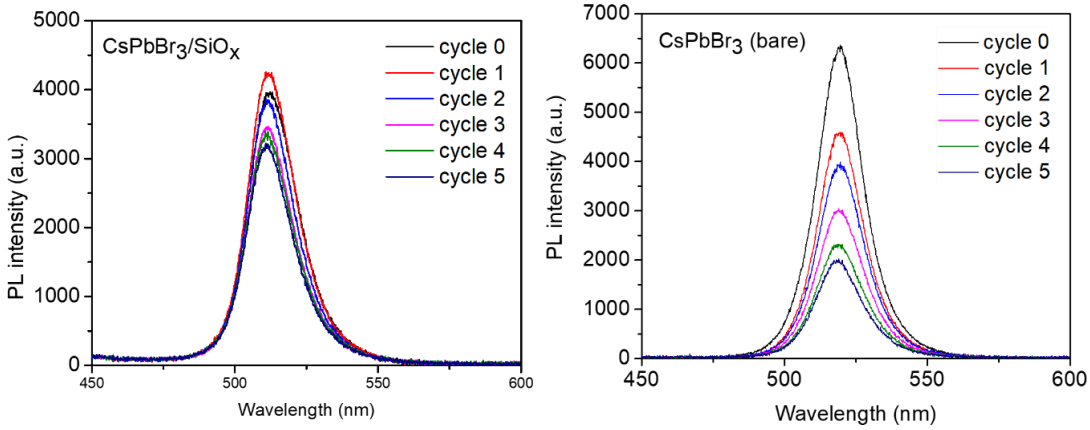

Figure 2.7. PL spectrum of $CsPbBr_3/SiO_x$ composite (left panel) and bare $CsPbBr_3$ NCs (right panel) are recorded at RT after each heat-up/cool-down cycle.

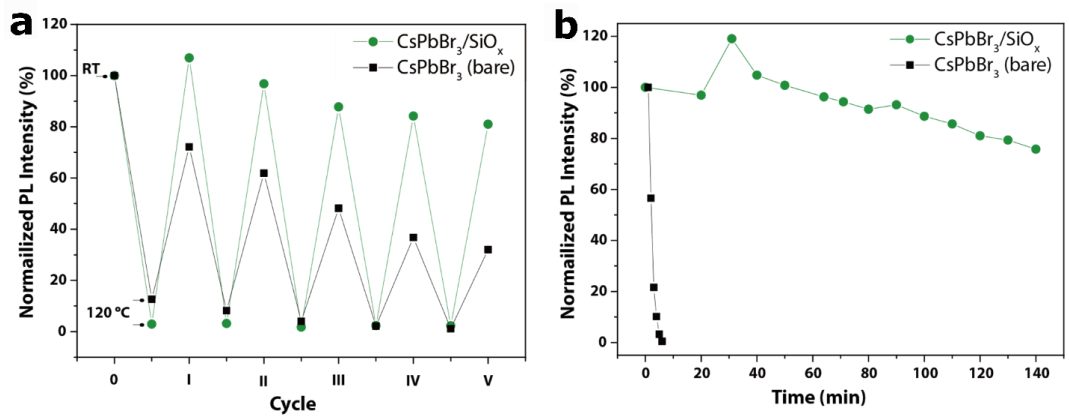

Figure 2.8. (a) Thermal stability test: heating and cooling cycling measurements of bare $CsPbBr_3$ NCs and $CsPbBr_3/SiO_x$ composite. **(b)** Water stability test: PL intensity changes of bare $CsPbBr_3$ NCs and $CsPbBr_3/SiO_x$ are monitored during those are exposed to water under stirring.

As shown in **Figure 2.7** and **Figure 2.8a**, the PL of both samples, $CsPbBr_3/SiO_x$ composite and bare $CsPbBr_3$ NCs, are quenched upon increasing the temperature up to 120 °C and then (partially) recover upon cooling back to RT. After 5 cycles, the $CsPbBr_3/SiO_x$ composite retains 81% of the initial emission intensity while the PL of bare $CsPbBr_3$ NCs drops to 31%. The stability against water is assessed by dispersing the samples in DI water under stirring and monitoring the resulting PL. As shown in **Figure 2.8b**, after 140 minutes, the $CsPbBr_3/SiO_x$ sample retains 76% of the initial emission intensity, while the PL of bare $CsPbBr_3$ NCs is quenched entirely within a few minutes. These stability results indicate that the SiO_x matrix improves both the thermal and the water stability of the $CsPbBr_3$ NCs.

2.6. Fabrication and characterization of W-LED

The $CsPbX_3/SiO_x$ composite samples are tested as down-conversion phosphors on top of a blue commercial LED. To this aim, green- and red-emitting powders are mixed with PMMA, finely ground, and pressed into a solid pellet (see **Figure 2.9a** for a schematic representation of the process and the *experimental part* for more details). The resulting emission spectrum is displayed in **Figure 2.9b**, where three peaks resulting from the blue LED and the two different phosphors are visible. It is worth noting that green- and red-emitting phosphors maintain their color purity in the pellet, confirming that the different NCs are well separated and no unwanted anion-exchange reactions occur, which would otherwise have led to a single yellow emission.[174] As a result, the CIE coordinates of (0.32; 0.33) (**Figure 2.9c**) are very close to the ideal white coordinates (0.33; 0.33) and correspond to a CCT of 6186 K that is suitable for most lighting and display applications. Also, the CRI is 69. Eventually, the luminance of commercial blue LED with and without the down-converting pellet is measured, finding values of 102 cd/m^2 and 29320 cd/m^2, respectively. Luminance loss can be attributed to various factors, such as non-

unity quantum yield of the phosphors and scattering losses in the relatively thick and rough pellet. Nonetheless, the value of 102 cd/m^2 is in the range of most common PC and smartphone displays.

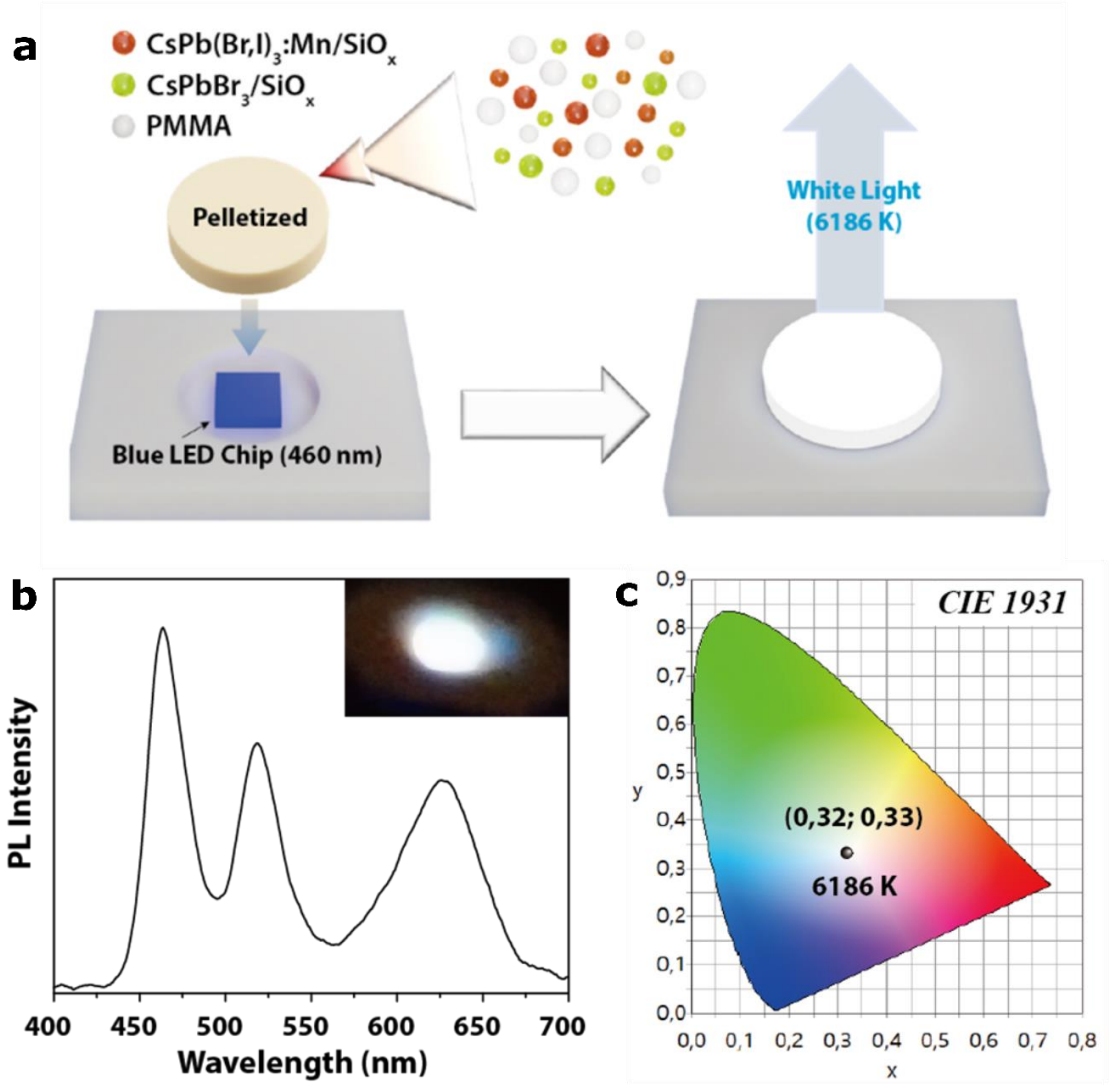

Figure 2.9. (a) Schematic structure of W-LED fabrication. Red $CsPb(I/Br)_3:Mn/SiO_x$ and green $CsPbBr_3/SiO_x$ emitting composite powders are covered on the 460 nm blue LED. **(b)** The emission spectrum of the fabricated W-LED (inset: photograph of the W-LED under working) **(c)** CIE1931 color coordinate diagram.

2.7. Conclusion

In summary, a simple and straightforward procedure to synthesize different color emitting $CsPbX_3/SiO_x$ composites is developed by employing phase transformation from 0D Cs_4PbX_6 NCs into 3D $CsPbX_3$ NCs via the sol-gel route.

It has been shown that the silica layer effectively isolates $CsPbX_3$ NCs from the outer environment, and thus, both water and thermal stability of $CsPbX_3$ NCs are significantly improved. Besides, this silica layer prevents undesirable anion exchange reactions between perovskite NCs. The W-LED is fabricated using green and red powders combined with a blue InGaN LED. The resultant of W-LED represents a color coordinate close to that of the ideal white light and a good color rendering index. Overall, with these results, $CsPbX_3/SiO_x$ composites present high potential as a promising material for the display, lighting, and bio-logical fields with improving future performance.

2.8. Experimental part

Synthesis of 0D Cs_4PbX_6 NCs. The synthesis is performed following the procedure reported in the previous work.[175] Briefly, 0.1 mmol of PbX_2 is combined with 5 mL of ODE, 0.2 mL of OA, and 1.5 mL of OLAM in a 20 mL vial, and the mixture is heated on a hotplate set at 150 °C. After the complete dissolution of the PbX_2 salt, the solution is cooled down to the desired reaction temperature, and 0.75 mL of a 0.3 M Cs-oleate solution in OA (obtained by dissolving 0.4 g of Cs_2CO_3 in 8 mL of OA at 150 °C) is swiftly injected. After about 30 seconds, the mixture becomes turbid white and is quickly cooled down to RT by plunging the vial into a water bath. The NCs are separated by centrifugation (at 4500 rpm for 10 minutes) and redispersed in 3 mL of hexane. Further details are presented in **Table 2.1**.

Table 2.1. Experimental conditions for the preparation of 0D Cs_4PbX_6 NCs

0D NCs	$PbBr_2$ (mmol)	$PbCl_2$ (mmol)	PbI_2 (mmol)	Reaction temperature (°C)
Cs_4PbBr_6	0.1			80
$Cs_4Pb(Cl/Br)_6$	0.05	0.05		100
$Cs_4Pb(I/Br)_6$	0.02		0.08	80

Synthesis of $CsPbX_3/SiO_x$ composites. 1 mL of Cs_4PbX_6 NCs solution [Pb]≈5 mM), 2 mL of hexane, 0.5 mL of TEOS, 20 µL of OA, and 10 µL of a 0.1 M lead oleate solution in OA (prepared by dissolving 22 mg of PbO in 1 mL of OA at 100 °C) are loaded into a 20 mL vial under stirring. The vial is placed

on a hot plate and heated to 100 °C. At this point, 10 µL of an aqueous solution of HNO_3 (65 % w/w) is injected into the vial, and the reaction is allowed to proceed at 100 °C for 30 minutes. Subsequently, the vial is moved onto a stirring plate at RT and is left there for 10 hours, after which a gel is obtained. The vials are kept uncapped during the whole procedure. The gel is washed with 2 mL of hexane, separated by centrifugation (twice), and finally dried at 40 °C for 2 hours in a vacuum oven yielding a flaky product. The flakes are then ground to powders in an agate mortar.

The preparation of Mn-doped $CsPb(I/Br)_3/SiO_x$ samples is similar, but 0.2 mL of TEOS and 3 µL of HNO_3 solution containing 0.1 M $Mn(ac)_2$ are used instead.

Fabrication and characterization of W-LED. Dry powders of red- and green-emitting $CsPbX_3/SiO_x$ composites are finely ground in a mortar together with PMMA beads. The resulting powder mixture is then pressed into a solid pellet of 16 mm in diameter and *ca.* 1-2 mm in height. The as-obtained phosphor pellet is placed on top of a commercial blue LED (Thorlabs LIU470A).

Appendices

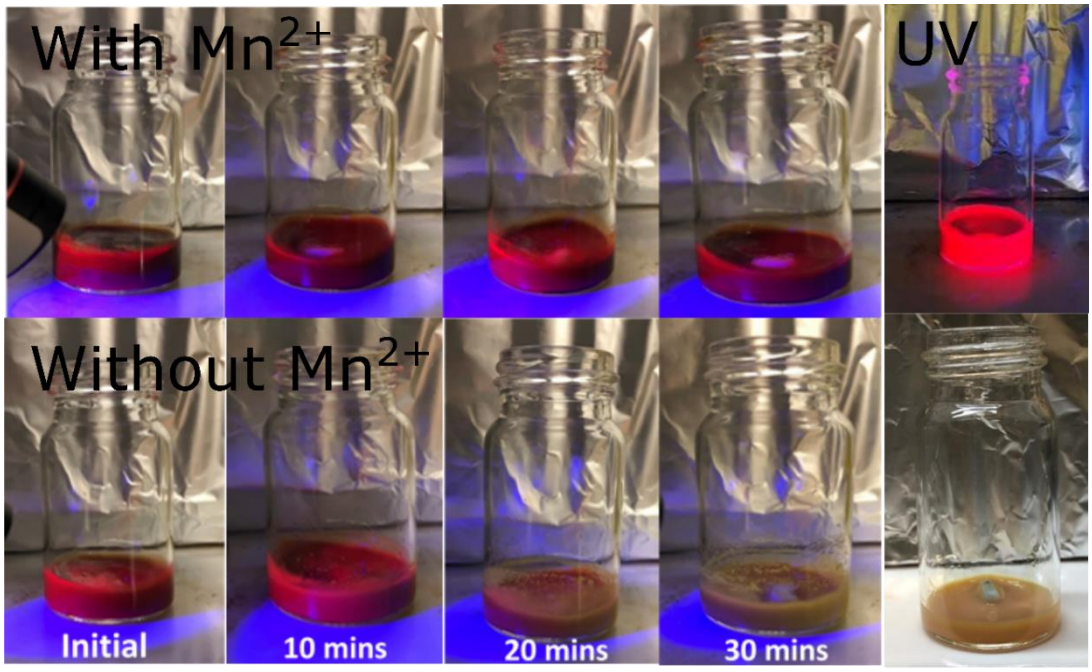

Appendix 2.1. Visualization of Mn-doped/non-doped $CsPb(Br,I)_3/SiO_x$ gelation process. In the absence of Mn^{2+} ions, the mixture solution turns brown and does not exhibit any PL emission.

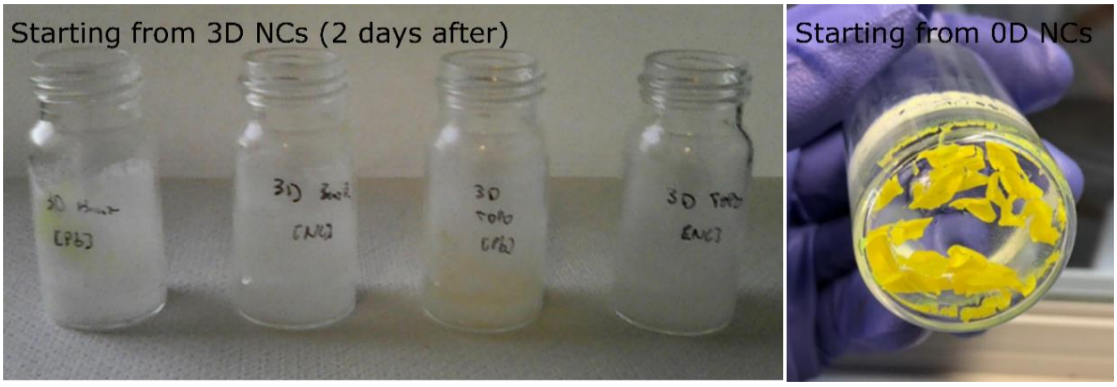

Appendix 2.2. The comparative experiment of the sol-gel process starting from 0D Cs_4PbBr_6 and 3D $CsPbBr_3$ NCs. When starting with 3D $CsPbBr_3$ NCs, only white powders (no emission) are obtained, while starting with 0D Cs_4PbBr_6 NCs, the homogenous green-emitting gel is obtained.

CHAPTER 3

$CsPbBr_3$/m-SiO_2 composites prepared via molten salt synthesis

Abstract: *This chapter presents a new molten salt synthesis route to prepare $CsPbBr_3$/m-SiO_2 composite materials made of mesoporous silica (m-SiO_2) particles whose pores are filled with light-emitting lead halide nanocrystals and other inorganic salts (e.g., KNO_3, $NaNO_3$, and KBr). The molten salts allow for the nucleation of perovskite nanocrystals $CsPbBr_3$ inside silica pores and enable the sealing of those pores at mild temperatures 350 °C, representing an important technological advancement compared to previous works (in which analogous sealing was observed only above 600 °C). The resulting $CsPbBr_3$/m-SiO_2 composites have high PLQY values (around 90 %) and exhibit high stability against heat, water, and even aqua regia. The white light-emitting diode (W-LED) devices in two prototypes, on-chip, and remote configuration, are fabricated from these composites to achieve stable white light emission. Moreover, these $CsPbBr_3$/m-SiO_2 composites also demonstrate their promise as an oil tracer material as they could survive under harsh conditions test of saline water and high temperature, which represents the typical underground oil wells environment.*

Parts of this chapter have been adapted or reproduced with permission from ref.[176] and patent application no. IT 102020000018481.

3.1. Introduction

Solution synthesis methods for nanocrystals fabrication have proven to be successful for various types of nanocrystals, such as metals[177], metal oxides,[178], and various conventional semiconductors.[179] However, in order to synthesize many types of inorganic nanocrystals, high-temperature conditions, usually well above 350 °C, can be required.[180] Unfortunately, this is a limitation for most organic solvents as they are not stable under such high-temperature conditions.

The use of molten salts to synthesize nanostructures has emerged in the last years as an essential complementary route to conventional liquid phase approaches. A molten salt (MS) is salt that is solid under ambient conditions, but that becomes liquid at an elevated temperature. The melting temperature

(i.e., the reaction temperature) and different ions in a MS synthesis can be precisely controlled by carefully selecting the fractions of the various salts in a mixture of salts. The MS method has the advantages of easy operation, fast ion diffusion, and tunable temperature (~ 100 °C to over 1000 °C) for the large-scale synthesis of different inorganic nanomaterials.[181-183]

In the work presented in this chapter, the use of molten salts allows for the formation of $CsPbBr_3$ perovskite NCs embedded inside mesoporous silica (m-SiO_2) matrix. The obtained $CsPbBr_3$/m-SiO_2 composites feature a strong PL emission (PLQY 89 %) and are highly stable against high temperature (180 °C), water, even aqua regia, and saline water. Besides presenting the synthesis approach, characterization, and stability test, this chapter also provides the result of applying $CsPbBr_3$/m-SiO_2 composites as down-converting phosphors white-LED, demonstrating the potential of this material in a display application.

3.2. $CsPbBr_3$/m-SiO_2 composites production

In a typical synthesis of $CsPbBr_3$/m-SiO_2 composites, CsBr and $PbBr_2$ (i.e., the perovskite precursors) are mixed with a molten salts mixture, namely KNO_3:$NaNO_3$:KBr (10:5:5 of molar ratio), and m-SiO_2 particles, and then heated up to 350 °C under the air in a furnace for 60 minutes (**Scheme 3.1**).

Scheme 3.1. Production of $CsPbBr_3$/m-SiO_2 composites via molten salts synthesis.

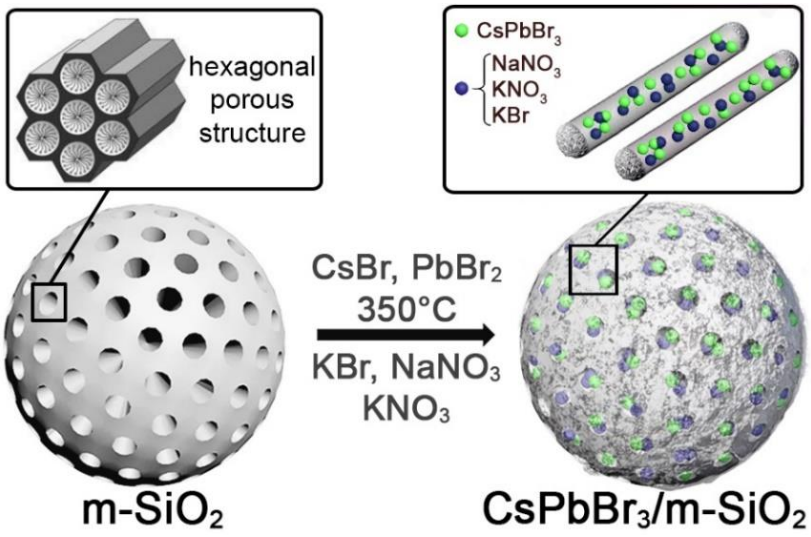

The $CsPbBr_3$/m-SiO_2 composite powder, obtained after washing the product with DMSO, features a bright PL emission peaked at 520 nm with a FWHM of 21.5 nm (99.18 meV) and a PLQY as high as 89 % (**Figure 3.1a**). The XRD pattern can be indexed with the orthorhombic $CsPbBr_3$ (ICSD 98-009-7851) crystal structure with the presence of KBr, $NaNO_3$ KNO_3 phases (**Figure 3.1b**). Given the high solubility of KBr, $NaNO_3$, and KNO_3 salts in polar solvents, their presence in the final composites, as evidenced by XRD analysis, indicates that they are must have been encapsulated in the pores of m-SiO_2 particles together with the $CsPbBr_3$ NCs. A broad peak from 15° to 35° is also present in the XRD pattern and is ascribed to the amorphous SiO_2 matrix (**Appendix 3.1a**). Interestingly, when DI water is used for the washing step, the corresponding XRD pattern is dominated by the PbBrOH reflections, which are superimposed to those of the expected $CsPbBr_3$ material. (**Appendix 3.2c**). The formation of PbBrOH, which is insoluble in water,[184] is attributed to the reaction of Pb-Br compounds present in the reaction medium outside SiO_2 particles. Therefore, to overcome such an issue, another polar solvent, DMSO, which should not lead to the formation of hydroxide compounds (**Appendix 3.2b**), is replaced by DI water in the washing step. It is important to highlight here that the washing with DMSO results in a final product having the same optical properties and PLQY as that obtained by washing with DI water (**Appendix 3.2a**).

An in-depth TEM analysis is performed to reveal the morphology and the structure of $CsPbBr_3$/m-SiO_2 composites. The starting m-SiO_2 MCM-41 particles have a mean size of 0.6 µm, as emerged from the DLS measurements (**Appendix 3.3**), and are characterized by a porous hexagonal structure. These pores have a mean diameter of 3.3 nm (**Appendix 3.1b**). TEM images of the final composite indicate that the nanoparticles had grown inside the pores of SiO_2 with the concomitant collapse of most of the pores (**Figure 3.1c**). High resolution (HR) TEM, high-angle annular dark-field (HAADF) - scanning transmission electron microscopy (STEM), and energy-dispersive X-ray spectroscopy (EDS) analyses are performed to gain a deeper understanding of the nanostructure of the nanostructure of the

composites. As shown in **Figure 3.1e**, the SiO_2 mesoporous structure is partial collapsed. The formation of orthorhombic $CsPbBr_3$ NCs and K, Na, and N-containing salts (with the K:Na ratio being close to 2:1) inside the SiO_2 particles is confirmed by EDS analysis in **Figure 3.1c-d.**

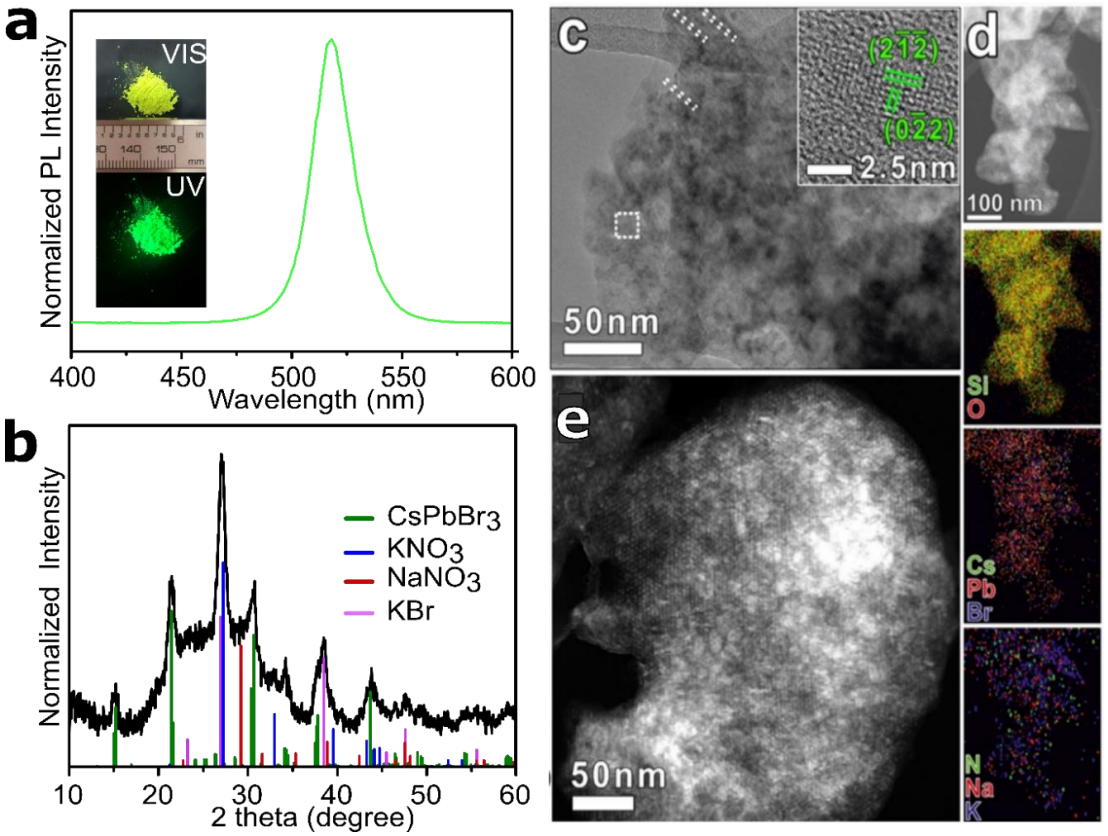

Figure 3.1. Characteristic of $CsPbBr_3$/m-SiO_2 composite: **(a)** PL spectrum (Inset is the photograph of the sample under visible and UV light, 345 nm). **(b)** XRD pattern (References are the bulk reflections of $CsPbBr_3$ (ICSD 98-009-7851), KBr (ICSD 98-005-3826), KNO_3 (ICSD 98-003-6113) and $NaNO_3$ (ICSD 98-001-5333)). **(c)** BF-TEM images. (Inset is HRTEM image of a $CsPbBr_3$ NC embedded in amorphous silica found in the square area highlighted in (c)). **(d)** HAADF-STEM images and the corresponding EDS elemental maps. **(e)** HAADF-STEM image.

3.3. Stability of $CsPbBr_3$/m-SiO_2 composites against thermal, water, and acidic environments

The stability of $CsPbBr_3$/m-SiO_2 composites is assessed by exposing the samples to either high temperature (180 °C), water, or aqua regia. Parallelly, colloidal $CsPbBr_3$ NCs prepared via a standard hot injection approach[185] are also tested for comparison. The samples are annealed at 180 °C in an argon

atmosphere for 3 hours, and the variation of the PLQY is monitored before and after the test. The $CsPbBr_3$/m-SiO_2 composite retains 78 % of the initial PLQY, whereas the PLQY of the colloidal $CsPbBr_3$ NCs drops from 90 % to 30 % after annealing at 180 °C in argon for 2 hours (**Figure 3.2a**). The stability against water is assessed by dispersing and stirring the samples in DI water and monitoring the resulting PLQY over time. Compared with colloidal $CsPbBr_3$ NCs whose PL emission complete quenches after few minutes of immersing in water, the $CsPbBr_3$/m-SiO_2 composites are stable in water with no visible drop in PL emission intensity for 30 days (**Figure 3.2b**). Moreover, the composites are stable when immersed in aqua regia for more than 10 days (**Figure 3.2c** and **Appendix 3.4**). Overall, these stability tests highlight the exceptional stability of the $CsPbBr_3$/m-SiO_2 composites that originates from the sealing of SiO_2 pores which leads to the complete protection of LHP NCs by SiO_2. This result to be compared with previous works, in which $CsPbBr_3$ NCs were grown inside m-SiO_2 without the use of molten salts: the resulting compounds could not even sustain a washing step with water.[115, 186]

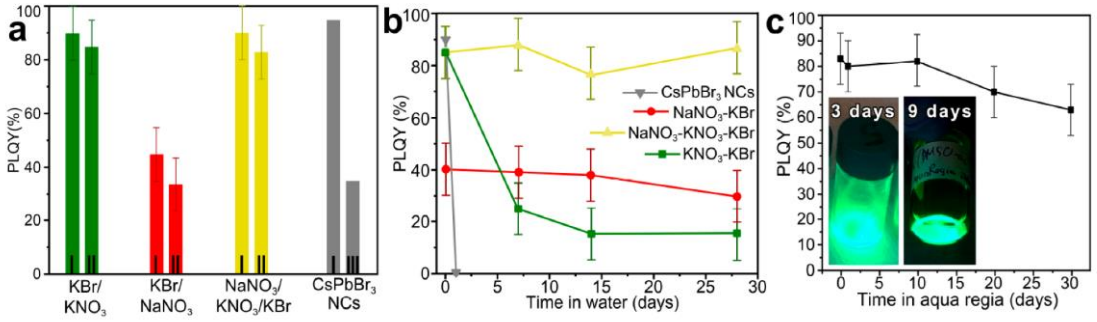

Figure 3.2. (a) PLQY of $CsPbBr_3$/m-SiO_2 composites made by using different molten salts mixtures (KNO_3-KBr (green columns), $NaNO_3$-KBr (red columns), and KNO_3-$NaNO_3$-KBr (yellow columns) and "standard" colloidal $CsPbBr_3$ NCs (grey columns) before (I) and after annealing test at 180 °C in argon for (II) 2h or (III) 3h. **(b)** Time-dependent normalized PL emission of $CsPbBr_3$/m-SiO_2 composites and "standard" colloidal $CsPbBr_3$ NCs immersed in water. **(c)** Time-dependent normalized PL emission of the $CsPbBr_3$/m-SiO_2 composite prepared with KNO_3-$NaNO_3$-KBr molten salts mixture immersed in aqua regia. (Insets: Photographs of $CsPbBr_3$/m-SiO_2 composite immersed in aqua regia for 3 days and 9 days.)

The stability of these samples is comparable to that those prepared by Zhang. et al. who employed a solid-state reaction in which CsBr, $PbBr_2$, and m-SiO_2 were annealed together at high temperatures (> 400 °C).[116] In their case, the

collapse of the mesoporous of silica was observed only when working above 700 °C and, therefore, it was attributed to high reaction temperatures, which also lead to the merging of SiO_2 particles. The resulting heavily sintered/aggregated composites had a reduced PLQY (63 %) that could only be moderately increased to 71 % by an HF treatment. Conversely, the molten salts synthesis does not lead to merging or aggregation of the resulting $CsPbBr_3$/m-SiO_2 particles, as demonstrated by DLS measurements (**Appendix 3.3**). Moreover, the PLQY of this $CsPbBr_3$/m-SiO_2 composite is already very high; hence performing further treatments is unnecessary. In fact, molten salts have even been used to produce mesoporous structures starting from non-porous metal oxides,[187] and, in particular, from silica.[188-192] The corrosiveness of alkali salts to various metal oxides, which have been known for decades,[187, 193] can explain the pore sealing in $CsPbBr_3$/m-SiO_2 composites here.

3.4. Control experiment by various molten salts media

Molten salts play a key role in determining the properties of the final composites. Thus, to better understand the role of molten salts, a series of control experiments are performed, in which the composition of the molten salt is varied systematically. When the composite is made by employing the salts mixture of KBr and KNO_3, the product exhibits a high PLQY (89 %) and a low resistance against water and aqua regia (**Figure 3.2a,b**).[194] This sample consists of m-SiO_2 particles whose pores are filled with $CsPbBr_3$ NCs and KNO_3 (**Figure 3.3a,c**). Interestingly, this procedure does not affect the mesoporous structure of m-SiO_2, which is completely retained (**Figure 3.3a**). Conversely, the use of $NaNO_3$ and KBr yields composites having a low PLQY (42 %) and a high resistance against water and aqua regia treatment (**Figure 3.2a,b** and **Figure 3.4**). The XRD and HRTEM analyses reveal that the product consisted of m-SiO_2 particles filled with $CsPbBr_3$ NCs and NaBr, which has partially lost their mesoporous structure (**Figure 3.3b,d**). These control experiments indicate that the composition of the molten salts mixture has a profound impact on the structure of the final composites.

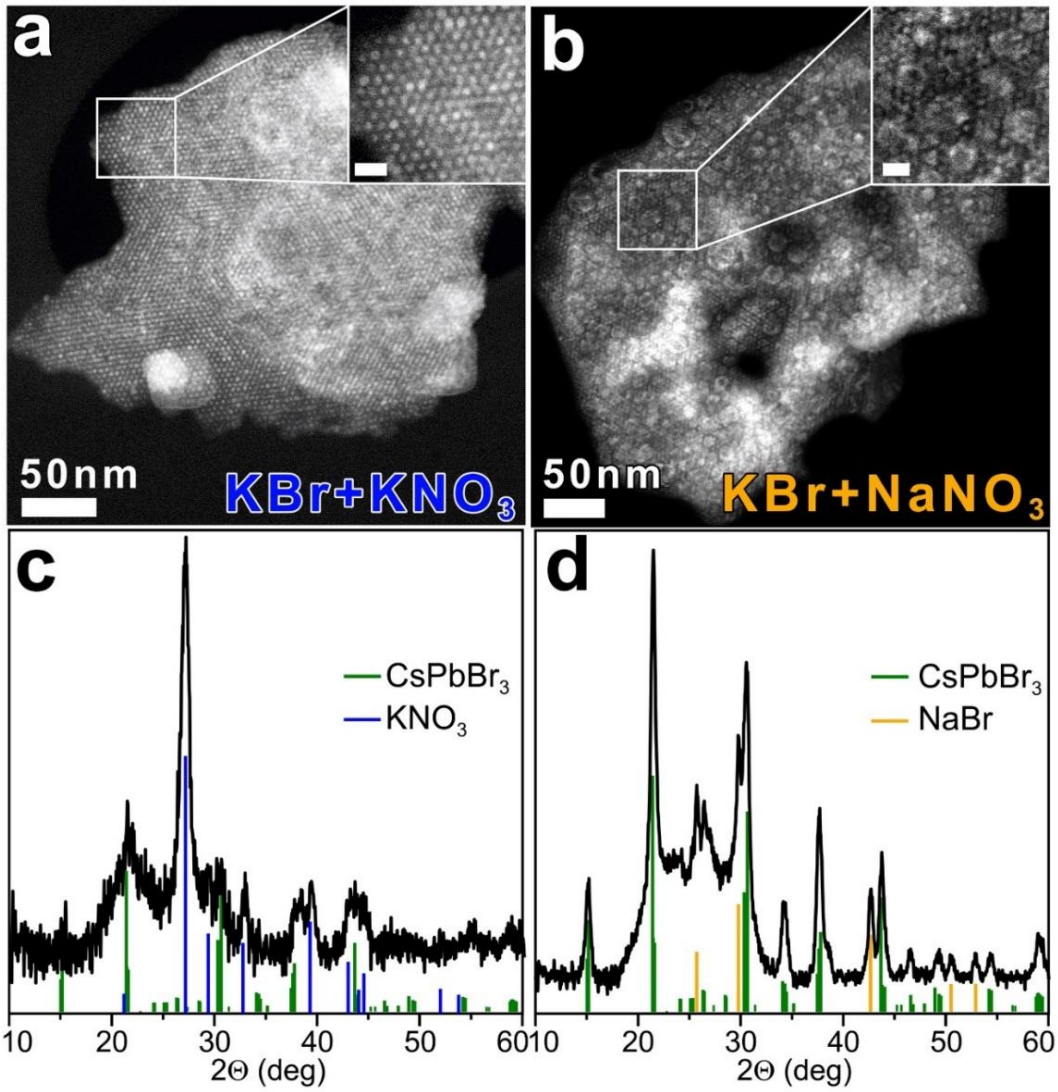

Figure 3.3. STEM-HAADF images and XRD patterns of the composites obtained using diverse molten salts mixture: **(a,c)** $KBr+KNO_3$ or **(b,d)** $KBr+NaNO_3$. The bulk reflections of $CsPbBr_3$ (ICSD 98-009-7851), KNO_3 (ICSD 98-003-6113), and NaBr (ICSD 98-004-1440 are also reported by means of vertical bars.

The ratio of molten salts in the mixture is also important; thus, another series of control experiments are carried out, in which the ternary KNO_3-KBr-$NaNO_3$ molten salts mixture is employed, and then the relative compositions are systematically varied by mixing KNO_3, KBr, and $NaNO_3$ salts in different molar ratio. The resulting emitting composites are stable in aqua regia (means the $CsPbBr_3$ NCs are embedded entirely inside the SiO_2 particles) only observing for the ratio of 10:5:5, 8:7:5, 7:8:5 and 5:10:1 for KNO_3:$NaNO_3$:KBr (**Table 3.1** and **Figure 3.4**), with the best ratio of 10:5:5 giving the maximum the PL emission of the product. Overall, the two control experiment series results indicate that both the composition and the stoichiometry of the molten salt

mixture are of paramount importance in regulating the properties of the final composites.

Table 3.1. The molar ratio of KNO_3:$NaNO_3$:KBr molten salts in different mixtures for $CsPbBr_3$/m-SiO_2 composites synthesis.

Sample	0	1	2	3	4	5	6	7	8	9	10	11	12	13
KNO_3 (mmol)	15	14	13	12	11	10	7.5	9	8	7	6	5	4	0
$NaNO_3$ (mmol)	0	1	2	3	4	5	7.5	6	7	8	9	10	11	15
KBr (mmol)	5	5	5	5	5	5	5	5	5	5	5	5	5	5

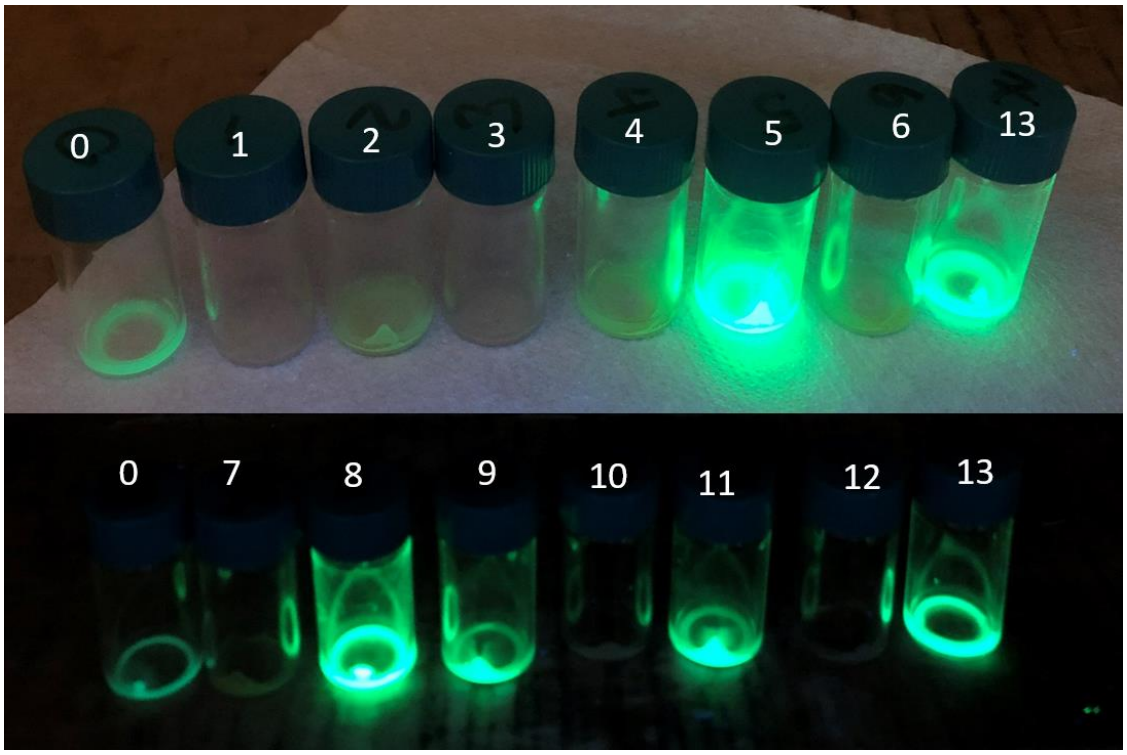

Figure 3.4. Photographs of $CsPbBr_3$/m-SiO_2 composites synthesized by varying the KNO_3:$NaNO_3$:KBr molar ratio (see **Table 3.1**) after being immersed in aqua regia for 3 days. (Photos are taken under UV light illumination (345 nm).

3.5. W-LED application

The $CsPbBr_3$/m-SiO_2 composites are then tested for down-converting W-LED (on-chip and remote configuration). For the fabrication of an on-chip W-LED, a blue-emitting LED (3 Watts, 3.2-3.4 V and wavelength: 445-450 nm) is

covered by a mixture of $CsPbBr_3$/m-SiO_2 composites (green-emitting), $K_2SiF_6:Mn^{4+}$ powder (red emitting), and TiO_2 (light scattering agent) dispersed in poly(dimethylsiloxane). The fabricated device has a white light with CIE color coordinates of (0.2985, 0.3076) and a CCT of 7692 K (**Figure 3.5a-b**).cSuch W-LED promises as a light source in LCD backlighting for wider color gamut displays[195] because it features three distinct narrow emission peaks of blue, green, and red colors (**Figure 3.5a**).

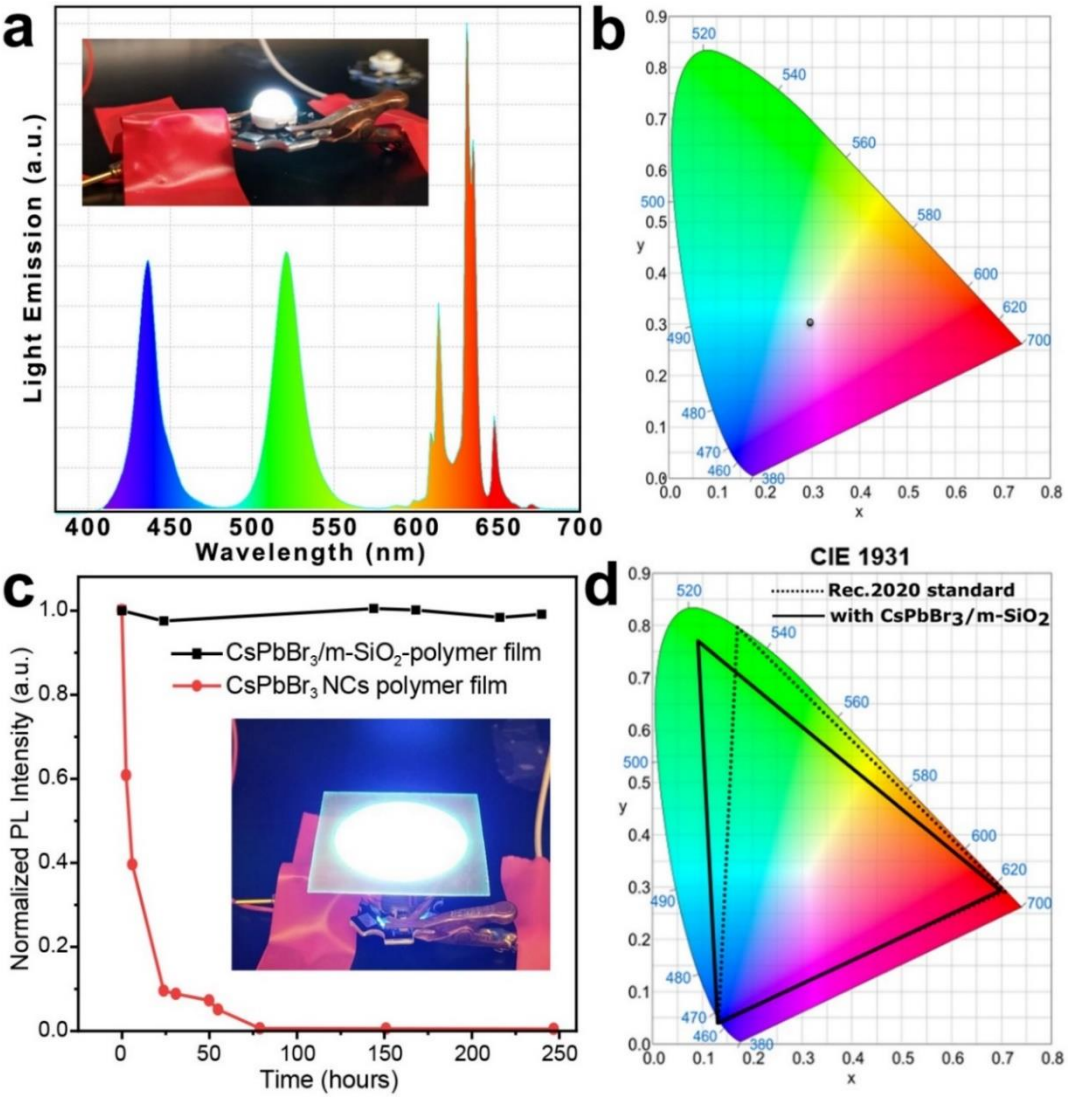

Figure 3.5. (a) The emission spectrum of the fabricated W-LED (Inset: photograph of the W-LED under operation) and the corresponding **(b)** CIE1931 color coordinate diagram. **(c)** Time-dependent normalized PL intensity of ($CsPbBr_3$/m-SiO_2)-polymer film and ($CsPbBr_3$ NCs-polymer) film under high flux remote-configuration test (inset: photograph of the ($CsPbBr_3$/m-SiO_2)-polymer film with blue LED chip (200 mW/cm^2) under operation). **(d)** Color coverage of ($CsPbBr_3$ NCs)-polymer composite film compared to the standard Rec.2020 area.

For the fabrication of a remote-prototype W-LED, a ($CsPbBr_3/m\text{-}SiO_2$)-polymer film is prepared by mixing $CsPbBr_3/m\text{-}SiO_2$, $K_2SiF_6:Mn^{4+}$, and TiO_2 powders enclosed in a UV-curable acrylate polymer and sandwiched in between two transparent barrier polymer films. This film is then placed remotely from a blue LED chip (450 nm, 200 mW/cm^2) (**Figure 3.5c**). Compared to a standard ($CsPbBr_3$ NCs)-polymer composite film, the ($CsPbBr_3/m\text{-}SiO_2$)-polymer film shows superior stability with fully retaining the initial luminescence after a prolonged test of 240 hours under high irradiation flux (**Figure 3.5c**). Moreover, unlike ($CsPbBr_3$ NCs)-polymer film whose the edge with the degradation of the NCs under ambient conditions, the ($CsPbBr_3/m\text{-}SiO_2$)-polymer film exhibits high stability as shown by the absence of edge ingress (**Appendix 3.5**). The ($CsPbBr_3/m\text{-}SiO_2$)-polymer film obtained here gives a color point at x=0.08992; y=0.76927 according to CIE 1931 color diagram and. Using this $CsPbBr_3/m\text{-}SiO_2$ as a green color emitter could cover 87 % of the Rec.2020 area (**Figure 3.5d**). These features make the $CsPbBr_3/m\text{-}SiO_2$ composites particularly promising for down-converter films in lighting and LCD applications.

3.6. Salinity stability of $CsPbBr_3/m\text{-}SiO_2$ composite

In the oil industry, the tracers are employed to probe the efficiency of injection wells drilled for oil extraction. Tracers are inserted into the injection well, and their recovered amount, which is probed at the extraction well, can give precious information about the efficiency of the injection well.[123] Such tracers have to withstand the underground condition with the salinity environment and high temperature.[196, 197] Motivated by high stability against water and aqua regia, the $CsPbBr_3/m\text{-}SiO_2$ composites are also tested under such harsh conditions. After 24 h of incubation in an aqueous solution of NaCl, $CaCl_2$, $MgCl_2$, Na_2SO_4, and $NaHCO_3$ at RT, the PLQY of $CsPbBr_3/m\text{-}SiO_2$ composites is 83 % and decreases to 18 % after continuously incubation at 90 °C for 168 h (**Figure 3.6** and **Appendix 3.6**). The decreasing of PLQY is attributed to the aggregation of the $CsPbBr_3/m\text{-}SiO_2$ particles whose hydrodynamic radius is measured to be 10 µm after the test completion (**Appendix 3.6**). These

preliminary results indicate that these composites are potential candidates for oil tagging applications. However, further improvements are needed to limit their aggregation; for example, surface functionalization of the composite with suitable molecules could be a proper suggestion.

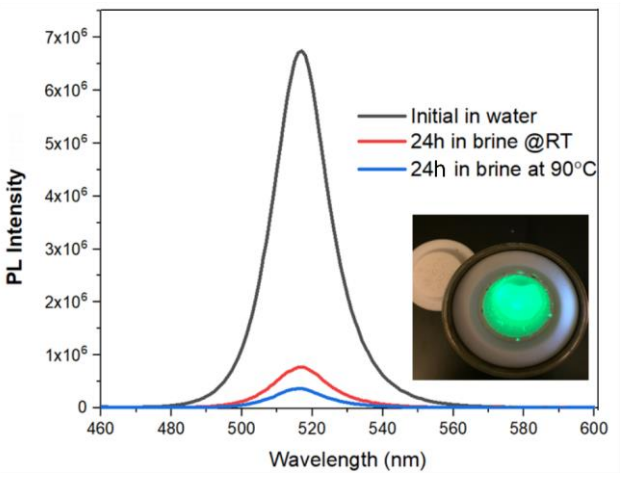

Figure 3.6. PL intensity of $CsPbBr_3$/m-SiO_2 composite before (initial in water, black curve) and after saline test in brine at RT for 24 h in brine (red curve) and at 90 °C for 24 h (blue curve). The PL intensity decrease due to the aggregation of composite during the test, but emission is still observed after the test as shown in the inset photograph.

3.7. Conclusion

A molten salt synthesis route has been developed to produce the composites made of $CsPbBr_3$ NCs embedded, together with inorganic salts (KNO_3-$NaNO_3$-KBr), inside mesoporous SiO_2 particles. The $CsPbBr_3$/m-SiO_2 composites with high PLQY (~90 %) are resistant to heat, water, and even to aqua regia, thanks to molten salts for sealing the pores of SiO_2. These composites are found to be promising as green-emitting phosphors in W-LEDs due to their optical and physical properties: the resulting device emits white light with CIE color coordinates of (0.2985, 0.3076) and CCT of 7692 K and exhibits a highly stable PL emission after 240 hours of operation (in terms of peak position and intensity). In addition, $CsPbBr_3$/m-SiO_2 composites survive after being exposed to salinity environment at 90 °C for 7 days, making them suitable candidates as tracers in the oil industry.

3.8. Experimental Part

Synthesis of $CsPbBr_3$/m-SiO_2 composites. CsBr (1 mmol), $PbBr_2$ (1 mmol), molten salts (different salts mixture are used: KBr:KNO_3 in 5:15 mmol ratio;

KBr:$NaNO_3$ in a 5:15 mmol ratio or KNO_3:$NaNO_3$:KBr in 10:5:5 mmol ratios) and commercial MCM-41 m-SiO_2 (5 mmol) are mixed by grinding with a mortar and pestle. The mixture powder is transferred into a ceramic crucible and heated up to 350 °C in a furnace for 60 minutes under the air, then allowed naturally cooling down to RT. The resulting product is washed with a polar solvent such as DMSO or DMF or even with DI water to remove all the inorganic salts and $CsPbBr_3$ crystals that grown outside of the m-SiO_2 particles. The final powder is eventually dried in a vacuum oven at 40 °C.

LED on-chip prototype. A mixture of $CsPbBr_3$/m-SiO_2 composite (green-emitting), $K_2SiF_6:Mn^{4+}$ powder (red-emitting), TiO_2 (light scattering agent) and PDMS-poly(dimethylsiloxane) is mixed with the wt% ratio of 1:4 for $CsPbBr_3$/m-SiO_2 composite and $K_2SiF_6:Mn^{4+}$. The mixture is then deposited onto a blue LED chip (3 watts, 3.2-3.4 V, and wavelength of 445-450 nm) and heated in the oven at 60 °C for 30 minutes.

$CsPbBr_3$/m-SiO_2-polymer composite film. For the fabrication of a ($CsPbBr_3$/m-SiO_2-polymer) film, a mixture of $CsPbBr_3$/m-SiO_2 composite powder (green-emitting), $K_2SiF_6:Mn^{4+}$ powder (red emitting), TiO_2 (light scattering agent), and a UV- curable polymer (isobornyl acrylate-based) is prepared with the wt% ratio of 1:4 for $CsPbBr_3$/m-SiO_2 and $K_2SiF_6:Mn^{4+}$. The mixture is deposited between transparent barrier films using blade coating and cured under a high flux UV lamp for 30 seconds.

Stability tests for oil tracing applications. In this study, the $CsPbBr_3$/m-SiO_2 composites are tested in 3 different conditions: water at RT for 24 h, brine solution at RT for 24h, and brine solution at 90 °C for 24 h. The composites are dispersed in water or brine solution with a concentration of 1 mg/mL. The brine solution is prepared by dissolving a mixture of 20.396 g of $MgCl_2$, 150.446 g of NaCl, 0.518 g of Na_2SO_4, 69.841 g of $CaCl_2$, and 0.487 g $NaHCO_3$ in 1 liter of distilled water. The PL intensity and size of the composites are compared before and after each test.

Appendices

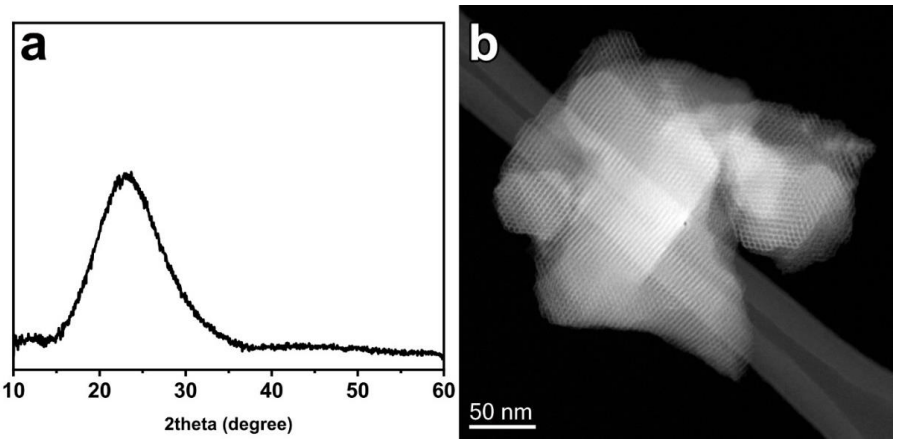

Appendix 3.1. (a) XRD pattern of starting m-SiO_2 MCM-41 (code 643645 Sigma Aldrich) showing a broad peak ranging from 15° to 35° is ascribed to the amorphous SiO_2 matrix. **(b)** HAADF-STEM image of the starting m-SiO_2 MCM-41.

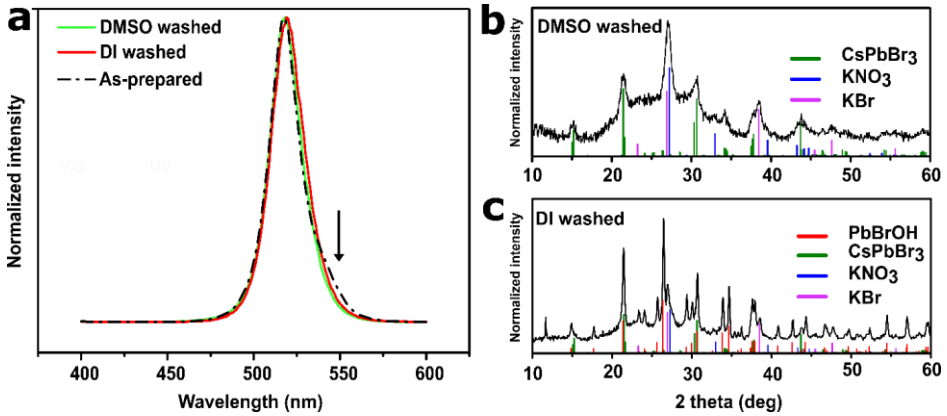

Appendix 3.2. (a) PL spectra of $CsPbBr_3/m\text{-}SiO_2$ composites before (black curve) and after different washing steps: cleaning with the use of DI water (red curve); DI water followed by DMSO (green curve). An arrow indicates the PL emission corresponding to bulk $CsPbBr_3$. **(b, c)** XRD pattern of $CsPbBr_3/m\text{-}SiO_2$ composites obtained after the washing step with water (c) and after a subsequent washing step with DMSO (b). The bulk reflections of PbBrOH (ICSD 98-002-83-13), $CsPbBr_3$ orthorhombic (ICSD 98-009-7851), KBr cubic (ICSD 98-005-3826), and KNO_3 hexagonal (ICSD 98-003-6113) are reported by means of vertical bars.

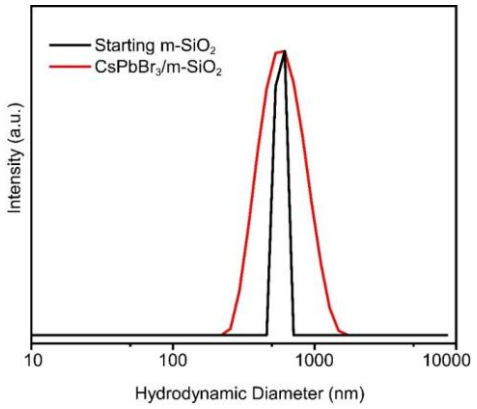

Appendix 3.3. DLS curves are obtained for starting m-SiO_2 particles and $CsPbBr_3/m\text{-}SiO_2$ composites dispersed in water.

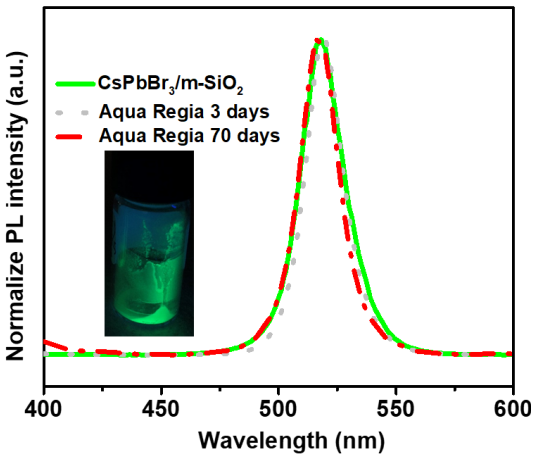

Appendix 3.4. PL spectra of $CsPbBr_3$/m-SiO_2 composite before and after immersion in aqua regia for 3 days or 70 days. The PL peaks position does not change during this test. (Inset: Photograph of $CsPbBr_3$/m-SiO_2 composite immersing in aqua regia for 70 days under UV light, 345 nm).

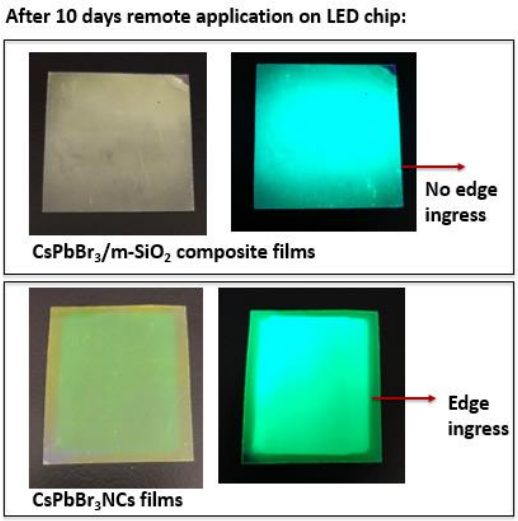

Appendix 3.5. Photographs are taken under visible (left) and UV light (right) of (upper panel) a ($CsPbBr_3$/m-SiO_2)-polymer film which does not show any edge ingress after being tested for 10 days in remote configuration; (lower panel) a $CsPbBr_3$ NCs-polymer film (the $CsPbBr_3$ NCs are synthesized by following the standard colloidal method of Protesescu et al.[26]) tested for 10 days in the remote configuration in which observing the appearance of the edge ingress.

Appendix 3.6. PLQY and size distribution of $CsPbBr_3$/m-SiO_2 composites before (in water) and after the "saline test" in 2 conditions: brine 24 h at RT and brine 24 h at RT, followed by heat 90 °C for 24 h. The photos show the aggregation of the sample overtime during the test.

	In water	In brine 24h	In brine 24h followed by heat 90 oC in brine 24h
PLQY	89 %	74 %	18 %
Particles size (by DLS measurement)	~ 0.6 µm	~ 1.1 µm	> 10 µm
Photo			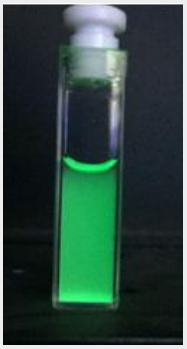

CHAPTER 4

Tin halide perovskites

Abstract: Lead halide perovskite nanocrystals emerged as potential materials for optoelectronic applications due to their outstanding optical properties. Their stability can be remarkably enhanced by several strategies; including two new methods are shown in *chapter 2* and *chapter 3*. However, they are based on Pb, a toxic element, which raises a critical concern for future commercial development. To address such toxicity issue, intense recent research has been devoted to developing lead-free materials. This chapter will present the structure and optical properties of tin (Sn) - based halide perovskites, including Cs_2SnI_6 3D perovskite, and $(C_{18}H_{35}NH_3)_2SnI_4$ 2D perovskite that are synthesized via the hot injection method with some substantial modification.

4.1. Introduction

The hot injection method is the common method to synthesize nanocrystals is discussed in *chapter 1*. In *section 4.2*, the Cs_2SnI_6 crystals are synthesized via a "benzoyl halide" hot injection method[198] based on the use of benzoyl halide (i.e., benzoyl iodide) as a halide source to be injected into the hot solution. The detailed results about the structure, size, shape and optical properties of these Cs_2SnI_6 crystals will be presented in this chapter. In *section 4.3*, a Sn-based 2D Ruddlesden–Popper-type $(C_{18}H_{35}NH_3)_2SnI_4$ perovskite is also synthesized by a similar method. The material is composed of a micro-platelets that exhibit large Stokes-shifted (250 nm) PL emission at 630 nm (red color emission), which is assumed to originate from self-trapped excitons.

4.2. Synthesis and characterization of 3D perovskite Cs_2SnI_6

Cs_2SnI_6 crystals are prepared via a hot injection process, previously employed by Muhammad et al.[198] for the synthesis of $APbX_3$ NCs, which relies on the use of benzoyl iodide as the halide precursor.

In a typical synthesis, cesium carbonate and tin (IV) acetate are dissolved and degassed in oleylamine, oleic acid, and octadecene at 120 °C in a three-neck flask. Subsequently, the solution is heated up to 180 °C, and the benzoyl iodide precursor is swiftly injected into the reaction flask leading to trigger the immediate nucleation and growth of the NCs (see *experimental part*). The resulting crystals have a black color and are ~100 nm in size (see TEM images in **Figure 4.1**). The XRD pattern of the sample is characterized by the presence of peaks at 2θ = 26.49°, 30.69°, 43.95°, 50.06°, 54.56°, which correspond to the diffractions from the (222), (004), (044), (226), and (444) planes of the cubic Cs_2SnI_6 structure (ICSD 98-002-2105)[126, 132, 199] (**Figure 4.2a**).

Control experiment revealed that the optimal temperature for the nucleation and growth of Cs_2SnI_6 crystals is ~180 ° C, which results in the crystals having an XRD pattern matching to the cubic Cs_2SnI_6 structure without the formation of secondary phases (see **Figure 4.2a**). On the other hand, at lower temperatures (i.e., 150 ° C), the samples obtained contain a mixture of Cs_2SnI_6 and CsI phases (see **Appendix 4.1**).

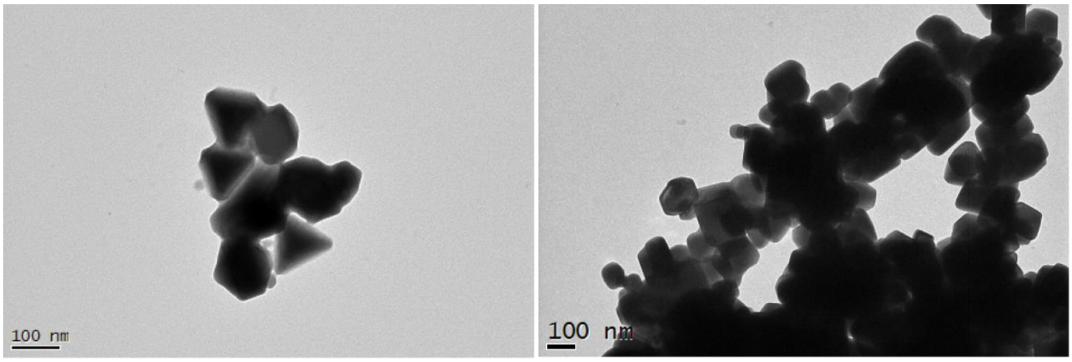

Figure 4.1. TEM images of Cs_2SnI_6 crystals.

The Cs_2SnI_6 crystals are then characterized by an absorption peak at 680 nm and an absorption onset near 1100 nm. Also, the bandgap of Cs_2SnI_6 crystals is calculated by extrapolating the linear of the plot $(\alpha h\nu)^2$ versus $h\nu$ based on the Tauc plots:

$$\alpha h\nu \propto \left(h\nu - E_g\right)^n$$

where α, h, ν are the optical absorption coefficient, Plank Constant, photon frequency, respectively; Eg is the bandgap of the sample; and n is constant whose value depends on whether the semiconductor is direct (n = 2) or indirect (n = 1/2).

The bandgap of Cs_2SnI_6 crystals is found to be 1.55 eV assuming a direct bandgap, which is in line with reported values which range from 1.3 eV (in the case of bulk crystals[126, 199]) to 1.68 eV (in the case of quantum dots (1-3 nm)[156]).

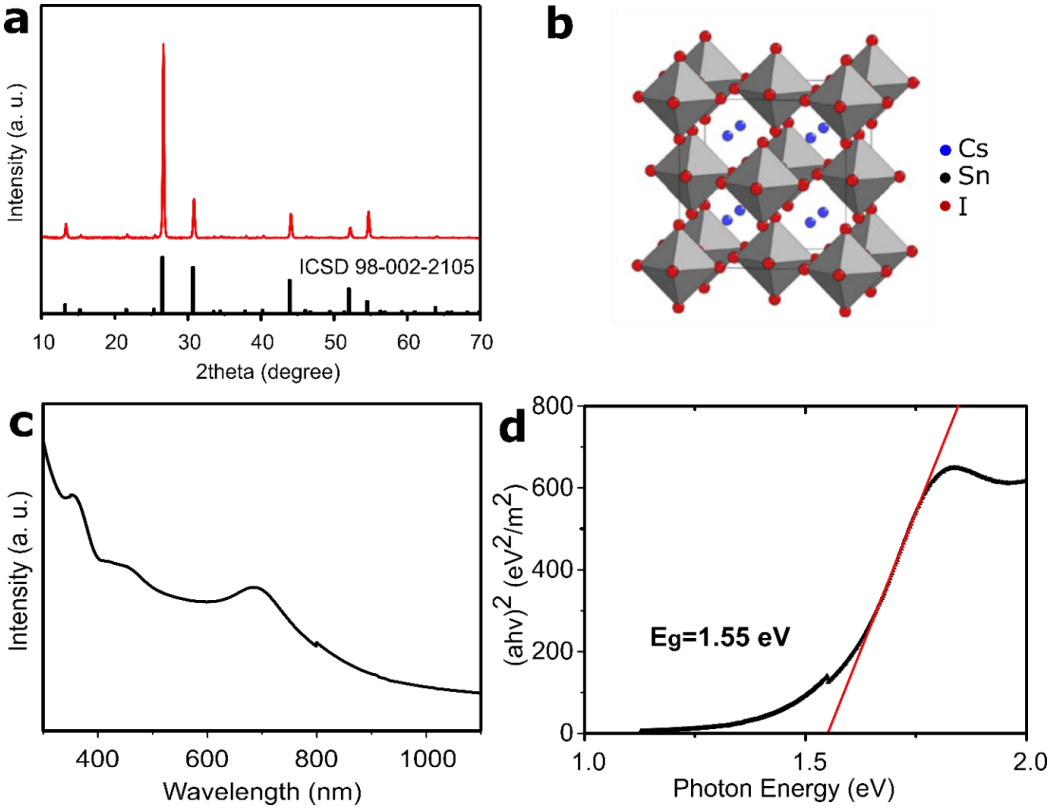

Figure 4.2. (a) XRD pattern of the Cs_2SnI_6 crystals together with the bulk reflections of Cs_2SnI_6 (ICSD 98-002-2105), **(b)** crystal structure of Cs_2SnI_6, **(c)** absorption spectra of Cs_2SnI_6 crystals, **(d)** Tauc fit of the absorbance data assuming a direct bandgap for Cs_2SnI_6 crystals, yielding a 1.55 eV gap.

The emission of Cs_2SnI_6 is not observed in the bulk form, whereas different results are reported in nanoscale. For example, Wang et al. first reported a red emission at 620 nm (2.0 eV), which is observed for Cs_2SnI_6 nanobelts with an average width of 30 nm, a thickness of 6-8 nm, and a length of several micrometers.[131] Later, Ghosh et al. prepared Cs_2SnI_6 nanocrystals in different sizes and shapes (5 nm quantum dots, 30 ± 3 nm nanocubes, nanorods with a length of 500–600 nm and an average radius of 5 ± 1 nm, 100 nm nanosheets), all exhibiting no PL emission.[156] They show that the bandgap of the Cs_2SnI_6 varied from 1.36 to 1.67 eV depending on the particle size. The Cs_2SnI_6 crystals presented in this chapter have no emission.

4.3. Synthesis and characterization of 2D perovskite $(C_{18}H_{35}NH_3)_2SnI_4$

$(C_{18}H_{35}NH_3)_2SnI_4$ NCs, namely, $(OAm)_2SnI_4$ 2D perovskite, are synthesized by the hot injection method with some modification (see the *experimental part* for detail). The TEM images in **Figure 4.3a-b** illustrate that the $(OAm)_2SnI_4$ micro-plates have large lateral dimensions and tend to stack over vertically. The EDS analysis indicates a Sn:I elemental ratio of 19.1:80.9 (**Figure 4.3d**). XRD pattern of the sample also reveals a periodic diffraction pattern at low angles with a regular interval of 2.3° due to the periodic 2D structure of the $(OAm)_2SnI_4$ perovskite, similar to the Pb-based 2D perovskites and reported $(OAm)_2SnBr_4$.[200, 201]

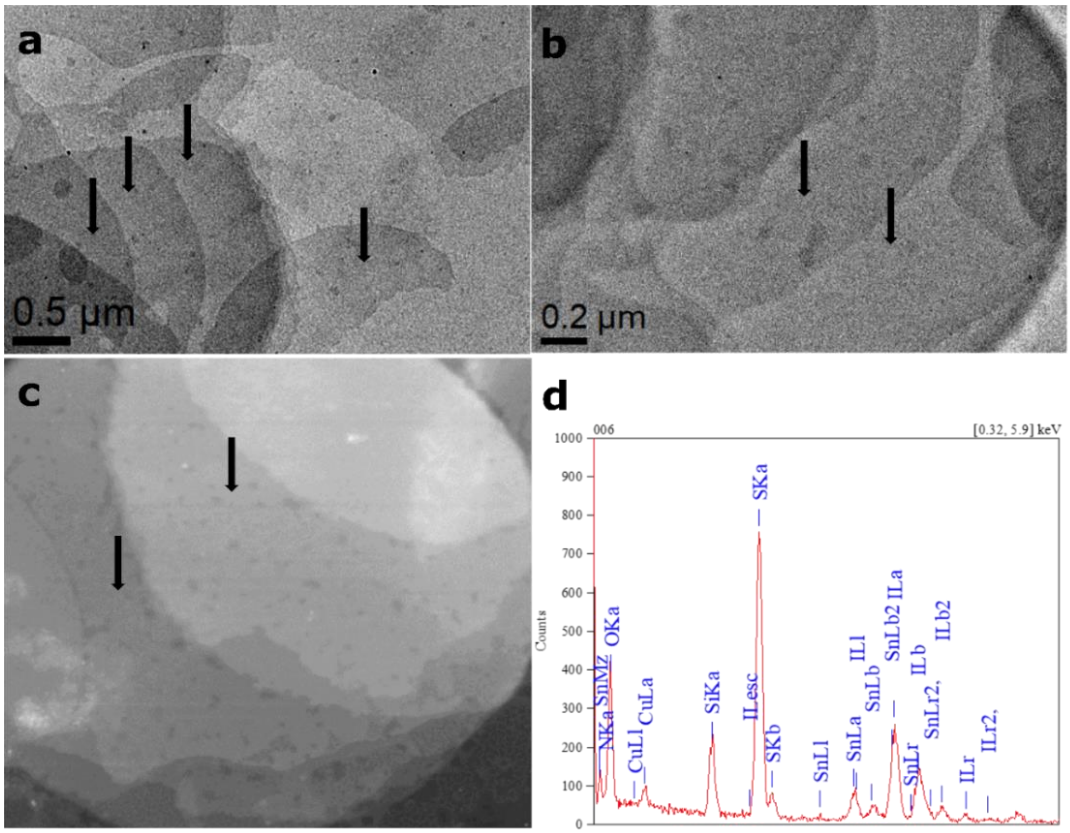

Figure 4.3. (a-b) TEM images of $(OAm)_2SnI_4$ 2D perovskite, **(c)** HAADF-STEM image of $(OAm)_2SnI_4$ 2D perovskite (the arrows indicate different layers of material), **(d)** the corresponding EDS elemental ratio of (c) estimates the atomic concentration percentage of Sn:I was 19.1:80.9.

$(OAm)_2SnI_4$ 2D perovskite follows the general formula of Ruddlesden–Popper-type 2D perovskite, $A'_2A_{n-1}B_nX_{3n+1}$, where A' cation represents OAm^+ ($C_{18}H_{35}NH_3^+$), B represents Sn, X represents I, and n = 1. The structure of the $(OAm)_2SnI_4$ 2D perovskite is shown in **Figure 4.4b**. Interlayer spacing d between the centers of mass of the $(SnI_6)^{4-}$ octahedron layers has been determined to be 3.9 nm, calculated considering the regular intervals between the diffraction peaks at small angles. Both the size of the $(SnI_6)^{4-}$ octahedra and the chain length of OAm contribute to this spacing. The NH_3^+ heads from OAm^+ electrostatically interact with I^- ions in the $(SnI_6)^{4-}$ octahedra, and the long carbon chains interdigitate between the inorganic layers formed by $(SnI_6)^{4-}$ octahedra through van der Waals interactions in an overlapping tail–tail arrangement.[202] The relationship between the layer spacing d and the carbon chain length in OAm is given by an equation d (nm) = 0.85 + 0.16 × m, where m stands for the number of carbons in the alkyl chain, according to a previous study on $(C_nH_{2n+1}NH_3)_2PbBr_4$ 2D perovskites.[203] For the $(OAm)_2SnI_4$ 2D perovskite, where m = 18, the value of d is calculated to be 3.7 nm, which is in good agreement with the above-mentioned experimental value.

Figure 4.4c shows the absorption spectrum, PLE curve, and broad red PL emission located at 630 nm under excitation at 370 nm of the $(OAm)_2SnI_4$ 2D perovskite. This material has a redshift in PL emission compares to the reported $(OAm)_2SnBr_4$ 2D perovskite, which exhibits a PL peak at 620 nm with orange emission. This redshift can be explained by the substitution of Br^- with I^- anions in $(OAm)_2SnI_4$ 2D perovskite here. Similar to $(OAm)_2SnBr_4$, the $(OAm)_2SnI_4$ material also has a large Stokes shift (250 nm). Generally, such large Stokes shifts and broad emissions do not originate from direct band-related recombination of carriers.[204-206] Thus, the emission in $(OAm)_2SnI_4$ 2D perovskite materials can be explained by taking into account self-trapped excitons, as already reported in previous works dealing with 0D, 1D, corrugated 2D metal halide perovskites, and $SnBr_2$ crystals.[41, 161, 207, 208]

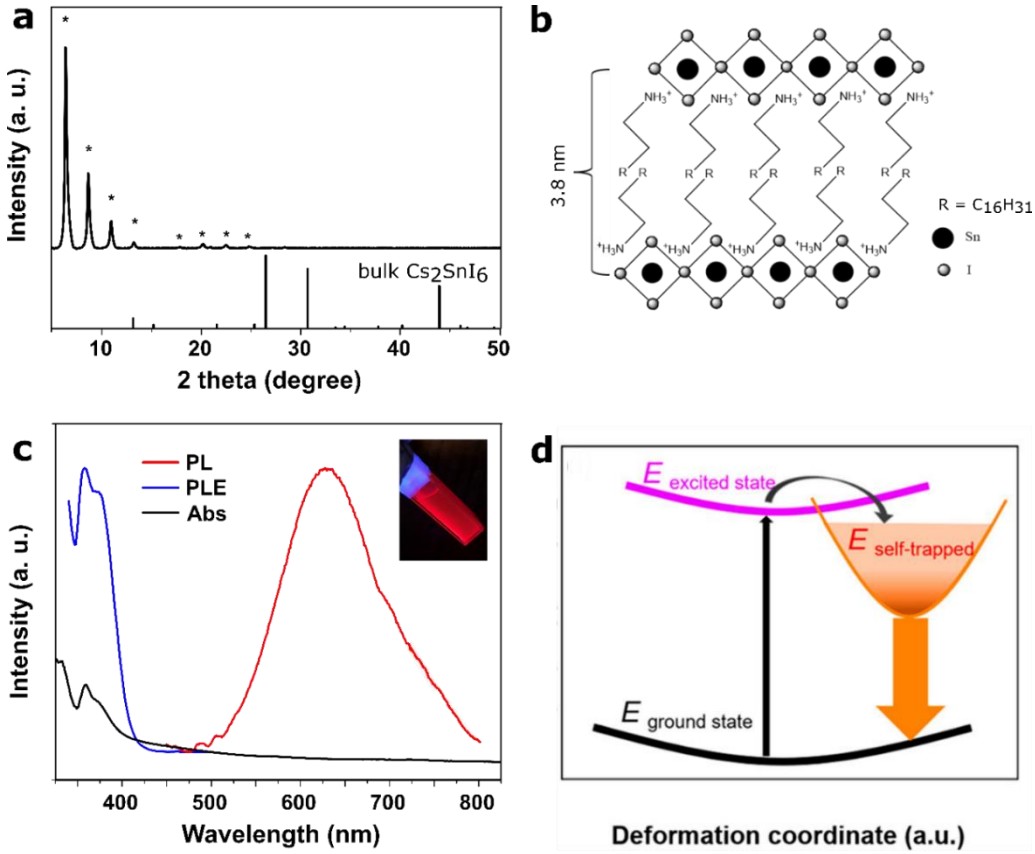

Figure 4.4. (a) XRD pattern of $(OAm)_2SnI_4$ 2D perovskite together with the bulk reflections of Cs_2SnI_6 (ICSD 98-002-2105), **(b)** proposed crystal structure of $(OAm)_2SnI_4$ 2D perovskite, **(c)** absorption (black curve), PLE (blue curve), and PL (red curve) spectra of $(OAm)_2SnI_4$ 2D perovskite (an inset is the photograph of the sample under UV light), **(d)** Configuration coordinate diagram for the potential energy curves to illustrate the photo-physical processes resulting in emission from the exciton self-trapping state at room temperature.

In classic solid-state theory, a configuration coordinate diagram (**Figure 4.4d**) is commonly used to illustrate the photo-physical processes resulting in emission from the exciton self-trapping state.[209] Under high-energy photon excitation, electrons are excited to a manifold of excited states from the ground state and then fall into lower energy self-trapped states through ultrafast excited-state structural reorganization. The subsequent recombination between electrons and holes generates large Stokes shifts and broad-band emissions.[206, 210, 211]

To explore the influence of different A'- site cations on the structure and optical properties of 2D perovskites, various amines with shorter alkyl chains ($C_8H_{17}NH_2$ - octylamine and $C_6H_{13}NH_2$ - hexylamine) are employed in the synthesis of

$(C_8H_{17}NH_3)_2SnI_4$ and $(C_6H_{13}NH_3)_2SnI_4$ 2D perovskites, respectively. XRD patterns of the samples reveal the expected periodic diffraction patterns with the interlayer space d = 2.3 nm and 1.9 nm for $(C_8H_{17}NH_3)_2SnI_4$ and $(C_6H_{13}NH_3)_2SnI_4$ 2D perovskites, respectively, attributed to a specified structure of 2D materials (**Appendix 4.2**). The PL spectra of these materials indicated the broad orange emissions and the PL peaks at around 625 nm (**Appendix 4.3**).

4.4. Conclusion

This chapter provides the results on the synthesis and characterization of the structure and optical property of Cs_2SnI_6 3D perovskite and $(OAm)_2SnI_4$ 2D perovskite materials. The Cs_2SnI_6 crystals have a size of 100 nm, a broad absorption band at 680 nm, and no emission, whereas $(OAm)_2SnI_4$ 2D perovskite with layer structure is characterized by a broad emission at 630 nm, which is ascribed to the intrinsic self-trapped states of molecular $(SnI_6)^{4-}$ species. These preliminary results of Cs_2SnI_6 crystals and $(OAm)_2SnI_4$ 2D perovskite relatively contribute to the library of the structure-property of the Sn-based perovskites family. More extensive studies are required to optimize these materials in the future, such as controlling their size and optical properties.

4.5. Experimental part

Preparation of Benzoyl Iodide. 3 g of sodium iodide is mixed with 1.4 mL of benzoyl chloride in a 20 mL vial. The mixture is vigorously stirred at 75 °C on a hot plate for 5 h. The reaction mixture turns from colorless to an orange-red color, indicating that the transformation of the benzoyl chloride into the benzoyl iodide is successful. Then, the mixture is cooled down to RT and diluted using 3 mL of anhydrous ODE.

Synthesis of Cs_2SnI_6 3D perovskite NCs. 16 mg of Cesium carbonate, 71 mg of tin (IV) acetate, 1 mL of OLAM, 0.5 mL of OA, and 5 mL of ODE are loaded into a 25 mL 3-neck round bottom under vacuum for 1 h at 120 °C. Subsequently,

the temperature is increased to 180 °C under N_2, and the 1.2 mmol of the benzoyl iodide precursor is swiftly injected into the solution. The reaction mixture is kept for 20 s before injecting 5ml fresh toluene for quenching reaction. Then, the resulting mixture is centrifuged for 10 min at 4000 rpm. The supernatant is discarded, and the precipitate is re-dispersed in 5 mL of toluene for further use.

Synthesis of A_2SnI_4 2D perovskites (A = $C_{18}H_{35}NH_3$, $C_8H_{17}NH_3$, and $C_6H_{13}NH_3$). 71 mg of tin (IV) acetate, 0.5 mL of OA, 0.5 mL of oleylamine (or octylamine or hexylamine), and 5 mL of ODE are loaded into a 25 mL 3-neck round bottom flask under vacuum at 120 °C for 1 h. After that, the temperature is increased to desired temperature (180 - 220 °C) (See **Table 4.1** for details) under N_2, and 1.2 mmol of iodotrimethylsilane precursor is swiftly injected into the solution. The reaction mixture is kept for 20 s before injecting 5ml fresh toluene for quenching reaction. Then, the resulting mixture is centrifuged for 10 min at 4000 rpm. The supernatant is discarded, and the precipitate is re-dispersed in 5 mL of toluene for further use.

Table 4.1. Temperature reaction synthesis for different samples

Sample	Reaction temperature
$(C_{18}H_{35}NH_3)_2SnI_4$	220 °C
$(C_8H_{17}NH_3)_2SnI_4$	120 °C
$(C_6H_{13}NH_3)_2SnI_4$	120 °C

Appendices

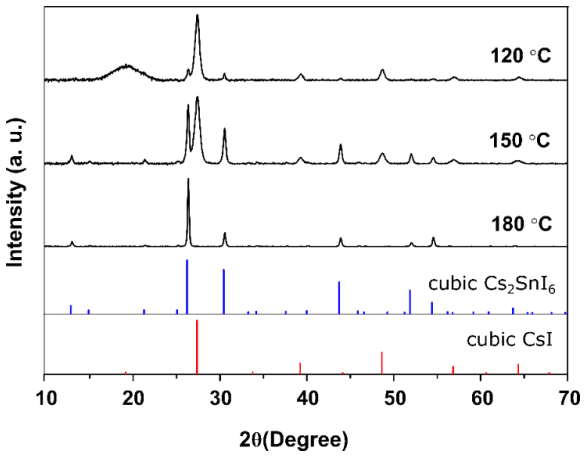

Appendix 4.1. XRD patterns of the samples were prepared at different temperatures: 120 °C, 150 °C, 180 °C with the bulk reflections of cubic Cs_2SnI_6 (ICSD 98-002-2105) and cubic CsI (ICSD code 61517).

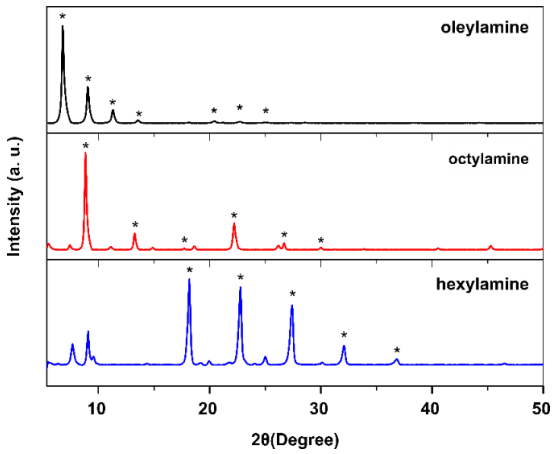

Appendix 4.2. XRD patterns of the $(OAm)_2SnI_4$, $(C_8H_{17}NH_3)_2SnI_4$, and $(C_6H_{13}NH_3)_2SnI_4$ 2D perovskites which are prepared by oleylamine, octylamine, and hexylamine, respectively. The asterisks indicate periodic diffractions, which are specific in 2D perovskites structures. The interlayer spacing d of $(OAm)_2SnI_4$, $(C_8H_{17}NH_3)_2SnI_4$, and $(C_6H_{13}NH_3)_2SnI_4$ is calculated to be 3.9, 2.3, and 1.9 nm, respectively

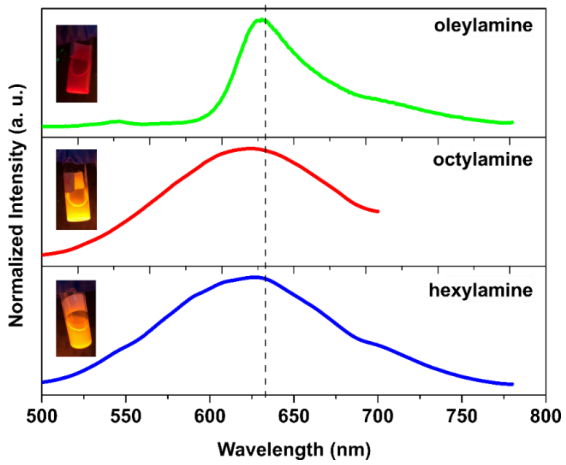

Appendix 4.3. PL spectra of the $(OAm)_2SnI_4$, $(C_8H_{17}NH_3)_2SnI_4$, and $(C_6H_{13}NH_3)_2SnI_4$ 2D perovskites, which are prepared by oleylamine, octylamine, and hexylamine, respectively. Insets: Photographs of 2D perovskites under UV light.

CHAPTER 5

Conclusion and prospects

Abstract: *In this thesis, several encapsulation approaches for lead halide perovskite nanocrystals have been discussed. The composites synthesized via molten salt synthesis exhibit strong photoluminescence emission, significantly enhanced stability and good performance in a proof-of-device application. This strategy method can be extended to prepare other composites such as other perovskite nanocrystals (e.g., lead-free perovskites) or chalcogenide nanocrystals inside different metal oxide hosts. This last chapter summarizes the achieving results of the PhD project and provides some suggestions for future prospects.*

5.1. Conclusion

This Ph.D. thesis encompasses three projects, each of them achieving the proposed target. The first two projects are mainly about lead halide perovskites encapsulated in silica, and the last one is related to the tin-based halide perovskite materials.

Efficient encapsulating strategies for lead halide perovskites (LHPs) are developed to improve their stability and examine their properties to be suitable for optoelectronic applications. An easy and straightforward procedure to produce $CsPbX_3$ NCs embedded inside a silica matrix is developed relying on the sol-gel reaction. The use of an aqueous acid solution HNO_3 in the reaction mixture not only triggers the transformation from Cs_4PbX_6 0D to $CsPbX_3$ 3D NCs but also simultaneously catalyzes the rapid hydrolysis of TEOS to grow a silica matrix fully embedding the final 3D NCs. The obtained $CsPbX_3/SiO_x$ composites feature enhanced stability (against thermal and water) thanks to the protection of the silica layer. To demonstrate the ability of these composites in the application, the W-LED is fabricated by implementing green and red-emitting $CsPbX_3/SiO_x$ composites enclosed with a blue InGaN LED. This W-LED is then characterized a color coordinate close to that of the ideal white light and a good color rendering index.

The amorphous silica is formed at room temperature, however, remains the pores on the surface (because of porosity in the silica network),[216] which would make LHP NCs gradually degrade. These pores are only collapsed when silica is calcined at high temperatures (above 600 ºC). This finding encourages exploring another method to protect LHP more efficiently.

As evolution in the LHPs encapsulation approach, a new molten salt synthesis route is developed to produce the composites made of $CsPbBr_3$ NCs and molten salts (KNO_3-$NaNO_3$-KBr) embedded inside mesoporous silica (m-SiO_2) particles. The use of molten salts delivers $CsPbBr_3$/m-SiO_2 composites with high PLQY (~90 %) and, simultaneously, for the sealing of SiO_2 pores, thus conferring exceptional stability to the system. These $CsPbBr_3$/m-SiO_2 composites are resistant to heat, water, even aqua regia and able to be promising as green-emitting phosphors in LEDs. The device is made with these composites emits white light with CIE color coordinates of (0.2985, 0.3076) and CCT of 7692 K and exhibits a highly stable PL emission after 240 hours of operation. Also, the composites retain their PL emission after being exposed to high salinity at 90 °C for 7 days, which allows them to be promising candidates as tracers for the oil industry.

The enhanced stability of the LHP/silica composites in *chapters 2* and *3* strongly proves the effectiveness of these new encapsulating methods for LHPs, and these composites are possibly be used in optoelectronic applications such as LEDs.

In the third project (*chapter 4*), motivated by working with a non-toxic lead-free material, two types of tin-based perovskites are synthesized and characterized: Cs_2SnI_6 3D perovskite and $(C_{18}H_{35}NH_3)_2SnI_4$ 2D perovskite. The Cs_2SnI_6 3D perovskite crystals have a size of 100 nm, a broad absorption band at 680 nm, and no emission, whereas $(OAm)_2SnI_4$ 2D perovskite with layer structure has a broad emission at 630 nm. These results can be the premise for further research of lead-free perovskite materials to be optimized optical properties or explore new structures.

5.2. Outlook

LHPs have outstanding optical properties; however, their soft nature limits their applications. Many research groups have attempted to improve the stability of LHPs, but crucial and effective solutions have rarely been suggested. The novel methods for the LHPs encapsulating, especially the use of silica combining with molten salt synthesis (*chapter 3*), could be one of the proper solutions. As a simple and powerful method, these methods can be extended to synthesize many types of nanomaterials. Some suggestions are described below:

(1) Despite LHPs have excellent optical properties and the best performance among the HPs family, and the stability of LHPs has been improved by many techniques to date, the existence of such materials that contain lead, an element that is toxic to humans, is an unavoidable fact. Thus, less-toxic environmental-friendly materials such as lead-free tin-based perovskites or double perovskites could be considered as alternative materials. These perovskites are probably synthesized by the use of molten salt synthesis and silica, based on the experiences with LHPs synthesis.

(2) Molten salts have been successfully employed for synthesizing several semiconductor NCs and QDs such as GaAs $In_{1-x}Ga_xP$, $In_{1-x}Ga_xAs$.[213-216] As a result, many III-V phase compositions are difficult to synthesize using the conventional solution process but can be achieved using the molten salt method.

(3) Future research should bridge the gap between the material and the applications. This gap is the quality of thin-film in device fabrication. The composites obtained here are very large (> 200 nm), which might be aggregated during the process of thin-film fabrication. Smaller particles (≤200 nm) are needed for synthesis, which can be accomplished using small silica particles in encapsulation methods. Another hypothesis is that composites made up of NCs embedded in silica can be functionalized with the desired functional groups thanks to silica's accessible functionalizing surface property, resulting in a robust colloidal solution that can be used in inkjet technique or thin-film fabrication.

ACKNOWLEDGMENTS

First of all, I would like to express my sincere gratitude to my supervisors, ***Liberato Manna*** *and* ***Luca De Trizio****; without their valuable guidance, I think it would have been difficult for me to reach this final goal. It is an honor to have the opportunity to learn from them.*

I would like to express my special thanks to ***Sungwook Park*** *for his help and support in this project, including his personal and professional guidance, encouraging support, and being a nice advisor, college, and friend.*

I gratefully acknowledge all members of the Nanochemistry group, who created a friendly research environment and shared experiences in practical work. I am also grateful to technicians from the NACH lab, XRD lab, and EM lab; this research would not have been completed without their help. Special thanks to the staff from IIT and UniGe, who helped me deal with the documents and administrative procedures.

I would like to thank ***Osman Bakr****,* ***Marat Lutfullin****, and* ***Lutfan Sinatra*** *for giving me an opportunity to collaborate with their research groups.*

In particular, I would like to thank my office mate ***Lía Vásquez*** *for her caring attitude and for being a lovely friend.*

Especially, I would like to thank my designer ***Ha Tran Hai*** *to help me complete the cover of this thesis.*

Finally, at home, I am indebted to my family for their love and continuous encouragement over the past three years.

15th December 2020

Mai Ngoc An

PUBLICATIONS

I. Patent application:

PARK Sungwook, **AN Mai Ngoc**, MANNA Liberato, DE TRIZIO Luca, LUTFULLIN Marat, SINATRA Lutfan, BAKR Osman Mohammed. "Method for Preparing Metal Halide Nanocomposites". IT 102020000018481, filed on July 29, **2020**.

II. Publications:

1. **Mai Ngoc An**, Rosaria Brescia, Marat Lutfullin, Lutfan Sinatra, Osman Bakr, Luca De Trizio and Liberato Manna. "Low Temperature Molten Salts Synthesis: $CsPbBr_3$ Nanocrystals with High Photoluminescence Emission Buried in Mesoporous SiO_2". *ACS Energy Lett*, **2021***, 6, 900–907.*
2. Sungwook Park, **Mai Ngoc An**, Guilherme Almeida, Francisco Palazon, Davide Spirito, Roman Krahne, Zhiya Dang, Luca De Trizio and Liberato Manna. "$CsPbX_3/SiO_x$ (X = Cl, Br, I) monoliths prepared via a novel sol–gel route starting from Cs_4PbX_6 nanocrystals". *Nanoscale*, **2019**, 11, 18739-18745.
3. Lía Vásquez, Alexander Davis, Francesca Gatto, **Mai Ngoc An**, Filippo Drago, Pier Paolo Pompa, Athanassia Athanassiou, Despina Fragouli. "Multifunctional PDMS polyHIPE filters for oil-water separation and antibacterial activity". *Separation and Purification Technology*, **2021**, Volume 255, 117748.

X-ray Diffraction (XRD) measurements

XRD patterns of the samples in *chapter 2*, *3*, *4* are acquired on a PAN analytical Empyrean X-ray diffractometer, equipped with a 1.8 kW Cu Kα ceramic X-ray tube and a PIXcel3D 2 × 2 area detector, using parallel beam geometry and symmetric reflection mode, operating at 45 kV and 40 mA under ambient conditions. The samples are prepared by drop-casting the solutions (i.e., Cs_4PbX_6 NCs dispersed in toluene in *chapter 2* and tin-perovskite samples in *chapter 4*) or pressing the composite powders (i.e., $CsPbX_3/SiO_x$ composites in *chapter 2* and $CsPbBr_3$/m-SiO_2 in *chapter 3*) onto a quartz zero-diffraction single crystal substrate.

Optical measurements.

The UV−Vis absorption spectra of the samples in *chapter 2* and *3* are recorded using a Varian Cary 5000 UV−Vis-NIR spectrophotometer equipped with an integrating sphere. The PL spectra are measured on a Varian Cary Eclipse spectrophotometer using an excitation wavelength of 350 nm. The samples are prepared by dispersing the composite powders in hexane, followed by drop-casting onto a quartz substrate. In thermal and water stability tests in *chapter 2*, PL spectra are recorded on an Ocean Optics HR4000 spectrometer with an excitation wavelength of 385 nm.

PLQY measurements of the samples in *chapter 3* are performed using Fluorescence Spectrometer FS5 Edinburgh Instruments equipped with an integrating sphere. Measurement of LED color position, CCT, and CRI parameters is performed with GL Spectis 5.0 touch-GL Optic spectrometers.

In *chapter 4*, the UV−Vis absorption spectra are recorded using a Varian Cary 300 UV−vis absorption spectrophotometer. The PL spectra are measured on a Varian Cary Eclipse spectrophotometer using an excitation wavelength of 370 nm for all samples. Samples are prepared by diluting crystal solutions in toluene in quartz cuvettes with a path length of 1 cm.

Transmission Electron Microscopy (TEM) measurements

Low-resolution TEM measurement of all the samples in *chapter 2*, *3*, and 4 is performed on a JEOL-1100 TEM operating at an acceleration voltage of 100kV.

In *chapter 2*, high-resolution TEM (HRTEM), high angle annular dark-field scanning TEM (HAADF-STEM), and Energy-dispersive X-ray spectroscopy (EDS) measurements are carried out on a JEOL JEM-2200FS microscope equipped with a 200 kV field emission gun, a CEOS spherical aberration corrector for the objective lens and an in-column image filter (Ω-type), on which a Bruker Quantax 400 system with a 60 mm^2 XFlash 6 T silicon drift detector (SDD) is mounted. Samples are prepared by dispersing the composite powders in hexane, followed by drop-casting onto carbon-coated copper grids.

In *chapter 3*, HRTEM and HAADF-STEM imaging are carried out on a JEOL JEM-2200FS TEM (Schottky emitter), equipped with a CEOS corrector for the objective lens and an in-column image filter (Ω-type), operated at 200 kV. The samples are exposed to a relatively low dose rate (~ 30 electrons/($Å^2$ s)) to avoid electron beam damage. HRTEM images are acquired using a direct electron detection camera (K2 Summit, Gatan) in super-resolution mode. All images are obtained from a $(260\ nm)^2$ frame obtained by summing aligned frames receiving short exposure (0.4 s), with a total acquisition time of 12 s. STEM - EDS data are acquired in STEM mode by a Bruker XFlash 5060 silicon-drift detector installed on the same microscope. For HRTEM, HAADF-STEM, and STEM-EDS mapping, samples are prepared by mildly sonicating the composite powder suspended in ethanol and drop-casting the suspension supernatant onto a holey carbon film on Cu. The grid is heated to 150 °C for 5 hours (in high vacuum, $p \leq 10^{-6}$ mbar) before the experiment. The sample is kept in a high vacuum the night before the measurements.

In *chapter 4*, EDS measurements are carried out on a JEOL JEM-2200FS microscope equipped with a 200 kV field emission gun, a CEOS spherical aberration corrector for the objective lens, and an in-column image filter (Ω-type), on which a Bruker Quantax 400 system with a 60 mm^2 XFlash 6 T silicon drift detector (SDD) is mounted. Samples are prepared by drop-casting onto carbon-coated copper grids.

Dynamic Light Scattering (DLS) measurements

DLS measurements in *chapter 3* are performed by using a Zetasizer Nano S from Malvern Pananalytical. The starting m-SiO_2 is dispersed in water for measurement. The composites are dispersed in water or the brine solution for the measurements. The refractive index of the $CsPbBr_3$/m-SiO_2 composites is taken from the work of Yan et al.[217]

LIST OF CHEMICALS

- Benzoyl chloride (C_6H_5COCl, 98 %)
- Cesium bromide (CsBr, 99.999 %)
- Cesium carbonate (Cs_2CO_3, reagent Plus, 99 %)
- Dimethylsulfoxide (DMSO)
- Hexylamine ($CH_3(CH_2)_5NH_2$, 99 %)
- Iodotrimethylsilane ($(CH_3)_3SiI$, 97%)
- Lead (II) bromide ($PbBr_2$, 99.999 % trace metals basis)
- Lead (II) chloride ($PbCl_2$, 99.999 % trace metals basis)
- Lead (II) iodide (PbI_2, 99.999 % trace metals basis)
- Lead (II) oxide (PbO, 99.999 % trace metals basis)
- Manganese (II) acetate tetrahydrate ($(CH_3COO)_2Mn{\cdot}4H_2O$, 99.99 % trace metals basis)
- Nitric acid (HNO_3, puriss. p.a., ≥ 65 % w/w (T))
- N-hexane (99.5 %)
- Toluene (anhydrous, 99.5 %)
- Octadecene (ODE, technical grade, 90 %)
- Oleic acid (OA, 90 %)
- Oleylamine (OLAM, 70 %)
- Octylamine ($CH_3(CH_2)_7NH_2$, 99 %)
- Poly(dimethylsiloxane) (PDMS)
- Polymethylmethacrylate (PMMA, powder)
- Potassium bromide (KBr, 99.99 %)
- Potassium nitrate (KNO_3, 99.999 %)
- Silica (mesostructured, MCM-41 type, product code 643645)
- Sodium iodide (NaI, 99.99 %)
- Sodium nitrate ($NaNO_3$, 99.995 %)
- Toluene (anhydrous, 99.5 %)
- Tin (IV) acetate ($Sn(CH_3CO_2)_4$, 99.99 %)
- Tetraethyl orthosilicate (TEOS, 99.999 % trace metals basis)

LIST OF ABBREVIATIONS

0/1/2/3D	0/1/2/3 Dimensional
Abs	Absorption
APTES	(3-aminopropyl) triethoxysilane
CB	Conduction Band
CBM	Conduction Band Minimum
CCT	Correlated Color Temperature
CIE	Commission Internationale de l'Eclairage
CRI	Color Rendering Index
DI	Deionized
DLS	Dynamic Light Scattering
DMF	Dimethyl Formamide
DMSO	Dimethylsulfoxide
EDS	Energy-Dispersive X-ray
EVA	Ethylene-vinyl acetate
FA	Formamidinium
FWHM	Full Width at Half Maximum
GC	Gas Chromatography
HAADF	High-Angle Annular Dark-Field
HP	Halide Perovskite
HRTEM	High Resolution Transmission Electron Microscopy
HAADF	High-Angle Annular Dark-Field
HP	Halide Perovskite
HRTEM	High Resolution Transmission Electron Microscopy
NC	Nanocrystal
ICP	Inductively Coupled Plasma Optical Emission Spectroscopy
IR	Infra-red
LCD	Liquid-Crystal Display
LE	Luminous Efficacy
LED	Light Emitting Diode
LHP	Lead Halide Perovskite
LARP	Ligand-assisted Reprecipitation
MA	Methylammonium
MABr	Methylammoniumbromide
MOF	Metal-Organic Framework
m-SiO_2	mesoporous silica
N/A	Not Available
NIR	Near Infra-red
NTSC	National Television System Committee
OA	Oleic Acid
ODE	1-Octadecene
OLA	Oleylamine
pc-LED	phosphor-converted Light Emitting Diode
PCE	Power Conversion Efficiency

LIST OF ABBREVIATIONS

PhD	Doctor of Philosophy
PL	Photoluminescence
PLE	Photoluminescence Excitation
PLQY	Photoluminescence Quantum Yield
PMMA	Poly(methyl methacrylate)
PS	Polystyrene
PSC	Perovskite solar cell
PTA	1,4-dicarboxybenzene
QD	Quantum Dot
QLCD	Quantum Dot Liquid-Crystal Display
RT	Room Temperature
SEM	Scanning Electron Microscope
SiO_2	Silica
STEM	Scanning Transmission Electron Micrograph
STEM	Scanning Transmission Electron Microscope
TEM	Transmission Electron Microscopy
TEOS	Tetraethoxysilane
TMOS	Tetramethoxysilane
UV	Ultra Violet
VB	Valance Band
VBM	Valance Band Maximum
Vis	Visible
XRD	X-Ray Diffraction
W-LED	White Light Emitting Diode

REFERENCES

1. Zhao, Y.; Zhu, K., Organic–inorganic hybrid lead halide perovskites for optoelectronic and electronic applications. *Chemical Society Reviews* **2016**, 45 (3), 655-689.
2. Guo, X.; Burda, C., Coordination engineering toward high performance organic–inorganic hybrid perovskites. *Coordination Chemistry Reviews* **2016**, 320-321, 53-65.
3. Manser, J. S.; Christians, J. A.; Kamat, P. V., Intriguing Optoelectronic Properties of Metal Halide Perovskites. *Chemical Reviews* **2016**, 116 (21), 12956-13008.
4. Ha, S.-T.; Su, R.; Xing, J.; Zhang, Q.; Xiong, Q., Metal halide perovskite nanomaterials: synthesis and applications. *Chemical Science* **2017**, 8 (4), 2522-2536.
5. Shi, Z.; Guo, J.; Chen, Y.; Li, Q.; Pan, Y.; Zhang, H.; Xia, Y.; Huang, W., Lead-Free Organic-Inorganic Hybrid Perovskites for Photovoltaic Applications: Recent Advances and Perspectives. *Advanced Materials* **2017**, 29 (16), 1605005.
6. Goldschmidt, V. M., Die Gesetze der Krystallochemie. *Naturwissenschaften* **1926**, 14 (21), 477-485.
7. Ju, M.-G.; Dai, J.; Ma, L.; Zeng, X. C., Lead-Free Mixed Tin and Germanium Perovskites for Photovoltaic Application. *Journal of the American Chemical Society* **2017**, 139 (23), 8038-8043.
8. Green, M. A.; Ho-Baillie, A.; Snaith, H. J., The emergence of perovskite solar cells. *Nature Photonics* **2014**, 8 (7), 506-514.
9. Travis, W.; Glover, E. N. K.; Bronstein, H.; Scanlon, D. O.; Palgrave, R. G., On the application of the tolerance factor to inorganic and hybrid halide perovskites: a revised system. *Chemical Science* **2016**, 7 (7), 4548-4556.
10. Kovalenko, M. V.; Protesescu, L.; Bodnarchuk, M. I., Properties and potential optoelectronic applications of lead halide perovskite nanocrystals. *Science* **2017**, 358 (6364), 745.
11. Yi, Z.; Ladi, N. H.; Shai, X.; Li, H.; Shen, Y.; Wang, M., Will organic–inorganic hybrid halide lead perovskites be eliminated from optoelectronic applications? *Nanoscale Advances*, **2019**, 1 (4), 1276-1289.
12. Dunlap-Shohl, W. A.; Zhou, Y.; Padture, N. P.; Mitzi, D. B., Synthetic Approaches for Halide Perovskite Thin Films. *Chemical Reviews* **2019**, 119 (5), 3193-3295.

REFERENCES

13. Ashurov, N.; Oksengendler, B. L.; Maksimov, S.; Rashiodva, S.; Ishteev, A. R.; Saranin, D. S.; Burmistrov, I. N.; Kuznetsov, D. V.; Zakhisov, A. A., Current state and perspectives for organo-halide perovskite solar cells. *Modern Electronic Materials* **2017**, 3 (1), 1-25.
14. Zhu, Z.; Sun, Q.; Zhang, Z.; Dai, J.; Xing, G.; Li, S.; Huang, X.; Huang, W., Metal halide perovskites: stability and sensing-ability. *Journal of Materials Chemistry C* **2018**, 6 (38), 10121-10137.
15. Wang, J.; Dong, J.; Lu, F.; Sun, C.; Zhang, Q.; Wang, N., Two-dimensional lead-free halide perovskite materials and devices. *Journal of Materials Chemistry A* **2019**, 7 (41), 23563-23576.
16. Mao, L.; Guo, P.; Kepenekian, M.; Spanopoulos, I.; He, Y.; Katan, C.; Even, J.; Schaller, R. D.; Seshadri, R.; Stoumpos, C. C.; Kanatzidis, M. G., Organic Cation Alloying on Intralayer A and Interlayer A' sites in 2D Hybrid Dion–Jacobson Lead Bromide Perovskites $A'APb_2Br_7$. *Journal of the American Chemical Society* **2020**, 142 (18), 8342-8351.
17. Mao, L.; Stoumpos, C. C.; Kanatzidis, M. G., Two-Dimensional Hybrid Halide Perovskites: Principles and Promises. *Journal of the American Chemical Society*, **2019**, 141 (3), 1171-1190.
18. Zhang, H.; Liao, Q.; Wu, Y.; Chen, J.; Gao, Q.; Fu, H., Pure zero-dimensional Cs_4PbBr_6 single crystal rhombohedral microdisks with high luminescence and stability. *Physical Chemistry Chemical Physics* **2017**, 19 (43), 29092-29098.
19. Qin, Z.; Dai, S.; Hadjiev, V. G.; Wang, C.; Xie, L.; Ni, Y.; Wu, C.; Yang, G.; Chen, S.; Deng, L.; Yu, Q.; Feng, G.; Wang, Z. M.; Bao, J., Revealing the Origin of Luminescence Center in 0D Cs_4PbBr_6 Perovskite. *Chemistry of Materials* **2019**, 31 (21), 9098-9104.
20. Bergerhoff, G.; Schmitz-Dumont, O., Die Kristallstruktur des Kaliumhexachlorocadmats(II). *Zeitschrift für anorganische und allgemeine Chemie* **1956**, 284 (13), 10-19.
21. Kondo, S.; Amaya, K.; Saito, T., Localized optical absorption in Cs_4PbBr_6. *Journal of Physics: Condensed Matter* **2002**, 14 (8), 2093-2099.
22. Saidaminov, M. I.; Almutlaq, J.; Sarmah, S.; Dursun, I.; Zhumekenov, A. A.; Begum, R.; Pan, J.; Cho, N.; Mohammed, O. F.; Bakr, O. M., Pure Cs_4PbBr_6: Highly Luminescent Zero-Dimensional Perovskite Solids. *ACS Energy Letters* **2016**, 1 (4), 840-845.

REFERENCES

23. Ravi, V. K.; Markad, G. B.; Nag, A., Band Edge Energies and Excitonic Transition Probabilities of Colloidal $CsPbX_3$ (X = Cl, Br, I) Perovskite Nanocrystals. *ACS Energy Letters* **2016**, 1 (4), 665-671.
24. Stoumpos, C. C.; Kanatzidis, M. G., Halide Perovskites: Poor Man's High-Performance Semiconductors. *Advanced Materials*, **2016**, 28 (28), 5778-5793.
25. Brandt, R. E.; Stevanović, V.; Ginley, D. S.; Buonassisi, T., Identifying defect-tolerant semiconductors with high minority-carrier lifetimes: beyond hybrid lead halide perovskites. *MRS Communications* **2015**, 5 (2), 265-275.
26. Protesescu, L.; Yakunin, S.; Bodnarchuk, M. I.; Krieg, F.; Caputo, R.; Hendon, C. H.; Yang, R. X.; Walsh, A.; Kovalenko, M. V., Nanocrystals of Cesium Lead Halide Perovskites ($CsPbX_3$, X = Cl, Br, and I): Novel Optoelectronic Materials Showing Bright Emission with Wide Color Gamut. *Nano Letters* **2015**, 15 (6), 3692–3696.
27. Peedikakkandy, L.; Bhargava, P., Composition dependent optical, structural and photoluminescence characteristics of cesium tin halide perovskites. *RSC Advances*, **2016**, 6 (24), 19857-19860.
28. Jellicoe, T. C.; Richter, J. M.; Glass, H. F.; Tabachnyk, M.; Brady, R.; Dutton, S. E.; Rao, A.; Friend, R. H.; Credgington, D.; Greenham, N. C.; Böhm, M. L., Synthesis and Optical Properties of Lead-Free Cesium Tin Halide Perovskite Nanocrystals. *Journal of the American Chemical Society* **2016**, 138 (9), 2941–2944.
29. Chen, Q.; De Marco, N.; Yang, Y.; Song, T.-B.; Chen, C.-C.; Zhao, H.; Hong, Z.; Zhou, H.; Yang, Y., Under the spotlight: The organic–inorganic hybrid halide perovskite for optoelectronic applications. *Nano Today* **2015**, 10 (3), 355-396.
30. Benny, F.; Yulia, L.; Jagjit, K.; Thomas J. N., H.; Padinhare Cholakkal, H.; Ming Hui, L.; Teck Ming, K.; Sudip, C.; Ze Xiang, S.; Nripan, M.; Jason, E., Formation of Corrugated n=1 2D Tin Iodide Perovskites and Their Use as Lead-Free Solar Absorbers. *ACS Nano* **2021** (Publication date: Aprill 5, 2021).
31. Febriansyah, B.; Giovanni, D.; Ramesh, S.; Koh, T. M.; Li, Y.; Sum, T. C.; Mathews, N.; England, J., Inducing formation of a corrugated, white-light emitting 2D lead-bromide perovskite via subtle changes in templating cation. *Journal of Materials Chemistry C* **2020**, 8 (3), 889-893.

REFERENCES

32. Mao, L.; Wu, Y.; Stoumpos, C. C.; Wasielewski, M. R.; Kanatzidis, M. G., White-Light Emission and Structural Distortion in New Corrugated Two-Dimensional Lead Bromide Perovskites. *Journal of the American Chemical Society* **2017**, 139 (14), 5210-5215.
33. Kovalenko, M.; Protesescu, L.; Bodnarchuk, M. A, Properties and potential optoelectronic applications of lead halide perovskite nanocrystals. *Science* **2017**, 358 (6364), 745-750.
34. Kang, J.; Wang, L.-W., High Defect Tolerance in Lead Halide Perovskite $CsPbBr_3$. *The Journal of Physical Chemistry Letters* **2017**, 8 (2), 489-493.
35. Sun, S.; Yuan, D.; Xu, Y.; Wang, A.; Deng, Z., Ligand-Mediated Synthesis of Shape-Controlled Cesium Lead Halide Perovskite Nanocrystals via Reprecipitation Process at Room Temperature. *ACS Nano* **2016**, 10 (3), 3648-3657.
36. Teunis, M. B.; Johnson, M. A.; Muhoberac, B. B.; Seifert, S.; Sardar, R., Programmable Colloidal Approach to Hierarchical Structures of Methylammonium Lead Bromide Perovskite Nanocrystals with Bright Photoluminescent Properties. *Chemistry of Materials* **2017**, 29 (8), 3526-3537.
37. Zhang, F.; Zhong, H.; Chen, C.; Wu, X.-g.; Hu, X.; Huang, H.; Han, J.; Zou, B.; Dong, Y., Brightly Luminescent and Color-Tunable Colloidal $CH_3NH_3PbX_3$ (X = Br, I, Cl) Quantum Dots: Potential Alternatives for Display Technology. *ACS Nano* **2015**, 9 (4), 4533-4542.
38. Chouhan, L.; Ghimire, S.; Subrahmanyam, C.; Miyasaka, T.; Biju, V., Synthesis, optoelectronic properties and applications of halide perovskites. *Chem Soc Rev* **2020**, 49 (10), 2869-2885.
39. Protesescu, L.; Yakunin, S.; Bodnarchuk, M. I.; Krieg, F.; Caputo, R.; Hendon, C. H.; Yang, R. X.; Walsh, A.; Kovalenko, M. V., Nanocrystals of Cesium Lead Halide Perovskites ($CsPbX_3$, X = Cl, Br, and I): Novel Optoelectronic Materials Showing Bright Emission with Wide Color Gamut. *Nano Letters* **2015**, 15 (6), 3692-3696.
40. Shekhirev, M.; Goza, J.; Teeter, J. D.; Lipatov, A.; Sinitskii, A., Synthesis of Cesium Lead Halide Perovskite Quantum Dots. *Journal of Chemical Education* **2017**, 94 (8), 1150-1156.
41. Zhang, J.; Yang, Y.; Deng, H.; Farooq, U.; Yang, X.; Khan, J.; Tang, J.; Song, H., High Quantum Yield Blue Emission from Lead-Free Inorganic Antimony Halide Perovskite Colloidal Quantum Dots. *ACS Nano* **2017**, 11, 9, 9294–9302.

REFERENCES

42. Li, Y.-F.; Feng, J.; Sun, H.-B., Perovskite quantum dots for light-emitting devices. *Nanoscale* **2019**, 11 (41), 19119-19139.

43. Chen, Q.; Wu, J.; Ou, X.; Huang, B.; Almutlaq, J.; Zhumekenov, A. A.; Guan, X.; Han, S.; Liang, L.; Yi, Z.; Li, J.; Xie, X.; Wang, Y.; Li, Y.; Fan, D.; Teh, D. B. L.; All, A. H.; Mohammed, O. F.; Bakr, O. M.; Wu, T.; Bettinelli, M.; Yang, H.; Huang, W.; Liu, X., All-inorganic perovskite nanocrystal scintillators. *Nature* **2018**, 561 (7721), 88-93.

44. Wu, Z.; Liu, P.; Zhang, W.; Wang, K.; Sun, X. W., Development of InP Quantum Dot-Based Light-Emitting Diodes. *ACS Energy Letters* **2020**, 5 (4), 1095-1106.

45. Han, C.-Y.; Lee, S.-H.; Song, S.-W.; Yoon, S.-Y.; Jo, J.-H.; Jo, D.-Y.; Kim, H.-M.; Lee, B.-J.; Kim, H.-S.; Yang, H., More Than 9 % Efficient ZnSeTe Quantum Dot-Based Blue Electroluminescent Devices. *ACS Energy Letters* **2020**, 5 (5), 1568-1576.

46. Jiang, M.; Hu, Z.; Liu, Z.; Wu, Z.; Ono, L. K.; Qi, Y., Engineering Green-to-Blue Emitting $CsPbBr_3$ Quantum-Dot Films with Efficient Ligand Passivation. *ACS Energy Letters* **2019**, 4 (11), 2731-2738.

47. Hassan, Y.; Ashton, O. J.; Park, J. H.; Li, G.; Sakai, N.; Wenger, B.; Haghighirad, A.-A.; Noel, N. K.; Song, M. H.; Lee, B. R.; Friend, R. H.; Snaith, H. J., Facile Synthesis of Stable and Highly Luminescent Methylammonium Lead Halide Nanocrystals for Efficient Light Emitting Devices. *Journal of the American Chemical Society* **2019**, 141 (3), 1269-1279.

48. Wang, H. C.; Lin, S. Y.; Tang, A. C.; Singh, B. P.; Tong, H. C.; Chen, C. Y.; Lee, Y. C.; Tsai, T. L.; Liu, R. S., Mesoporous Silica Particles Integrated with All-Inorganic $CsPbBr_3$ Perovskite Quantum-Dot Nanocomposites (MP-PQDs) with High Stability and Wide Color Gamut Used for Backlight Display. **2016**, 55 (28), 7924-7929.

49. Sun, C.; Zhang, Y.; Ruan, C.; Yin, C.; Wang, X.; Wang, Y.; Yu, W. W., Efficient and Stable White LEDs with Silica-Coated Inorganic Perovskite Quantum Dots. *Advanced Materials* **2016**, 28 (45), 10088-10094.

50. Sun, J.-Y.; Rabouw, F. T.; Yang, X.-F.; Huang, X.-Y.; Jing, X.-P.; Ye, S.; Zhang, Q.-Y., Facile Two-Step Synthesis of All-Inorganic Perovskite $CsPbX_3$ (X = Cl, Br, and I) Zeolite-Y Composite Phosphors for Potential Backlight Display Application. *Advanced Functional Materials* **2017**, 27 (45), 1704371.

REFERENCES

51. Wei, Y.; Xiao, H.; Xie, Z.; Liang, S.; Liang, S.; Cai, X.; Huang, S.; Al Kheraif, A. A.; Jang, H. S.; Cheng, Z.; Lin, J., Highly Luminescent Lead Halide Perovskite Quantum Dots in Hierarchical CaF_2 Matrices with Enhanced Stability as Phosphors for White Light-Emitting Diodes. *Advanced Optical Materials* **2018**, 6 (11), 1701343.
52. Yoon, Y. J.; Chang, Y.; Zhang, S.; Zhang, M.; Pan, S.; He, Y.; Lin, C. H.; Yu, S.; Chen, Y.; Wang, Z.; Ding, Y.; Jung, J.; Thadhani, N.; Tsukruk, V. V.; Kang, Z.; Lin, Z. A.-O., Enabling Tailorable Optical Properties and Markedly Enhanced Stability of Perovskite Quantum Dots by Permanently Ligating with Polymer Hairs. *Advanced Materials* **2019**, 31 (32), 1901602.
53. Xuan, T.; Huang, J.; Liu, H.; Lou, S.; Cao, L.; Gan, W.; Liu, R.-S.; Wang, J., Super-Hydrophobic Cesium Lead Halide Perovskite Quantum Dot-Polymer Composites with High Stability and Luminescent Efficiency for Wide Color Gamut White Light-Emitting Diodes. *Chemistry of Materials* **2019**, 31 (3), 1042-1047.
54. Wang, B.; Zhang, C.; Zheng, W.; Zhang, Q.; Bao, Z.; Kong, L.; Li, L., Large-Scale Synthesis of Highly Luminescent Perovskite Nanocrystals by Template-Assisted Solid-State Reaction at 800 °C. *Chemistry of Materials* **2020**, 32 (1), 308-314.
55. Wei, Y.; Cheng, Z.; Lin, J., An overview on enhancing the stability of lead halide perovskite quantum dots and their applications in phosphor-converted LEDs. *Chemical Society Reviews* **2019**, 48 (1), 310-350.
56. Zhou, J.; Huang, F.; Lin, H.; Lin, Z.; Xu, J.; Wang, Y., Inorganic halide perovskite quantum dot modified YAG-based white LEDs with superior performance. *Journal of Materials Chemistry C* **2016**, 4 (32), 7601-7606.
57. Yoshihiro, O. Color rendering and luminous efficacy of white LED spectra, *Proc.SPIE*, **2004**.
58. Xu, R.-P.; Li, Y.-Q.; Jin, T.-Y.; Liu, Y.-Q.; Bao, Q.-Y.; O'Carroll, C.; Tang, J.-X., In Situ Observation of Light Illumination-Induced Degradation in Organometal Mixed-Halide Perovskite Films. *ACS Applied Materials & Interfaces* **2018**, 10 (7), 6737-6746.
59. Huang, S.; Li, Z.; Wang, B.; Zhu, N.; Zhang, C.; Kong, L.; Zhang, Q.; Shan, A.; Li, L., Morphology evolution and degradation of $CsPbBr_3$ nanocrystals under blue light-emitting diode illumination. *ACS Applied Materials & Interfaces* **2017**, 9 (8), 7249-7258.

REFERENCES

60. Leguy, A. M.; Hu, Y.; Campoy-Quiles, M.; Alonso, M. I.; Weber, O. J.; Azarhoosh, P.; Van Schilfgaarde, M.; Weller, M. T.; Bein, T.; Nelson, J., Reversible hydration of $CH_3NH_3PbI_3$ in films, single crystals, and solar cells. *Chemistry of Materials* **2015**, 27 (9), 3397-3407.
61. Akbali, B.; Topcu, G.; Guner, T.; Ozcan, M.; Demir, M. M.; Sahin, H., CsPbBr 3 perovskites: Theoretical and experimental investigation on water-assisted transition from nanowire formation to degradation. *Physical Review Materials* **2018**, 2 (3), 034601.
62. Turedi, B.; Lee, K. J.; Dursun, I.; Alamer, B.; Wu, Z.; Alarousu, E.; Mohammed, O. F.; Cho, N.; Bakr, O. M., Water-induced dimensionality reduction in metal-halide perovskites. *The Journal of Physical Chemistry C* **2018**, 122 (25), 14128-14134.
63. Aristidou, N.; Sanchez-Molina, I.; Chotchuangchutchaval, T.; Brown, M.; Martinez, L.; Rath, T.; Haque, S. A., The Role of Oxygen in the Degradation of Methylammonium Lead Trihalide Perovskite Photoactive Layers. *Angewandte Chemie* **2015**, 54 (28), 8208-8212.
64. Aristidou, N.; Eames, C.; Sanchez-Molina, I.; Bu, X.; Kosco, J.; Islam, M. S.; Haque, S. A., Fast oxygen diffusion and iodide defects mediate oxygen-induced degradation of perovskite solar cells. *Nature Communications* **2017**, 8 (1), 15218.
65. Merdasa, A.; Bag, M.; Tian, Y.; Källman, E.; Dobrovolsky, A.; Scheblykin, I. G., Super-Resolution Luminescence Microspectroscopy Reveals the Mechanism of Photoinduced Degradation in $CH_3NH_3PbI_3$ Perovskite Nanocrystals. *The Journal of Physical Chemistry C* **2016**, 120 (19), 10711-10719.
66. Lorenzon, M.; Sortino, L.; Akkerman, Q.; Accornero, S.; Pedrini, J.; Prato, M.; Pinchetti, V.; Meinardi, F.; Manna, L.; Brovelli, S., Role of Nonradiative Defects and Environmental Oxygen on Exciton Recombination Processes in $CsPbBr_3$ Perovskite Nanocrystals. *Nano Letters* **2017**, 17 (6), 3844-3853.
67. Dualeh, A.; Gao, P.; Seok, S. I.; Nazeeruddin, M. K.; Grätzel, M., Thermal behavior of methylammonium lead-trihalide perovskite photovoltaic light harvesters. *Chemistry of Materials* **2014**, 26 (21), 6160-6164.
68. Kulbak, M.; Gupta, S.; Kedem, N.; Levine, I.; Bendikov, T.; Hodes, G.; Cahen, D., Cesium enhances long-term stability of lead bromide perovskite-based solar cells. *The Journal of Physical Chemistry Letters* **2016**, 7 (1), 167-172.

REFERENCES

69. Huang, H.; Bodnarchuk, M. I.; Kershaw, S. V.; Kovalenko, M. V.; Rogach, A. L., Lead Halide Perovskite Nanocrystals in the Research Spotlight: Stability and Defect Tolerance. *ACS Energy Letters* **2017**, 2 (9), 2071-2083.
70. Trots, D.; Myagkota, S., High-temperature structural evolution of caesium and rubidium triiodoplumbates. *Journal of Physics and Chemistry of Solids* **2008**, 69 (10), 2520-2526.
71. Conings, B.; Drijkoningen, J.; Gauquelin, N.; Babayigit, A.; D'Haen, J.; D'Olieslaeger, L.; Ethirajan, A.; Verbeeck, J.; Manca, J.; Mosconi, E.; Angelis, F. D.; Boyen, H.-G., Intrinsic Thermal Instability of Methylammonium Lead Trihalide Perovskite. *Advanced Energy Materials* **2015**, 5 (15), 1500477.
72. Heleen F. Sijbom, R. V., Jonas J. Joos, Dirk Poelman, and Philippe F. Smet, $K_2SiF_6:Mn^{4+}$ as a red phosphor for displays and warm-white LEDs: a review of properties and perspectives. *Optical Materials Express* **2017**, 7 (9), 3332-3365.
73. Shan, Q.; Li, J.; Song, J.; Zou, Y.; Xu, L.; Xue, J.; Dong, Y.; Huo, C.; Chen, J.; Han, B.; Zeng, H., All-inorganic quantum-dot light-emitting diodes based on perovskite emitters with low turn-on voltage and high humidity stability. *Journal of Materials Chemistry C* **2017**, 5 (18), 4565-4570.
74. Zhou, Y.; Chen, J.; Bakr, O. M.; Sun, H.-T., Metal-doped lead halide perovskites: synthesis, properties, and optoelectronic applications. *Chemistry of Materials* **2018**, 30 (19), 6589-6613.
75. Jiang, Q.; Chen, M.; Li, J.; Wang M Fau - Zeng, X.; Zeng, X.; Besara, T. A.-O.; Lu, J.; Xin, Y.; Shan, X.; Pan, B.; Wang, C.; Lin S Auid- Fau - Siegrist, T.; Siegrist T Fau - Xiao, Q.; Xiao, Q.; Yu, Z., Electrochemical Doping of Halide Perovskites with Ion Intercalation. *ACS Nano* **2017**, 11, 1, 1073–1079.
76. Liu, M.; Zhong, G.; Yin, Y.; Miao, J.; Li, K.; Wang, C.; Xu, X.; Shen, C.; Meng, H. X., Aluminum-Doped Cesium Lead Bromide Perovskite Nanocrystals with Stable Blue Photoluminescence Used for Display Backlight. *Advance Science* **2017**, 4 (11), 1700335.
77. Swarnkar, A.; Mir, W. J.; Nag, A., Can B-Site Doping or Alloying Improve Thermal- and Phase-Stability of All-Inorganic $CsPbX_3$ (X = Cl, Br, I) Perovskites? *ACS Energy Letters* **2018**, 3 (2), 286-289.

REFERENCES

78. Liu, F.; Zhang, Y.; Ding, C.; Kobayashi, S.; Izuishi, T.; Nakazawa, N.; Toyoda, T.; Ohta, T.; Hayase, S.; Minemoto, T.; Yoshino, K.; Dai, S.; Shen, Q., Highly Luminescent Phase-Stable $CsPbI_3$ Perovskite Quantum Dots Achieving Near 100 % Absolute Photoluminescence Quantum Yield. *ACS Nano* **2017**, 11, 10, 10373–10383.

79. Wu, H.; Zhang, Y.; Lu, M.; Zhang, X.; Sun, C.; Zhang, T.; Colvin, V. L.; Yu, W. W., Surface ligand modification of cesium lead bromide nanocrystals for improved light-emitting performance. *Nanoscale* **2018**, 10 (9), 4173-4178.

80. Pan, J.; Sarmah, S. P.; Murali, B.; Dursun, I.; Peng, W.; Parida, M. R.; Liu, J.; Sinatra, L.; Alyami, N.; Zhao, C.; Alarousu, E.; Ng, T. K.; Ooi, B. S.; Bakr, O. M.; Mohammed, O. F., Air-Stable Surface-Passivated Perovskite Quantum Dots for Ultra-Robust, Single- and Two-Photon-Induced Amplified Spontaneous Emission. *The Journal of Physical Chemistry Letters* **2015**, 6, 24, 5027–5033.

81. Woo, J. Y.; Kim, Y.; Bae, J.; Kim, T. G.; Kim, J. W.; Lee, D. C.; Jeong, S., Highly Stable Cesium Lead Halide Perovskite Nanocrystals through in Situ Lead Halide Inorganic Passivation. *Chemistry of Materials* **2017**, 29 (17), 7088-7092.

82. Li Y Fau - Lv, Y.; Lv Y Fau - Guo, Z.; Guo Z Fau - Dong, L.; Dong, L. A.-O.; Zheng, J.; Chai, C.; Chen N Fau - Lu, Y.; Lu Y Fau - Chen, C.; Chen, C., One-Step Preparation of Long-Term Stable and Flexible $CsPbBr_3$ Perovskite Quantum Dots/Ethylene Vinyl Acetate Copolymer Composite Films for White Light-Emitting Diodes. *ACS Applied Materials & Interfaces* **2018**, 10, 18, 15888–15894.

83. Ren, J. J.; Li, T. R.; Zhou, X. P.; Dong, X.; Shorokhov, A. V.; Semenov, M. B.; Krevchik, V. D.; Wang, Y. H., Encapsulating all-inorganic perovskite quantum dots into mesoporous metal organic frameworks with significantly enhanced stability for optoelectronic applications. *Chemical Engineering Journal* **2019**, 358, 30-39.

84. Zhou, L.; Yu, K.; Yang, F.; Zheng, J.; Zuo, Y.; Li, C.; Cheng, B.; Wang, Q., All-inorganic perovskite quantum dot/mesoporous TiO_2 composite-based photodetectors with enhanced performance. *Dalton Transactions* **2017**, 46 (6), 1766-1769.

REFERENCES

85. Yang, W.; Gao, F.; Qiu, Y.; Liu, W.; Xu, H.; Yang, L.; Liu, Y., $CsPbBr_3$-Quantum-Dots/Polystyrene@Silica Hybrid Microsphere Structures with Significantly Improved Stability for White LEDs. *Advanced Optical Materials* **2019**, 7 (13), 1900546.

86. Hu, Z. P.; Liu, Z. Z.; Bian, Y.; Li, S. Q.; Tang, X. S.; Du, J.; Zang, Z. G.; Zhou, M.; Hu, W.; Tian, Y. X.; Leng, Y. X., Enhanced Two-Photon-Pumped Emission from In Situ Synthesized Nonblinking $CsPbBr_3/SiO_2$ Nanocrystals with Excellent Stability. *Advanced Optical Materials* **2018**, 6 (3), 1700997.

87. Yang, D.; Li, X.; Zeng, H., Surface Chemistry of All Inorganic Halide Perovskite Nanocrystals: Passivation Mechanism and Stability. *Advanced Materials Interfaces* **2018**, 5 (8), 1701662.

88. Shan, Q.; Song, J.; Zou, Y.; Li, J.; Xu, L.; Xue, J.; Dong, Y.; Han, B.; Chen, J.; Zeng, H., High Performance Metal Halide Perovskite Light-Emitting Diode: From Material Design to Device Optimization. *Small* **2017**, 13 (45), 1701770.

89. Moon, H.; Lee, C.; Lee, W.; Kim, J.; Chae, H., Stability of Quantum Dots, Quantum Dot Films, and Quantum Dot Light-Emitting Diodes for Display Applications. *Advanced Materials* **2019**, 31 (34), 1804294.

90. Huang, H.; Chen, B.; Wang, Z.; Hung, T. F.; Susha, A. S.; Zhong, H.; Rogach, A. L., Water resistant $CsPbX_3$ nanocrystals coated with polyhedral oligomeric silsesquioxane and their use as solid state luminophores in all-perovskite white light-emitting devices. *Chemical Science* **2016**, 7, 5699-5703.

91. Li, X.; Xue, Z. J.; Luo, D.; Huang, C. H.; Liu, L. Z.; Qiao, X. Z.; Liu, C.; Song, Q.; Yan, C.; Li, Y. C.; Wang, T., A stable lead halide perovskite nanocrystals protected by PMMA. *Sci China Mater* **2018**, 61 (3), 363-370.

92. Zhang, M.; Wang, M.; Yang, Z.; Li, J.; Qiu, H., Preparation of all-inorganic perovskite quantum dots-polymer composite for white LEDs application. *Journal of Alloys and Compounds* **2018**, 748, 537-545.

93. Raja, S. N.; Bekenstein, Y.; Koc, M. A.; Fischer, S.; Zhang, D.; Lin, L.; Ritchie, R. O.; Yang, P.; Alivisatos, A. P., Encapsulation of Perovskite Nanocrystals into Macroscale Polymer Matrices: Enhanced Stability and Polarization. *ACS Applied Materials & Interfaces* **2016**, 8 (51), 35523-35533.

REFERENCES

94. Wei, Y.; Deng, X.; Xie, Z.; Cai, X.; Liang, S.; Ma, P. a.; Hou, Z.; Cheng, Z.; Lin, J., Enhancing the Stability of Perovskite Quantum Dots by Encapsulation in Crosslinked Polystyrene Beads via a Swelling–Shrinking Strategy toward Superior Water Resistance. *Advanced Functional Materials* **2017**, 27 (39), 1703535.
95. Pan, A.; Jurow, M. J.; Qiu, F.; Yang, J.; Ren, B.; Urban, J. J.; He, L.; Liu, Y., Nanorod Suprastructures from a Ternary Graphene Oxide-Polymer-$CsPbX_3$ Perovskite Nanocrystal Composite That Display High Environmental Stability. *Nano Letters* **2017**, 17 (11), 6759-6765.
96. Erman, B.; Flory, P. J., Critical Phenomena and Transitions in Swollen Polymer Networks and in Linear Macromolecules. *Macromolecules* **1986**, 19 (9), 2342-2353.
97. Cao, S.; Gody, G.; Zhao, W.; Perrier, S.; Peng, X.; Ducati, C.; Zhao, D.; Cheetham, A. K., Hierarchical bicontinuous porosity in metal–organic frameworks templated from functional block co-oligomer micelles. *Chemical Science* **2013**, 4 (9), 3573-3577.
98. Eddaoudi, M.; Kim, J.; Rosi, N.; Vodak, D.; Wachter, J.; Keeffe, M.; Yaghi, O. M., Systematic Design of Pore Size and Functionality in Isoreticular MOFs and Their Application in Methane Storage. *Science* **2002**, 295 (5554), 469.
99. Shen, K.; Zhang, L.; Chen, X.; Liu, L.; Zhang, D.; Han, Y.; Chen, J.; Long, J.; Luque, R.; Li, Y.; Chen, B., Ordered macro-microporous metal-organic framework single crystals. *Science* **2018**, 359 (6372), 206.
100. Lee, K. J.; Lee, J. H.; Jeoung, S.; Moon, H. R., Transformation of Metal–Organic Frameworks/Coordination Polymers into Functional Nanostructured Materials: Experimental Approaches Based on Mechanistic Insights. *Accounts of Chemical Research* **2017**, 50 (11), 2684-2692.
101. Yang, G.; Fan, Q.; Chen, B.; Zhou, Q.; Zhong, H., Reprecipitation synthesis of luminescent $CH_3NH_3PbBr_3/NaNO_3$ nanocomposites with enhanced stability. *Journal of Materials Chemistry C* **2016**, 4 (48), 11387-11391.
102. Dirin, D. N.; Benin, B. M.; Yakunin, S.; Krumeich, F.; Raino, G.; Frison, R.; Kovalenko, M. V., Microcarrier-Assisted Inorganic Shelling of Lead Halide Perovskite Nanocrystals. *ACS Nano* **2019**, 13 (10), 11642-11652.

REFERENCES

103. Li, Z.-J.; Hofman, E.; Li, J.; Davis, A. H.; Tung, C.-H.; Wu, L.-Z.; Zheng, W., Photoelectrochemically Active and Environmentally Stable $CsPbBr_3/TiO_2$ Core/Shell Nanocrystals. *Advanced Functional Materials* **2018**, 28 (1), 1704288.

104. Anaya, M.; Rubino, A.; Rojas, T. C.; Galisteo-López, J. F.; Calvo, M. E.; Míguez, H., Strong Quantum Confinement and Fast Photoemission Activation in $CH_3NH_3PbI_3$Perovskite Nanocrystals Grown within Periodically Mesostructured Films. *Advanced Optical Materials* **2017**, 5 (8), 1601087.

105. Demchyshyn, S.; Roemer, J. M.; Groiß, H.; Heilbrunner, H.; Ulbricht, C.; Apaydin, D.; Böhm, A.; Rütt, U.; Bertram, F.; Hesser, G.; Scharber, M. C.; Sariciftci, N. S.; Nickel, B.; Bauer, S.; Głowacki, E. D.; Kaltenbrunner, M. Confining metal-halide perovskites in nanoporous thin films. *Science Advances* **2017**, 3 (8), e1700738.

106. Qiu, L.; Yang, H.; Dai, Z.; Sun, F.; Hao, J.; Guan, M.; Dang, P.; Yan, C.; Lin, J.; Li, G., Highly efficient and stable $CsPbBr_3$ perovskite quantum dots by encapsulation in dual-shell hollow silica spheres for WLEDs. *Inorganic Chemistry Frontiers* **2020**, 7 (10), 2060-2071.

107. Huang, Y.; Li, F.; Qiu, L.; Lin, F.; Lai, Z.; Wang, S.; Lin, L.; Zhu, Y.; Wang, Y.; Jiang, Y.; Chen, X., Enhancing the Stability of $CH_3NH_3PbBr_3$ Nanoparticles Using Double Hydrophobic Shells of SiO_2 and Poly(vinylidene fluoride). *ACS Applied Materials & Interfaces* **2019**, 11 (29), 26384-26391.

108. Chen, Y.; Yu, M.; Ye, S.; Song, J.; Qu, J., All-inorganic $CsPbBr_3$ perovskite quantum dots embedded in dual-mesoporous silica with moisture resistance for two-photon-pumped plasmonic nanoLasers. *Nanoscale* **2018**, 10 (14), 6704-6711.

109. Liu, Z.; Zhang, Y.; Fan, Y.; Chen, Z.; Tang, Z.; Zhao, J.; Lv, Y.; Lin, J.; Guo, X.; Zhang, J.; Liu, X., Toward Highly Luminescent and Stabilized Silica-Coated Perovskite Quantum Dots through Simply Mixing and Stirring under Room Temperature in Air. *ACS Applied Materials & Interfaces* **2018**, 10 (15), 13053-13061.

110. Xu, L.; Chen, J.; Song, J.; Li, J.; Xue, J.; Dong, Y.; Cai, B.; Shan, Q.; Han, B.; Zeng, H., Double-Protected All-Inorganic Perovskite Nanocrystals by Crystalline Matrix and Silica for Triple-Modal Anti-Counterfeiting Codes. *ACS Applied Materials & Interfaces* **2017**, 9, 31, 26556–26564.

REFERENCES

111. Hu, H.; Wu, L.; Tan, Y.; Zhong, Q.; Chen, M.; Qiu, Y.; Yang, D.; Sun, B.; Zhang, Q.; Yin, Y., Interfacial Synthesis of Highly Stable $CsPbX_3$/Oxide Janus Nanoparticles. *Journal of the American Chemical Society* **2018**, 140 (1), 406-412.

112. Landau, L. D., Akhiezer, A. I., & Lifshitz, E. M, Surface phenomena. *General Physics*, **1967**, 276–293.

113. Brinker, C. J., Hydrolysis and condensation of silicates: Effects on structure. *Journal of Non-Crystalline Solids* **1988**, 100 (1), 31-50.

114. Dirin, D. N.; Protesescu, L.; Trummer, D.; Kochetygov, I. V.; Yakunin, S.; Krumeich, F.; Stadie, N. P.; Kovalenko, M. V., Harnessing Defect-Tolerance at the Nanoscale: Highly Luminescent Lead Halide Perovskite Nanocrystals in Mesoporous Silica Matrixes. *Nano Letters* **2016**, 16 (9), 5866-5874.

115. Chen, P.; Liu, Y.; Zhang, Z.; Sun, Y.; Hou, J.; Zhao, G.; Zou, J.; Fang, Y.; Xu, J.; Dai, N., In situ growth of ultrasmall cesium lead bromine quantum dots in a mesoporous silica matrix and their application in flexible light-emitting diodes. *Nanoscale* **2019**, 11 (35), 16499-16507.

116. Zhang, Q.; Wang, B.; Zheng, W.; Kong, L.; Wan, Q.; Zhang, C.; Li, Z.; Cao, X.; Liu, M.; Li, L., Ceramic-like stable $CsPbBr_3$ nanocrystals encapsulated in silica derived from molecular sieve templates. *Nature Communications* **2020**, 11 (1), 31.

117. Zhao, H.; Zhou, Y.; Benetti, D.; Ma, D.; Rosei, F., Perovskite quantum dots integrated in large-area luminescent solar concentrators. *Nano Energy* **2017**, 37, 214-223.

118. Troughton, J.; Gasparini, N.; Baran, D., Cs 0.15 FA 0.85 PbI 3 perovskite solar cells for concentrator photovoltaic applications. *Journal of Materials Chemistry A* **2018**, 6 (44), 21913-21917.

119. Dr. Narayanasamy Sabari Arul, D. V. D. N., *Chapter 4*. Perovskite Materials in Biomedical Applications. In Revolution of Perovskite Synthesis, Properties and Applications, **2020**.

120. Gasparini, A., Two-photon excited perovskite nanocrystals for bio-imaging. *Scilight* **2019**, 42, 421104.

121. C&en Seeking to boost oil production, petroleum researchers turn to nanotech. https://cen.acs.org/energy/fossil-fuels/Seeking-boost-oil-production-petroleum/96/i40.

REFERENCES

122. Zhang, Q.; Wang, B.; Zheng, W.; Kong, L.; Wan, Q.; Zhang, C.; Li, Z.; Cao, X.; Liu, M.; Li, L., Ceramic-like stable $CsPbBr_3$ nanocrystals encapsulated in silica derived from molecular sieve templates. *Nature Communications* **2020**, 11 (1), 31.

123. Qiu, L.; Ono, L. K.; Qi, Y., Advances and challenges to the commercialization of organic–inorganic halide perovskite solar cell technology. *Materials Today Energy* **2018**, 7, 169-189.

124. Babayigit, A.; Duy Thanh, D.; Ethirajan, A.; Manca, J.; Muller, M.; Boyen, H.-G.; Conings, B., Assessing the toxicity of Pb- and Sn-based perovskite solar cells in model organism Danio rerio. *Scientific Reports* **2016**, 6 (1), 18721.

125. Slavney, A. H.; Smaha, R. W.; Smith, I. C.; Jaffe, A.; Umeyama, D.; Karunadasa, H. I., Chemical Approaches to Addressing the Instability and Toxicity of Lead–Halide Perovskite Absorbers. *Inorganic Chemistry* **2017**, 56 (1), 46-55.

126. Lee, B.; Stoumpos, C. C.; Zhou, N.; Hao, F.; Malliakas, C.; Yeh, C.-Y.; Marks, T. J.; Kanatzidis, M. G.; Chang, R. P. H., Air-Stable Molecular Semiconducting Iodosalts for Solar Cell Applications: Cs_2SnI_6 as a Hole Conductor. *Journal of the American Chemical Society* **2014**, 136 (43), 15379-15385.

127. Dalpian, G. M.; Liu, Q.; Stoumpos, C. C.; Douvalis, A. P.; Balasubramanian, M.; Kanatzidis, M. G.; Zunger, A., Changes in charge density vs changes in formal oxidation states: The case of Sn halide perovskites and their ordered vacancy analogues. *Physical Review Materials* **2017**, 1 (2), 025401.

128. Ma, L.; Hao, F.; Stoumpos, C. C.; Phelan, B. T.; Wasielewski, M. R.; Kanatzidis, M. G., Carrier Diffusion Lengths of over 500 nm in Lead-Free Perovskite $CH_3NH_3SnI_3$ Films. *Journal of the American Chemical Society* **2016**, 138 (44), 14750-14755.

129. Wang, A.; Guo, Y.; Muhammad, F.; Deng, Z., Controlled Synthesis of Lead-Free Cesium Tin Halide Perovskite Cubic Nanocages with High Stability. *Chemistry of Materials* **2017**, 29 (15), 6493-6501.

130. Nishimura, K.; Kamarudin, M. A.; Hirotani, D.; Hamada, K.; Shen, Q.; Iikubo, S.; Minemoto, T.; Yoshino, K.; Hayase, S., Lead-free tin-halide perovskite solar cells with 13% efficiency. *Nano Energy* **2020**, 74, 104858.

REFERENCES

131. Wang, A.; Yan, X.; Zhang, M.; Sun, S.; Yang, M.; Shen, W.; Pan, X.; Wang, P.; Deng, Z., Controlled Synthesis of Lead-Free and Stable Perovskite Derivative Cs_2SnI_6 Nanocrystals via a Facile Hot-Injection Process. *Chemistry of Materials* **2016**, 28 (22), 8132-8140.

132. Qiu, X.; Cao, B.; Yuan, S.; Chen, X.; Qiu, Z.; Jiang, Y.; Ye, Q.; Wang, H.; Zeng, H.; Liu, J.; Kanatzidis, M. G., From unstable $CsSnI_3$ to air-stable Cs_2SnI_6: A lead-free perovskite solar cell light absorber with bandgap of 1.48eV and high absorption coefficient. *Solar Energy Materials and Solar Cells* **2017**, 159, 227-234.

133. Hu, W.; Cong, H.; Huang, W.; Huang, Y.; Chen, L.; Pan, A.; Xue, C., Germanium/perovskite heterostructure for high-performance and broadband photodetector from visible to infrared telecommunication band. *Light: Science & Applications* **2019**, 8 (1), 106.

134. Krishnamoorthy, T.; Ding, H.; Yan, C.; Leong, W. L.; Baikie, T.; Zhang, Z.; Sherburne, M.; Li, S.; Asta, M.; Mathews, N.; Mhaisalkar, S. G., Lead-free germanium iodide perovskite materials for photovoltaic applications. *Journal of Materials Chemistry A* **2015**, 3 (47), 23829-23832.

135. Chang, X.; Marongiu, D.; Sarritzu, V.; Sestu, N.; Wang, Q.; Lai, S.; Mattoni, A.; Filippetti, A.; Congiu, F.; Lehmann, A. G.; Quochi, F.; Saba, M.; Mura, A.; Bongiovanni, G., Layered Germanium Hybrid Perovskite Bromides: Insights from Experiments and First-Principles Calculations. *Advanced Functional Materials* **2019**, 29 (31), 1903528.

136. Jain, S. M.; Edvinsson, T.; Durrant, J. R., Green fabrication of stable lead-free bismuth based perovskite solar cells using a non-toxic solvent. *Communications Chemistry* **2019**, 2 (1), 91.

137. Ahmad, K., Bismuth Halide Perovskites for Photovoltaic Applications. *IntechOpen*, **2020**.

138. Pham, M.; Harris, J.; Shaffer, J.; Daniel, A.; Chowdhury, S.; Ali, A.; Banerjee, S.; Ahmed, S., Bismuth perovskite as a viable alternative to Pb perovskite solar cells: device simulations to delineate critical efficiency dynamics. *Journal of Materials Science: Materials in Electronics* **2019**, 30 (10), 9438-9443.

139. Soykan, C.; Gocmez, H., The physical properties of bismuth replacement in lead halogen perovskite solar cells: $CH_3NH_3Pb_{1-x}Bi_xI_3$ compounds by ab-initio calculations. *Results in Physics* **2019**, 13, 102278.

REFERENCES

140. Jin, Z.; Zhang, Z.; Xiu, J.; Song, H.; Gatti, T.; He, Z., A critical review on bismuth and antimony halide based perovskites and their derivatives for photovoltaic applications: recent advances and challenges. *Journal of Materials Chemistry A* **2020**, 8 (32), 16166-16188.

141. Yang, Y.; Liu, C.; Cai, M.; Liao, Y.; Ding, Y.; Ma, S.; Liu, X.; Guli, M.; Dai, S.; Nazeeruddin, M. K., Dimension-Controlled Growth of Antimony-Based Perovskite-like Halides for Lead-Free and Semitransparent Photovoltaics. *ACS Applied Materials & Interfaces* **2020**, 12 (14), 17062-17069.

142. Tuohey, H.; Della Gaspera, E.; van Embden, J., Perovskite-Inspired High Stability Organometal Antimony(V) Halide Thin Films by Post-Deposition Bromination. *ACS Materials Letters* **2020**, 2 (9), 1203-1210.

143. Zhou, H.; Cui, X.; Yuan, C.; Cui, J.; Shi, S.; He, G.; Wang, Y.; Wei, J.; Pu, X.; Li, W.; Zhang, D.; Wang, J.; Ren, X.; Ma, H.; Shao, X.; Wei, X.; Zhao, J.; Zhang, X.; Yin, J., Band-Gap Tuning of Organic–Inorganic Hybrid Palladium Perovskite Materials for a Near-Infrared Optoelectronics Response. *ACS Omega* **2018**, 3 (10), 13960-13966.

144. Mancini, A.; Quadrelli, P.; Milanese, C.; Patrini, M.; Guizzetti, G.; Malavasi, L., $CH_3NH_3Sn_xPb_{1-x}Br_3$ Hybrid Perovskite Solid Solution: Synthesis, Structure, and Optical Properties. *Inorganic Chemistry* **2015**, 54 (18), 8893-8895.

145. Jellicoe, T. C.; Richter, J. M.; Glass, H. F. J.; Tabachnyk, M.; Brady, R.; Dutton, S. E.; Rao, A.; Friend, R. H.; Credgington, D.; Greenham, N. C.; Böhm, M. L., Synthesis and Optical Properties of Lead-Free Cesium Tin Halide Perovskite Nanocrystals. *Journal of the American Chemical Society* **2016**, 138 (9), 2941-2944.

146. Ferrara, C.; Patrini, M.; Pisanu, A.; Quadrelli, P.; Milanese, C.; Tealdi, C.; Malavasi, L., Wide band-gap tuning in Sn-based hybrid perovskites through cation replacement: the $FA_{1-x}MA_xSnBr_3$ mixed system. *Journal of Materials Chemistry A* **2017**, 5 (19), 9391-9395.

147. Pisanu, A.; Mahata, A.; Mosconi, E.; Patrini, M.; Quadrelli, P.; Milanese, C.; De Angelis, F.; Malavasi, L., Exploring the Limits of Three-Dimensional Perovskites: The Case of $FAPb_{1-x}Sn_xBr_3$. *ACS Energy Letters* **2018**, 3 (6), 1353-1359.

REFERENCES

148. Stoumpos, C. C.; Malliakas, C. D.; Kanatzidis, M. G., Semiconducting Tin and Lead Iodide Perovskites with Organic Cations: Phase Transitions, High Mobilities, and Near-Infrared Photoluminescent Properties. *Inorganic Chemistry* **2013**, 52 (15), 9019-9038.

149. Tao, S.; Schmidt, I.; Brocks, G.; Jiang, J.; Tranca, I.; Meerholz, K.; Olthof, S., Absolute energy level positions in tin- and lead-based halide perovskites. *Nature Communications* **2019**, 10 (1), 2560.

150. Dang, Y.; Zhou, Y.; Liu, X.; Ju, D.; Xia, S.; Xia, H.; Tao, X., Formation of Hybrid Perovskite Tin Iodide Single Crystals by Top-Seeded Solution Growth. *Angewandte Chemie* **2016**, 55 (10), 3447-3450.

151. Cai, Y.; Xie, W.; Ding, H.; Chen, Y.; Thirumal, K.; Wong, L. H.; Mathews, N.; Mhaisalkar, S. G.; Sherburne, M.; Asta, M., Computational Study of Halide Perovskite-Derived A_2BX_6 Inorganic Compounds: Chemical Trends in Electronic Structure and Structural Stability. *Chemistry of Materials* **2017**, 29 (18), 7740-7749.

152. Ju, M.-G.; Chen, M.; Zhou, Y.; Garces, H. F.; Dai, J.; Ma, L.; Padture, N. P.; Zeng, X. C., Earth-Abundant Nontoxic Titanium(IV)-based Vacancy-Ordered Double Perovskite Halides with Tunable 1.0 to 1.8 eV Bandgaps for Photovoltaic Applications. *ACS Energy Letters* **2018**, 3 (2), 297-304.

153. Xiao, Z.; Zhou, Y.; Hosono, H.; Kamiya, T., Intrinsic defects in a photovoltaic perovskite variant Cs_2SnI_6. *Physical Chemistry Chemical Physics* **2015**, 17 (29), 18900-18903.

154. Qiu, X.; Jiang, Y.; Zhang, H.; Qiu, Z.; Yuan, S.; Wang, P.; Cao, B., Lead‐free mesoscopic Cs_2SnI_6 perovskite solar cells using different nanostructured ZnO nanorods as electron transport layers. *Physica Status Solidi - Rapid Research Letters* **2016**, 10 (8), 587-591.

155. Dolzhnikov, D. S.; Wang, C.; Xu, Y.; Kanatzidis, M. G.; Weiss, E. A., Ligand-Free, Quantum-Confined Cs_2SnI_6 Perovskite Nanocrystals. *Chemistry of Materials* **2017**, 29 (18), 7901-7907.

156. Ghosh, S.; Paul, S.; De, S. K., Control Synthesis of Air-Stable Morphology Tunable Pb-Free Cs_2SnI_6 Perovskite Nanoparticles and Their Photodetection Properties. *Particle & Particle Systems Characterization* **2018**, 35 (9), 1800199.

REFERENCES

157. Xu, Y.; Li, S.; Zhang, Z.; Hu, Y.; Yuan, L.; Chen, W.; Chen, Z.; Patterson, R.; Huang, S., Ligand-mediated synthesis of colloidal Cs_2SnI_6 three-dimensional nanocrystals and two-dimensional nanoplatelets. *Nanotechnology* **2019**, 30 (29), 295601.

158. Cao, D. H.; Stoumpos, C. C.; Yokoyama, T.; Logsdon, J. L.; Song, T.-B.; Farha, O. K.; Wasielewski, M. R.; Hupp, J. T.; Kanatzidis, M. G., Thin Films and Solar Cells Based on Semiconducting Two-Dimensional Ruddlesden–Popper $(CH_3(CH_2)_3NH_3)_2(CH_3NH_3)_{n-1}Sn_nI_{3n+1}$ Perovskites. *ACS Energy Letters* **2017**, 2 (5), 982-990.

159. Li, M.; Zuo, W.; Yang, Y.; Aldamasy, M. H.; Wang, Q.; Cruz, S. H. T.; Feng, S.-L.; Saliba, M.; Wang, Z.-K.; Abate, A., Tin Halide Perovskite Films Made of Highly Oriented 2D Crystals Enable More Efficient and Stable Lead-free Perovskite Solar Cells. *ACS Energy Letters* **2020**, 5 (6), 1923-1929.

160. Liao, Y.; Shang, Y.; Wei, Q.; Wang, H.; Ning, Z., Two-dimensional tin perovskite nanoplate for pure red light-emitting diodes. *Journal of Physics D: Applied Physics* **2020**, 53 (41), 414005.

161. Zhang, X.; Wang, C.; Zhang, Y.; Zhang, X.; Wang, S.; Lu, M.; Cui, H.; Kershaw, S. V.; Yu, W. W.; Rogach, A. L., Bright Orange Electroluminescence from Lead-Free Two-Dimensional Perovskites. *ACS Energy Letters* **2019**, 4 (1), 242-248.

162. Park, S.; An, M. N.; Almeida, G.; Palazon, F.; Spirito, D.; Krahne, R.; Dang, Z.; De Trizio, L.; Manna, L., $CsPbX_3/SiO_x$ (X = Cl, Br, I) monoliths prepared via a novel sol–gel route starting from Cs_4PbX_6 nanocrystals. *Nanoscale* **2019**, 11 (40), 18739-18745.

163. Choi, W. K.; Chim, W. K.; Heng, C. L.; Teo, L. W.; Ho, V.; Ng, V.; Antoniadis, D. A.; Fitzgerald, E. A., Observation of memory effect in germanium nanocrystals embedded in an amorphous silicon oxide matrix of a metal–insulator– semiconductor structure. *Applied Physics Letters* **2002**, 80 (11), 2014-2016.

164. Zeng, F.; Yang, M.; Qin, J.; Teng, F.; Wang, Y.; Chen, G.; Wang, D.; Peng, H., Ultrastable Luminescent Organic–Inorganic Perovskite Quantum Dots via Surface Engineering: Coordination of Methylammonium Bromide and Covalent Silica Encapsulation. *ACS Applied Materials & Interfaces* **2018**, 10 (49), 42837-42843.

REFERENCES

165. Sathe, T. R.; Agrawal, A.; Nie, S., Mesoporous Silica Beads Embedded with Semiconductor Quantum Dots and Iron Oxide Nanocrystals: Dual-Function Microcarriers for Optical Encoding and Magnetic Separation. *Analytical Chemistry* **2006**, 78 (16), 5627-5632.

166. Kim, J.; Lee, J. E.; Lee, J.; Yu, J. H.; Kim, B. C.; An, K.; Hwang, Y.; Shin, C.-H.; Park, J.-G.; Kim, J.; Hyeon, T., Magnetic Fluorescent Delivery Vehicle Using Uniform Mesoporous Silica Spheres Embedded with Monodisperse Magnetic and Semiconductor Nanocrystals. *Journal of the American Chemical Society* **2006**, 128 (3), 688-689.

167. Ishida, H.; Kumar, G., Molecular Characterization of Composite Interfaces. *Springer* **1985**.

168. Huang, S.; Li, Z.; Kong, L.; Zhu, N.; Shan, A.; Li, L., Enhancing the Stability of $CH_3NH_3PbBr_3$ Quantum Dots by Embedding in Silica Spheres Derived from Tetramethyl Orthosilicate in "Waterless" Toluene. *Journal of the American Chemical Society* **2016**, 138 (18), 5749-5752.

169. Zhong, Q.; Cao, M.; Hu, H.; Yang, D.; Chen, M.; Li, P.; Wu, L.; Zhang, Q., One-Pot Synthesis of Highly Stable $CsPbBr_3@SiO_2$ Core–Shell Nanoparticles. *ACS Nano* **2018**, 12 (8), 8579-8587.

170. Ciriminna, R.; Sciortino, M.; Alonzo, G.; Schrijver, A. d.; Pagliaro, M., From Molecules to Systems: Sol-Gel Microencapsulation in Silica-Based Materials. *Chemical Reviews* **2011**, 111 (2), 765-789.

171. Wu, L.; Hu, H.; Xu, Y.; Jiang, S.; Chen, M.; Zhong, Q.; Yang, D.; Liu, Q.; Zhao, Y.; Sun, B.; Zhang, Q.; Yin, Y., From Nonluminescent Cs_4PbX_6 (X = Cl, Br, I) Nanocrystals to Highly Luminescent $CsPbX_3$ Nanocrystals: Water-Triggered Transformation through a CsX-Stripping Mechanism. *Nano Letters* **2017**, 17 (9), 5799-5804.

172. Akkerman, Q. A.; Park, S.; Radicchi, E.; Nunzi, F.; Mosconi, E.; De Angelis, F.; Brescia, R.; Rastogi, P.; Prato, M.; Manna, L., Nearly Monodisperse Insulator Cs_4PbX_6 (X = Cl, Br, I) Nanocrystals, Their Mixed Halide Compositions, and Their Transformation into $CsPbX_3$ Nanocrystals. *Nano Lett.* **2017**, 17, 3, 1924-1930.

173. Akkerman, Q. A.; Meggiolaro, D.; Dang, Z.; De Angelis, F.; Manna, L., Fluorescent Alloy $CsPb_xMn_{1-x}I_3$ Perovskite Nanocrystals with High Structural and Optical Stability. *ACS Energy Letters* **2017**, 2 (9), 2183-2186.

REFERENCES

174. Palazon, F.; Di Stasio, F.; Akkerman, Q. A.; Krahne, R.; Prato, M.; Manna, L., Polymer-Free Films of Inorganic Halide Perovskite Nanocrystals as UV-to-White Color-Conversion Layers in LEDs. *Chemistry of Materials* **2016**, 28 (9), 2902-2906.

175. Akkerman, Q. A.; Park, S.; Radicchi, E.; Nunzi, F.; Mosconi, E.; De Angelis, F.; Brescia, R.; Rastogi, P.; Prato, M.; Manna, L., Nearly monodisperse insulator Cs_4PbX_6 (X= Cl, Br, I) nanocrystals, their mixed halide compositions, and their transformation into $CsPbX_3$ nanocrystals. *Nano Lett.* **2017**, 17 (3), 1924-1930.

176. An, M. N.; Park, S.; Brescia, R.; Lutfullin, M.; Sinatra, L.; Bakr, O. M.; De Trizio, L.; Manna, L., Low-Temperature Molten Salts Synthesis: $CsPbBr_3$ Nanocrystals with High Photoluminescence Emission Buried in Mesoporous SiO_2. *ACS Energy Letters* **2021**, 900-907.

177. Soulantica, K.; Maisonnat, A.; Fromen, M.-C.; Casanove, M.-J.; Chaudret, B., Spontaneous Formation of Ordered 3D Superlattices of Nanocrystals from Polydisperse Colloidal Solutions. *Angewandte Chemie* **2003**, 115 (17), 1989-1993.

178. Hyeon, T.; Lee, S. S.; Park, J.; Chung, Y.; Na, H. B., Synthesis of Highly Crystalline and Monodisperse Maghemite Nanocrystallites without a Size-Selection Process. *Journal of the American Chemical Society* **2001**, 123 (51), 12798-12801.

179. Murray, C. B.; Norris, D. J.; Bawendi, M. G., Synthesis and characterization of nearly monodisperse CdE (E = sulfur, selenium, tellurium) semiconductor nanocrystallites. *Journal of the American Chemical Society* **1993**, 115 (19), 8706-8715.

180. Srivastava, V.; Liu, W.; Janke, E. M.; Kamysbayev, V.; Filatov, A. S.; Sun, C. J.; Lee, B.; Rajh, T.; Schaller, R. D.; Talapin, D. V., Understanding and Curing Structural Defects in Colloidal GaAs Nanocrystals. *Nano Lett.* **2017**, 17 (3), 2094-2101.

181. Liu, X.; Fechler, N.; Antonietti, M., Salt melt synthesis of ceramics, semiconductors and carbon nanostructures. *Chemical Society Reviews* **2013**, 42 (21), 8237-8265.

182. Liu, X.; Antonietti, M.; Giordano, C., Manipulation of Phase and Microstructure at Nanoscale for SiC in Molten Salt Synthesis. *Chemistry of Materials* **2013**, 25 (10), 2021-2027.

REFERENCES

183. Kanady, J. S.; Leidinger, P.; Haas, A.; Titlbach, S.; Schunk, S.; Schierle-Arndt, K.; Crumlin, E. J.; Wu, C. H.; Alivisatos, A. P., Synthesis of Pt_3Y and Other Early–Late Intermetallic Nanoparticles by Way of a Molten Reducing Agent. *Journal of the American Chemical Society* **2017**, 139 (16), 5672-5675.

184. Lin, H.; Zhang, X.; Cai, L.; Lao, J.; Qi, R.; Luo, C.; Chen, S.; Peng, H.; Huang, R.; Duan, C., High-stability fluorescent perovskites embedded in PbBrOH triggered by imidazole derivatives in water. *Journal of Materials Chemistry C* **2020**, 8 (16), 5594-5599.

185. Protesescu, L.; Yakunin, S.; Bodnarchuk, M. I.; Krieg, F.; Caputo, R.; Hendon, C. H.; Yang, R. X.; Walsh, A.; Kovalenko, M. V., Nanocrystals of Cesium Lead Halide Perovskites ($CsPbX_3$, X = Cl, Br, and I): Novel Optoelectronic Materials Showing Bright Emission with Wide Color Gamut. *Nano Letters* **2015**, 15 (6), 3692-3696.

186. Pan, A.; Wu, Y.; Yan, K.; Yu, Y.; Jurow, M. J.; Ren, B.; Zhang, C.; Ding, S.; He, L.; Liu, Y., Stable Luminous Nanocomposites of Confined Mn^{2+}-Doped Lead Halide Perovskite Nanocrystals in Mesoporous Silica Nanospheres as Orange Fluorophores. *Inorganic Chemistry* **2019**, 58 (6), 3950-3958.

187. Lantelme, F.; Groult, H., Molten Salts Chemistry: From Lab to Applications. *Elsevier Science* **2013**.

188. Malgras, V.; Ataee-Esfahani, H.; Wang, H.; Jiang, B.; Li, C.; Wu, K. C.-W.; Kim, J. H.; Yamauchi, Y., Nanoarchitectures for Mesoporous Metals. *Advanced Materials* **2016**, 28 (6), 993-1010.

189. Sun, Y.-H.; Sun, L.-B.; Li, T.-T.; Liu, X.-Q., Modulating the Host Nature by Coating Alumina: A Strategy to Promote Potassium Nitrate Decomposition and Superbasicity Generation on Mesoporous Silica SBA-15. *The Journal of Physical Chemistry C* **2010**, 114 (44), 18988-18995.

190. Liu, X.-Y.; Sun, L.-B.; Lu, F.; Li, T.-T.; Liu, X.-Q., Constructing mesoporous solid superbases by a dualcoating strategy. *Journal of Materials Chemistry A* **2013**, 1 (5), 1623-1631.

191. Liu, N.; Wu, Z.; Li, M.; Li, S.; Luo, Z.; Li, Y.; Pan, L.; Liu, Y., Low-Temperature Preparation of a Mesoporous Silica Superbase by Employing the Multifunctionality of a La_2O_3 Interlayer. *ChemCatChem* **2017**, 9 (9), 1641-1647.

REFERENCES

192. Liu, X.-Y.; Sun, L.-B.; Lu, F.; Liu, X.-D.; Liu, X.-Q., Low-temperature generation of strong basicity via an unprecedented guest–host redox interaction. *Chemical Communications* **2013**, 49 (73), 8087-8089.

193. Pascual, M. J.; Pascual, L.; Valle, F. J.; Durán, A.; Berjoan, R., Corrosion of Borosilicate Sealing Glasses for Molten Carbonate Fuel Cells. *Journal of the American Chemical Society* **2003**, 86 (11), 1918-1926.

194. Hu, G.; Li, W.; Xu, J.; He, G.; Ge, Y.; Pan, Y.; Wang, J.; Yao, B., Substantially reduced crystallization temperature of SBA-15 mesoporous silica in $NaNO_3$ molten salt. *Materials Letters* **2016**, 170, 179-182.

195. Huang, Y.-M.; Singh, K. J.; Liu, A.-C.; Lin, C.-C.; Chen, Z.; Wang, K.; Lin, Y.; Liu, Z.; Wu, T.; Kuo, H.-C., Advances in Quantum-Dot-Based Displays. *Nanomaterials* **2020**, 10 (7).

196. Hu, Z.; Gao, H.; Ramisetti, S. B.; Zhao, J.; Nourafkan, E.; Glover, P. W. J.; Wen, D., Carbon quantum dots with tracer-like breakthrough ability for reservoir characterization. *Science of The Total Environment* **2019**, 669, 579-589.

197. Franco, C. A.; Candela, C. H.; Gallego, J.; Marin, J.; Patiño, L. E.; Ospina, N.; Patiño, E.; Molano, M.; Villamil, F.; Bernal, K. M.; Lopera, S. H.; Franco, C. A.; Cortés, F. B., Easy and Rapid Synthesis of Carbon Quantum Dots from Mortiño (Vaccinium Meridionale Swartz) Extract for Use as Green Tracers in the Oil and Gas Industry: Lab-to-Field Trial Development in Colombia. *Industrial & Engineering Chemistry Research* **2020**, 59 (25), 11359-11369.

198. Imran, M.; Caligiuri, V.; Wang, M.; Goldoni, L.; Prato, M.; Krahne, R.; De Trizio, L.; Manna, L., Benzoyl Halides as Alternative Precursors for the Colloidal Synthesis of Lead-Based Halide Perovskite Nanocrystals. *J. Am. Chem. Soc.* **2018**, 140 (7), 2656-2664.

199. Saparov, B.; Sun, J.-P.; Meng, W.; Xiao, Z.; Duan, H.-S.; Gunawan, O.; Shin, D.; Hill, I. G.; Yan, Y.; Mitzi, D. B., Thin-Film Deposition and Characterization of a Sn-Deficient Perovskite Derivative Cs_2SnI_6. *Chemistry of Materials* **2016**, 28 (7), 2315-2322.

200. Stoumpos, C. C.; Cao, D. H.; Clark, D. J.; Young, J.; Rondinelli, J. M.; Jang, J. I.; Hupp, J. T.; Kanatzidis, M. G., Ruddlesden–Popper Hybrid Lead Iodide Perovskite 2D Homologous Semiconductors. *Chemistry of Materials* **2016**, 28 (8), 2852-2867.

REFERENCES

201. Weidman Mc Fau - Seitz, M.; Seitz M Fau - Stranks, S. D.; Stranks, S. D.; Tisdale, W. A., Highly Tunable Colloidal Perovskite Nanoplatelets through Variable Cation, Metal, and Halide Composition. *ACS Nano* **2016**, 10, 8, 7830–7839.

202. Cheng, Z.; Lin, J., Layered organic–inorganic hybrid perovskites: structure, optical properties, film preparation, patterning and templating engineering. *CrystEngComm* **2010**, 12 (10), 2646-2662.

203. Era, M.; Maeda, K.; Tsutsui, T., Self-organization approach to organic/inorganic quantum-well based on metal halide-based layer perovskite. *Thin Solid Films* **1998**, 331 (1), 285-290.

204. Yuan, Z.; Zhou, C.; Tian, Y.; Shu, Y.; Messier, J.; Wang, J. C.; van de Burgt, L. J.; Kountouriotis, K.; Xin, Y.; Holt, E.; Schanze, K.; Clark, R.; Siegrist, T.; Ma, B., One-dimensional organic lead halide perovskites with efficient bluish white-light emission. *Nature Commun*ications **2017**, 8 (1), 14051.

205. Yuan, Z.; Zhou, C.; Messier, J.; Tian, Y.; Shu, Y.; Wang, J.; Xin, Y.; Ma, B., A Microscale Perovskite as Single Component Broadband Phosphor for Downconversion White-Light-Emitting Devices. *Advanced Optical Materials* **2016**, 4 (12), 2009-2015.

206. Lin, H.; Zhou, C.; Tian, Y.; Siegrist, T.; Ma, B., Low-Dimensional Organometal Halide Perovskites. *ACS Energy Letters* **2018**, 3 (1), 54-62.

207. Zhou, C.; Lin, H.; Shi, H.; Tian, Y.; Pak, C.; Shatruk, M.; Zhou, Y.; Djurovich, P.; Du, M.-H.; Ma, B., A Zero-Dimensional Organic Seesaw-Shaped Tin Bromide with Highly Efficient Strongly Stokes-Shifted Deep-Red Emission. *Angewandte Chemie* **2018**, 57 (4), 1021-1024.

208. Yamasaki, Y.; Ohno, N., Self-Trapped Excitons in Orthorhombic $SnBr_2$. *International Journal of Modern Physics B* **2001**, 15, 4009.

209. Lin, H.; Zhou, C.; Tian, Y.; Besara, T.; Neu, J.; Siegrist, T.; Zhou, Y.; Bullock, J.; Schanze, K. S.; Ming, W.; Du, M.-H.; Ma, B., Bulk assembly of organic metal halide nanotubes. *Chemical Science* **2017**, 8 (12), 8400-8404.

210. Zhou, C.; Lin, H.; Tian, Y.; Yuan, Z.; Clark, R.; Chen, B.; Van de Burgt, L. J.; Wang, J. C.; Zhou, Y.; Hanson, K.; Meisner, Q. J.; Neu, J.; Besara, T.; Siegrist, T.; Lambers, E.; Djurovich, P.; Ma, B., Luminescent zero-dimensional organic metal halide hybrids with near-unity quantum efficiency. *Chemical Science* **2018**, 9 (3), 586-593.

REFERENCES

211. Mourdikoudis, S.; Liz-Marzán, L. M., Oleylamine in Nanoparticle Synthesis. *Chemistry of Materials* **2013**, 25 (9), 1465-1476.

212. Pisal, A. A.; Rao, A. V., Comparative studies on the physical properties of TEOS, TMOS and Na_2SiO_3 based silica aerogels by ambient pressure drying method. *Journal of Porous Materials* **2016**, 23 (6), 1547-1556.

213. Hao Zhang, J. J., Wenyong Liu, Dmitri V. Talapin, Colloidal Nanocrystals with Inorganic Halide, Pseudohalide, and Halometallate Ligands. *ACS Nano* **2014**, 8 (7), 7359–7369.

214. Zhang, H.; Dasbiswas, K.; Ludwig, N. B.; Han, G.; Lee, B.; Vaikuntanathan, S.; Talapin, D. V., Stable colloids in molten inorganic salts. *Nature* **2017**, 542 (7641), 328-331.

215. Kamysbayev, V.; Srivastava, V.; Ludwig, N. B.; Borkiewicz, O. J.; Zhang, H.; Ilavsky, J.; Lee, B.; Chapman, K. W.; Vaikuntanathan, S.; Talapin, D. V., Nanocrystals in Molten Salts and Ionic Liquids: Experimental Observation of Ionic Correlations Extending beyond the Debye Length. *ACS Nano* **2019**, 13 (5), 5760-5770.

216. Srivastava, V.; Kamysbayev, V.; Hong, L.; Dunietz, E.; Klie, R. F.; Talapin, D. V., Colloidal Chemistry in Molten Salts: Synthesis of Luminescent $In_{1-x}Ga_xP$ and $In_{1-x}Ga_xAs$ Quantum Dots. *Journal of the American Chemical Society* **2018**, 140 (38), 12144-12151.

217. Yan, W.; Mao, L.; Zhao, P.; Mertens, A.; Dottermusch, S.; Hu, H.; Jin, Z.; Richards, B. S., Determination of complex optical constants and photovoltaic device design of all-inorganic $CsPbBr_3$ perovskite thin films. *Optics Express* **2020**, 28 (10), 15706-15717.